Restoring Fine Motor Skills through Neural Interface Technology

by

Zachary Thomas Irwin

**A dissertation submitted in partial fulfillment
of the requirements for the degree of
Doctor of Philosophy
(Biomedical Engineering)
in the University of Michigan
2016**

Doctoral Committee:

Assistant Professor Cynthia A. Chestek, Chair
Assistant Professor William C. Stacey
Assistant Professor Deanna H. Gates
Professor Douglas C. Noll

DEDICATION

For Ashleigh

ACKNOWLEDGEMENTS

This has been a wild ride – an exciting, terrifying, depressing, amazing ride. At the end of it, about the only thing I can say with certainty is that I would not have made it through without the help, advice, and encouragement of what seems like thousands of people. Nothing I say here will be enough to convey the extent of the gratitude I have for all of you, but I'll try anyway.

First and foremost, I would like to thank my family. Most of all my wife, Ashleigh, who has put up with all the craziness for far too long and been far too nice about it; I only hope I can pay back the support and encouragement in kind. My parents and brothers – how on Earth could I possibly fit all of it into one page? You deserve most of the credit for who I am today.

My advisor, Cindy Chestek, took me on as her first graduate student sight unseen, and I still maintain that she took a bigger risk than I did. I hope that it paid off for her as much as it has for me, I am forever grateful. I'd like to thank the rest of my committee as well, Bill Stacey, Deanna Gates, and Doug Noll, for past help and advice as well as for future enlightening grilling. Bill Stacey in particular put up with my stumbling around learning about big data processing for my first year of grad school, and wasn't too upset with me when I totally bailed on him.

And finally, the Chestek lab, thank you guys so much for your help, advice, commiseration, friendship, and coffee. Everyone in the lab, currently and in the past, has had a huge impact on my work and my life, and I have no idea what I will do without all of you. Maybe we'll meet up in another dingy backroom bar and grab some waffles.

TABLE OF CONTENTS

LIST OF FIGURES

LIST OF TABLES

ABSTRACT

Loss of motor function in the upper-limb, whether through paralysis or through loss of the limb itself, is a profound disability which affects a large population worldwide. While lifelike, fully-articulated prosthetic hands exist and are commercially available, there is currently no satisfactory method of controlling all of the available degrees of freedom. In order to generate better control signals for this technology and help restore normal movement, it is necessary to interface directly with the nervous system. This thesis is intended to address several of the limitations of current neural interfaces and enable the long-term extraction of control signals for fine movements of the hand and fingers.

The first study addresses the problems of low signal amplitudes and short implant lifetimes in peripheral nerve interfaces. In two rhesus macaques, we demonstrated the successful implantation of regenerative peripheral nerve interfaces (RPNI), which allowed us to record high amplitude, functionally-selective signals from peripheral nerves up to 20 months post-implantation. These signals could be accurately decoded into intended movement, and used to enable monkeys to control a virtual hand prosthesis.

The second study presents a novel experimental paradigm for intracortical neural interfaces, which enables detailed investigation of fine motor information contained in primary motor cortex. We used this paradigm to demonstrate accurate decoding of continuous fingertip position and enable a monkey to control a virtual hand in closed-loop. This is the first demonstration of volitional control of fine motor skill enabled by a cortical neural interface.

The final study presents the design and testing of a wireless implantable neural recording system. By extracting signal power in a single, configurable frequency band onboard the device, this system achieves low power consumption while maintaining decode performance, and is applicable to cortical, peripheral, and myoelectric signals. This suggests a novel path to both clinical and commercial viability for fully-implanted neural interfaces.

Taken together, these results represent a significant step towards clinical reality for neural interfaces, and towards restoration of full and dexterous movement for people with severe disabilities.

CHAPTER I

Introduction

Loss of motor function in the upper-limb, whether through paralysis or through loss of the limb itself, is a profound disability which affects a large population worldwide. In the United States, around 500,000 people are currently living with at least partial upper-limb loss (Ziegler-Graham et al., 2008) and another 140,000 are living with tetraplegia resulting from spinal cord injury (National Spinal Cord Injury Statistical Center, 2012). Currently available clinical solutions to this problem are woefully inadequate. People living with paralysis have virtually no solutions available to them, and people with partial or total limb loss are limited to simple prostheses which restore only basic functionality. According to surveys of these populations, there is a pressing need to restore hand-level function (Anderson et al., 2008; Snoek et al., 2004), which would enable more normal interactions with the environment for the majority of people as well as restore basic self-sufficiency in the most extreme cases.

The technology to address this need currently exists: lifelike, fully-articulated prosthetic hands have been developed, and several are commercially available. The fundamental issue with current prosthetic technology, however, is the lack of sufficient control signals. It is not possible, with available body-powered or myoelectric controllers, to naturally and effectively use all of the functions of advanced prostheses. Users are limited to unintuitive control of a single movement or simple grasp at a time (Lovely, 2004; Roche et al., 2014), which does not approach the functionality of the normal limb.

In order to generate better control signals for this technology, and help restore normal movement, it is necessary to interface directly with the nervous system. In both amputation and paralysis, the volitional neural drive is still intact, whether in the peripheral or central nervous systems. Thus, useful information about intended movement can be extracted (Carmena et al., 2003; Dhillon and Horch, 2005; Georgopoulos et al., 1986; Warren et al., 2016), and provide patients with functional control of advanced prostheses (Collinger et al., 2013; Kuiken et al., 2009).

There is significant interest in neural interface technology among both amputees and spinal cord injury patients, even at higher levels of surgical invasiveness (Blabe et al., 2015; Engdahl et al., 2015), but there are still many challenges to solve before it is practical for clinical implementation. This thesis focuses on addressing several of these challenges for both peripheral and central neural interfaces: improving the stability and longevity of peripheral interfaces, demonstrating the functional efficacy of extracting finger-level movements directly from cortex, and developing a low-power implantable neural recording system for both peripheral and central signals.

The following sections will discuss current and investigational approaches for restoring function after both amputation and spinal cord injury, and present opportunities for improvements which will form the basis of this work.

1.1 Prosthesis Control for Amputation

1.1.1 Myoelectric Interfaces

Myoelectric prostheses record electromyographic (EMG) activity from muscles remaining after amputation and interpret that activity to actuate joints, or degrees of freedom (DoFs), on the prosthesis (e.g. wrist pronation, finger flexion, etc.). An ideal myoelectric controller would proportionally map activity recorded from each muscle onto the respective physiological movement on the prosthesis. This is known as "direct" control (Roche et al., 2014), and would, in theory, allow for the intuitive, independent control of all available joints on the prosthesis simultaneously. In current clinical practice, however, this type of control is severely limited.

All commercially-available myoelectric prostheses use surface electrodes to record EMG through the skin. While simple to implement and maintain, these electrodes are heavily affected by signal cross-talk, in which activity from both the intended and nearby muscles appear on the same electrode, and signal attenuation of EMG from deeper muscles (Farina et al., 2014). This limits the number of truly independent signals which can be recorded. For this reason, clinical myoelectric prostheses typically use only one or two electrodes in order to control a single motor function on the prosthesis (e.g. power grasp, key pinch, etc.). This motor function can be actuated either discretely, in response to the EMG activity on a given channel crossing a pre-defined threshold, or proportionally, in which the level of EMG activity is mapped continuously

to the velocity of the movement (Fougner et al., 2012). In order to control multiple functions with only one or two control signals, most prostheses implement mode switching, in which the user can change which function is currently being controlled by performing a particular EMG activation pattern (Lovely, 2004). While this allows prostheses to be somewhat more functional, it is cumbersome for the user and only roughly approximates normal function of the hand.

In order to enable simpler and more natural control, many research groups have investigated pattern recognition techniques to replace direct control (Hudgins et al., 1993). In this paradigm, by using more electrodes placed on the limb, machine learning algorithms are trained to recognize natural patterns of EMG activity that correspond to particular movements. Movements can be selected by simply attempting that movement, instead of relying on independent activation of single electrodes, which is more intuitive for the user and obviates the need for mode switching. Currently, there is one commercially-available pattern recognition prosthesis controller (Coapt LLC, Chicago, IL), but it has been on the market for less than a year and it remains to be seen how successful or accepted it will be. The primary limitation of typical pattern recognition control is that it is necessarily discrete and sequential. That is, only one motion can be selected at a time and cannot be controlled proportionally. Several groups are actively researching methods of adding the ability to perform both proportional and simultaneous control (Scheme et al., 2014; Young et al., 2013), with promising results.

While much progress has been made in increasing the functionality and usability of myoelectric interfaces, there is an inherent limit to this progress. As the level of amputation or paralysis gets higher, more control signals are needed to control all of the lost function. At the same time, recording sites which could provide natural, intuitive control are necessarily eliminated. In order to address this fundamental issue with myoelectric control, it becomes necessary to interface directly with the nervous system.

1.1.2 Peripheral Nerve Interfaces

Following amputation, even decades after the injury, peripheral nerves in the limb still carry volitional motor commands intended for the lost anatomy (Dhillon et al., 2004; Jia et al., 2007). These signals can be recorded and potentially used to extract movement intent for intuitive prosthesis control in cases where myoelectric interfaces are not useful. Electrodes for interfacing with nerves can be classified into two broad categories: epineural, in which the

electrode contacts lie directly on the outside of the nerve, and intraneural, in which the electrode penetrates the nerve and the contacts lie in close proximity to the internal nerve fascicles.

The most common type of epineural electrode is the nerve cuff (Naples et al., 1988; Sahin and Durand, 1998), in which contacts are embedded in a flexible substrate and wrapped around the outside of the nerve. Cuff electrodes have been widely used for nerve stimulation, but recording nerve activity with these electrodes is limited. Signal amplitudes outside the nerve are very small (Popovic et al., 1993) and must compete with much larger EMG from neighboring muscle (Navarro et al., 2005; Sahin et al., 1997).

To achieve higher amplitude signals, intraneural electrodes can be used to record from fascicles within the nerve. The two most commonly studied intraneural electrode variants are the longitudinal intrafascicular electrode (LIFE; [Lawrence et al., 2004]) and the Utah slant electrode array (USEA; [Branner et al., 2001]). Multiple studies have been performed with the LIFE array in humans, demonstrating offline classification of grasp types (Micera et al., 2011; Rossini et al., 2010), object discrimination using sensory percepts evoked via stimulation (Horch et al., 2011), and real-time control of prosthesis grip force and elbow position (Dhillon and Horch, 2005). Compared to the LIFE, the USEA consists of many more electrodes which are distributed throughout the cross-section of the nerve, intended to enable better sampling of fascicles. The USEA has been implanted semi-chronically in several healthy and amputee human subjects, and has enabled simple proportional control of grip force (Gasson et al., 2005), continuous control of individual finger movement (Warren et al., 2016), and the restoration of sensory perception (Clark et al., 2014).

The amplitude of volitional motor signals recorded by USEAs has been larger than is possible with cuff electrodes, but is still quite small compared to EMG signals which can appear on the same electrodes (Clark et al., 2011). This is a large confounding factor for direct nerve recordings and may limit the effectiveness of such interfaces, although some progress has been made in mitigating this noise source both in hardware (Clark et al., 2011) and signal processing (Warren et al., 2016). Perhaps the biggest unknown with intraneural electrodes is the expected longevity of the interface. By introducing foreign materials into the nerve, these arrays produce inflammatory responses and the accumulation of granulation tissue under and around the array in longer-term (>10 month) implantations (Christensen et al., 2014). In USEA human implantations, there have been no noted sensory or motor deficits (Warwick et al., 2003), though

the longest implant has been only 3 months (Gasson et al., 2005). Due to the short-term nature of these studies, it is unknown if the signal recording ability would remain stable over longer periods.

A promising alternative to these direct electrode-nerve interfaces is targeted muscle reinnervation (TMR; [Kuiken et al., 2004]). After amputation, the nerves originally innervating the arm and hand are severed, and can be re-routed into the non-functional residual muscles proximal to the injury. Over the course of a few months, the muscles are reinnervated by the transplanted nerves, and subsequently contract normally in response to descending motor commands. The muscles thus act as biological amplifiers for nerve activity, converting low amplitude neural action potentials in high amplitude EMG. This creates new myoelectric recording sites for natural control of lost hand function. TMR has been successfully implemented in over 60 shoulder disarticulation and transhumeral amputees worldwide as of 2013 (Miller et al., 2013). In early studies, TMR enabled the simultaneous proportional control of elbow position and either hand aperture or wrist rotation (either function could be mode selected and locked in position), and the patient was able to perform functional tasks easier than with his previous touchpad-controlled prosthesis (Kuiken et al., 2004). The same patient was later able to use a 6 DoF prosthetic limb and control up to three joints simultaneously, though two simultaneous movements were easier and more commonly used (Miller et al., 2008). Recent work has applied pattern recognition techniques to TMR (Zhou et al., 2007), classifying up to seven arm and hand movements to enable functional control of an advanced prosthetic arm (Kuiken et al., 2009).

While TMR is a vast improvement over traditional myoelectric prosthesis control in very proximal amputees, the effectiveness of the technique is limited by using whole nerves to reinnervate whole muscles. This does not allow for spatial separation of each function of the nerve, as the fascicles controlling many different muscles are spatially disorganized, and not all functions of the nerve are guaranteed to be represented in the reinnervated muscle (Stubblefield et al., 2009). Using surface electrodes, this limits the number of independent control sites enabled by TMR to one site for each whole nerve, a maximum of three in the arm (Kuiken et al., 2004; O'Shaughnessy et al., 2008). One additional issue with using surface electrodes is the inherent instability of the interface. Any change in either the position of the electrode in relation to the muscle, as seen during normal muscle contractions (O'Shaughnessy et al., 2008), or the condition of the skin-electrode interface (Farina et al., 2004) when, for example, sweating during

prosthesis use, will act to shift the pattern of EMG activity recorded by the electrode. The use of intramuscular electrodes, which are implanted directly into muscle tissue, would alleviate this issue. However, as the recording volume of typical intramuscular electrodes is small, the spatial distribution of signals within the reinnervated muscle may require an excessive number of electrodes to be implanted in order to ensure full signal coverage.

These peripheral interface solutions, both direct and indirect, are huge improvements over current myoelectric control. However, further improvements must still be made in the stability and longevity of the interface, as well as increasing the number of available independent control signals.

1.2 Movement Restoration for Spinal Cord Injury

1.2.1 Functional Electrical Stimulation

Unlike amputation, spinal cord injury (SCI) leaves the musculature and peripheral nerves intact, though useless to the patient. This provides the opportunity to restore limb movement through functional electrical stimulation (FES) instead of bypassing the limb in favor of a prosthesis. In FES, the peripheral nerves innervating the non-functional muscles in the limb are electrically stimulated in order to produce controlled movement (Peckham and Knutson, 2005). One fully-implanted FES system, the FreeHand (Hobby et al., 2001), was commercially available for a short time, but has since been taken off the market.

While FES is an effective solution that does not require a prosthesis, which may be a more palatable option for SCI patients (Blabe et al., 2015), it still requires sufficient control signals. In typical FES systems, voluntary commands can be provided either by a physical switch (Peckham et al., 2001) or by myoelectric recording of a non-paralyzed muscle (Kilgore et al., 2008). This provides mostly equivalent functionality to clinical myoelectric prostheses, controlling a single grasp type at a time (Peckham and Knutson, 2005). However, if the number of available functions increases, to make the system more capable, more control signals will be needed. Even in incomplete SCI, there is a severe limit to the number of available recording sites, and none will be intuitive for controlling multiple movements by the user. To remedy this, and also provide input for advanced prostheses, cortical interfaces may be necessary.

1.2.2 Cortical Neural Interfaces

Extracting motor control signals directly from the brain has been extensively studied for decades (Carmena et al., 2003; Evarts, 1968; Georgopoulos et al., 1982; Kennedy et al., 2000). Currently, there are a number of cortical interface technologies which vary in the level of invasiveness and spatial specificity. At the lowest end of the invasiveness spectrum is electroencephalography (EEG), in which electrodes are placed on the scalp. EEG requires no surgery to implement, and has been investigated for assistive technology such as communication devices (Krusienski et al., 2006) for paralyzed individuals. More invasive is electrocorticography (ECoG), in which electrodes are placed directly on the surface of the brain, typically under the dura mater layer. ECoG has been successfully used to classify movements of the arm and hand (Chestek et al., 2013; Pistohl et al., 2012), control a computer cursor (Schalk et al., 2008), and even enable rudimentary control of a robotic hand (Hotson et al., 2016). However, these interfaces, while advantageous in implementation, are limited in effectiveness due to their distance from motor output neurons and susceptibility to noise.

In order to access the most spatially specific signals, and thus extract the greatest amount of information, intracortical electrodes penetrate the brain to record directly from individual or small, local groups of neurons. Research into the practical application of intracortical interfaces has focused mostly on the control of computer cursors (Carmena et al., 2005; Fan et al., 2014; Li et al., 2009; Suminski et al., 2010), but several studies in the past decade have enabled the use of both simple and advanced prosthetic arms (Hochberg et al., 2012; Velliste et al., 2008). Initial studies enabled able-bodied monkeys to move a virtual cursor in 2D and 3D space to hit specified targets, using only neural activity recorded from primary motor cortex (Serruya et al., 2002; Taylor et al., 2002). This work was soon translated to paralyzed human subjects (Hochberg et al., 2006) during the initial BrainGate clinical trial for the 96-channel "Utah" intracortical electrode array (Nordhausen et al., 1994).

The control performance reported in these initial studies was relatively poor, possibly due to the simple decoding algorithms used to infer the subjects' movement intent. A key improvement in control signal extraction was the introduction of the Kalman filter to neural data (Wu et al., 2006), which enabled much higher performance in subsequent monkey (Wu et al., 2004) and human (Kim et al., 2008; Simeral et al., 2011) studies. Further improvements in algorithm design, such as the ReFIT Kalman filter (Gilja et al., 2012), have enabled the human

use of cortical interfaces for self-paced typing with rates up to six words per minute (Gilja et al., 2015) and a sustained rate of ~20 characters per minute over 42 days without user recalibration (Jarosiewicz et al., 2015).

Beyond control of computer cursors, which has demonstrated the efficacy of control signal extraction directly from the brain as well as the application of those control signals for assistive technology, intracortical interfaces have also enabled the direct control of prosthetic and paralyzed limbs. Initially, monkeys and humans were able to control only the arm endpoint in 3D space, along with either discrete or proportional control of a 1 DoF gripper (Hochberg et al., 2012; Velliste et al., 2008). More recent studies have extended this to also enable control of 3D hand orientation (Collinger et al., 2013), and hand shape (Wodlinger et al., 2015). Additionally, monkeys have been able to control several temporarily-paralyzed forearm muscles through FES to restore grasping in a functional task (Ethier et al., 2012; Moritz et al., 2008).

These studies, both cursor and limb control, have mostly focused on decoding movement of the arm in space, with control of dexterous functions of the hand itself limited to coarse control of one or several grasp patterns (Klaes et al., 2015; Wodlinger et al., 2015). Offline decoding of finger-level function has been investigated by several groups in monkeys. Discrete movements of the wrist and individual fingers could be classified with high accuracy (Egan et al., 2012; Hamed et al., 2007), and the continuous motion of up to 27 joints in the arm and hand could be reconstructed following whole-arm reaching (Aggarwal et al., 2013; Menz et al., 2015; Vargas-Irwin et al., 2010). Reconstruction of isolated movements of individual fingers has also been demonstrated (Aggarwal et al., 2009), though these movements were limited to a couple of millimeters and not representative of the full range of finger motion. As of yet, no studies have enabled online control of dexterous hand function.

1.3 Implantable Neural Recording Systems

Both peripheral and cortical neural interfaces have shown significant potential for generating prosthetic control signals; however, current systems require a percutaneous connection from the interface to recording equipment outside the body. This introduces a serious risk of infection, as well as limiting user mobility and increasing the noise present in the recorded signal. In order to translate these interfaces into the clinic, it is necessary to develop

recording systems which can be implanted in the body and wirelessly transmit information through the skin.

Many groups have developed and tested wireless and implantable systems for both neural and myoelectric interfaces (Farnsworth et al., 2009; Gosselin et al., 2009; Najafi and Wise, 1986; Sodagar et al., 2009; Weir et al., 2009). Myoelectric recording systems, in particular, have had the most clinical success thus far. Multiple fully-implanted FES systems have been tested in human subjects (Memberg et al., 2014), with one achieving FDA approval as a commercial system (Peckham et al., 2001). The IMES, a separate system intended to record intramuscular EMG for prosthetic control, is currently in clinical trials and has successfully been used to provide prosthesis control for the subject (Pasquina et al., 2015).

Currently, no implantable device for peripheral or cortical neural interfaces has been tested in human subjects. One potential reason for this discrepancy between myoelectric and neural interfaces is the higher bandwidth necessary for recording neural signals. In order to resolve neural action potentials, typical recording systems sample the signal at rates of >20kHz (Yin et al., 2013), whereas myoelectric signals can be sampled much slower (<3kHz; [Morel et al., 2016]). This high sampling rate requires a large amount of power to process and wirelessly transmit, which is made worse when using a large number of channels as is typical with neural interfaces. High power consumption in turn causes several issues in designing implantable devices, including high device temperatures and a short battery life (Borton et al., 2013; Gosselin et al., 2009; Harrison et al., 2009; Miranda et al., 2010).

Aside from new hardware architectures (Chae et al., 2009; Zou et al., 2013) and smaller fabrication process sizes (Gao et al., 2012), which complicate both the design and production of the device, significant power reduction can be achieved through data compression. By extracting and transmitting only the signal features actually used by the decoding algorithm, instead of the full broadband waveform, decode performance is unchanged while reducing wireless data rates by ~90% (Olsson and Wise, 2005). This compression has been used in both myoelectric devices, by extracting and transmitting the low bandwidth signal envelope (Hart et al., 2011; Weir et al., 2009), and in cortical interfaces by detecting neural action potentials onboard the device and transmitting either individual detection times or detection rates over a specified time interval (Harrison et al., 2009; Rizk et al., 2009). While successful, this technique has two primary issues. First, particularly for cortical devices, there is still a large processing overhead on the front-end

in order to resolve relevant signal features, requiring high-bandwidth amplifiers and high sampling rates (Chestek et al., 2009; Patterson et al., 2004), which limit the potential power reduction. Second, by focusing the design of the device around the extraction of specific signal features, the device is necessarily restricted to a particular interface. This is limiting particularly for cortical devices, as the potential market size is much smaller than for myoelectric or peripheral devices, and may preclude commercial viability.

1.4 Summary of Thesis

This thesis is intended to address several of the limitations of neural interfaces described previously, and thus enable the long-term extraction of control signals for fine movements of the hand and fingers.

First, in Chapter 2, we will address peripheral nerve interfaces, which are currently hampered by low signal amplitude, interface instability, and low functional resolution within the nerve. In two rhesus macaques, we demonstrate the successful implantation of a regenerative peripheral nerve interface (RPNI). The RPNI, which was developed and tested previously in a rat model (Kung et al., 2014; Ursu et al., 2016), consists of a small partial muscle graft which is reinnervated by a transected nerve, similar to targeted muscle reinnervation. By using small free grafts instead of whole muscles, as in TMR, the nerve can be subdivided into individual fascicles which reinnervate separate grafts, enabling the recording of high-amplitude, functionally-selective EMG via stable intramuscular electrodes. In this study, RPNI signals were successfully recorded for up to 20 months post-implantation, and could be decoded to accurately classify finger movements and enable closed-loop control of a virtual hand prosthesis. This demonstrates that the RPNI technique is safe and effective in long-term extraction of fine motor information from peripheral nerves.

In Chapter 3, we will present a novel experimental paradigm for intracortical interfaces which allows for the detailed investigation of fine motor information contained in primary motor cortex. Previous studies of intracortical decoding of finger movements have either been confounded by simultaneous upper-arm movement or have elicited only limited movement of the fingers. To address this, we use our novel behavioral task to demonstrate accurate offline decoding of isolated finger movements over the full range of motion in three rhesus macaques. Further, we apply this decode in real-time to enable one macaque to control a virtual hand

prosthesis, which represents the first demonstration of online, closed-loop control of fine motor skills using a cortical interface.

Chapter 4 will present the design and testing of a novel implantable neural recording system which is both low power and applicable to cortical, peripheral, and myoelectric interfaces. This power reduction and multi-modality is achieved by the onboard extraction of the signal power in a single, configurable frequency band, a signal feature which is both low bandwidth and common to all three interfaces. This study demonstrates that, despite a massive reduction in power consumption, decode performance does not significantly drop when using this system architecture, indicating the potential viability of this approach for future clinical devices.

Chapter 5 will discuss the results of each study and their implications for the future of prosthetic control as enabled by neural interface technology.

CHAPTER II

Chronic Recording of Hand Prosthesis Control Signals via a Regenerative Peripheral Nerve Interface in a Rhesus Macaque

A version of this chapter has been submitted for publication and is currently under peer review.

2.1 Abstract

Loss of even part of the upper limb is a devastating injury. In order to fully restore natural function when lacking sufficient residual musculature, it is necessary to record directly from peripheral nerves. However, current approaches must make trade-offs between signal quality and longevity which limit their clinical potential. To address this issue, we have developed the regenerative peripheral nerve interface (RPNI), which consists of a small, autologous partial muscle graft reinnervated by a transected peripheral nerve branch. After reinnervation, the graft acts as a bioamplifier for descending motor commands in the nerve, enabling long-term recording of high signal-to-noise ratio (SNR), functionally-specific electromyographic (EMG) signals. We implanted nine RPNIs on separate branches of the median and radial nerves in two rhesus macaques. No adverse events were noted in either monkey, and we recorded normal EMG with high SNR from the RPNIs for up to 20 months post-implantation. Using RPNI signals recorded during a behavioral task, we were able to classify each monkey's finger movements as flexion, extension, or rest with >96% accuracy. RPNI signals also enabled functional prosthetic control, allowing the monkeys to perform the same behavioral task equally well with either physical finger movements or RPNI-based movement classifications. The RPNI signal strength, stability, and longevity demonstrated here represents a promising method for controlling advanced prosthetic limbs and fully restoring natural movement.

2.2 Introduction

Loss of even part of the upper limb is a devastating injury, and current available prostheses cannot fully restore natural function. An estimated 20-40% of upper-limb amputees reject using a prosthesis (Biddiss and Chau, 2007; Raichle et al., 2008) mostly citing the lack of

functionality (Biddiss and Chau, 2007; Wright et al., 1995). Fully-articulated myoelectric prostheses, which use voluntary activation of residual muscles as a control signal, promise the restoration of multiple naturally-controlled degrees of freedom. However, the rejection rate for this state-of-the-art technology is not significantly better than that of simple body-powered hooks (Biddiss and Chau, 2007; McFarland et al., 2010).

The primary underlying issue with this technology is the scarcity of independent signals with which to control all of the available functions of the prosthesis. Direct prosthetic control, in which each recorded muscle is mapped to its corresponding physiological function on the prosthesis (Roche et al., 2014), would reduce the user's cognitive burden while operating the prosthesis and allow for intuitive, simultaneous control of multiple degrees of freedom. However, this requires a separate, independent control signal for each degree of freedom, which is not possible for standard surface electromyography (EMG) on an amputee due to a combination of inadequate remaining musculature, signal cross-talk contamination, and attenuation of deep muscle signals at the skin surface. This leads to either a reduced set of functions available to the user or non-physiological control strategies which require long and tedious training periods, both of which may contribute to rejection of the prosthesis.

An ideal solution to this problem is to record motor commands directly from peripheral nerves, which are still extant in the residual limb and carry information about the amputated musculature. However, this is difficult to accomplish in practice. Signals recorded by epineural electrodes are typically low amplitude and corrupted by much larger EMG activity from the surrounding muscles (Navarro et al., 2005; Sahin et al., 1997). More selective and higher amplitude signals can be recorded by penetrating intraneural electrodes (Clark et al., 2014), but damage to the nerve may result in shortened implant lifetime.

Targeted muscle reinnervation (TMR) solves many of the issues with both myoelectric and direct nerve interfaces, and has been successfully demonstrated in several amputees (Dumanian et al., 2009; Kuiken et al., 2009). A hybrid approach, the TMR procedure reroutes transected nerves from the arm into sections of denervated muscles in the chest or residual limb. After the muscles are reinnervated by the rerouted nerves, they produce large amplitude EMG activity in response to voluntary motor commands. These biologically amplified signals are recorded by high-density surface electrodes, and serve to increase the number of available physiologically-relevant control sites. Through TMR, patients have been able to use advanced

multi-functional robotic limbs, controlling elbow and wrist movement along with up to four hand grasps with no mode selection required (Kuiken et al., 2009).

The primary limitation of TMR, however, is that because whole nerves are attached to large sections of muscle, separate functional signals are not well isolated (Kuiken et al., 2004) and nerve fibers controlling any particular function are not guaranteed to reinnervate the new muscle (Stubblefield et al., 2009). This limits the number of independent control signals enabled by TMR. To overcome this, recent efforts have focused on pattern recognition algorithms to classify intended movement from a large number of electrodes covering the entire reinnervated area (Kuiken et al., 2009; Zhou et al., 2007). Though the user can select and initiate a large number of movements with this control scheme, they are largely limited to sequential movements in which one degree of freedom is activated at a time, increasing both the controller complexity and the required user training time. Additionally, the need to cover a large area may prohibit the use of implanted intramuscular electrodes, which would produce a much more stationary signal. This non-stationary signal in turn requires either frequent re-training of the controller or careful maintenance of the electrode interface, such as regularly taking off the prosthesis to dry accumulated sweat before continuing use (Kuiken et al., 2004).

To address these issues, we have developed the regenerative peripheral nerve interface (RPNI), which consists of a small, autologous partial muscle graft which has been reinnervated by a transected peripheral nerve branch. Following initial implantation, the muscle graft temporarily degenerates due to lack of innervation and vascularization. During this time, stem cells in the graft periphery are sustained via diffusion from the surrounding tissue and vascular bed (Faulkner et al., 1976). Over the course of several months, the graft is revascularized, regenerates (creating new, healthy muscle fibers), and is reinnervated by the transplanted nerve through axonal sprouting and elongation within the graft (Carlson and Faulkner, 1983; Cedars and Miller, 1984). The mature, reinnervated RPNI then produces high-amplitude EMG activity in response to voluntary motor commands (Ursu et al., 2016). The muscle graft thus acts as both a stable housing for the nerve and a biological amplifier for descending action potentials in the nerve.

Like TMR, the RPNI creates new physiologic EMG recording sites for natural control of multiple degrees of freedom. However, using small muscle grafts instead of large intact muscles enables several advantages. First, RPNIs can be placed directly at the distal end of the nerve

without re-routing the nerve into the large muscles of the chest or residual limb. This allows for the use of RPNIs with any level of amputation, and requires a less invasive surgical procedure. Second, RPNIs can be made more functionally selective by intraneural dissection of the residual nerve into fascicles and implanting separate RPNIs on each of these fascicles. By pairing each RPNI with an intramuscular EMG electrode, we can potentially record stable, independent signals from each fascicle in the nerve and implement more natural and effective prosthetic control schemes.

The long-term viability of RPNIs has been previously reported in a rat model (Kung et al., 2014), demonstrating that RPNIs are successfully reinnervated and maintain health and electrical responsiveness up to 7 months post-implantation. A further study found that implanted RPNIs produced high-amplitude, physiologically-appropriate EMG activity in response to volitional movement during walking in rats (Ursu et al., 2016). In order to test the safety and performance of this technique in the context of voluntary finger movements, we implanted RPNIs in the forearms of two healthy rhesus macaques. We recorded volitional EMG signals from the RPNIs during a finger movement task, and conducted a preliminary assessment of both the signal quality and the ability to extract functional information from the recorded signals in order to control a prosthetic hand.

2.3 Methods

All procedures were approved by the University of Michigan University Committee on the Use and Care of Animals. The author of this dissertation assisted with the described surgeries, designed and implemented all experimental procedures, and was primarily responsible for all data collection.

2.3.1 Regenerative peripheral nerve interface (RPNI) construction and implantation

The process of RPNI construction is demonstrated in figure 2.1 (a). First, the distal end of the target peripheral nerve is identified, isolated, and, if necessary, dissected into smaller branches or individual fascicles. For each resulting nerve, a small muscle graft, approximately 1x3 cm, is harvested from a large native donor muscle. The distal end of each nerve is then placed centrally in its corresponding muscle graft and secured in place with sutures from epineurium to epimysium. The muscle graft is then folded around the nerve to create a stable housing and sutured together. A newly-constructed RPNI is shown in figure 2.1 (b).

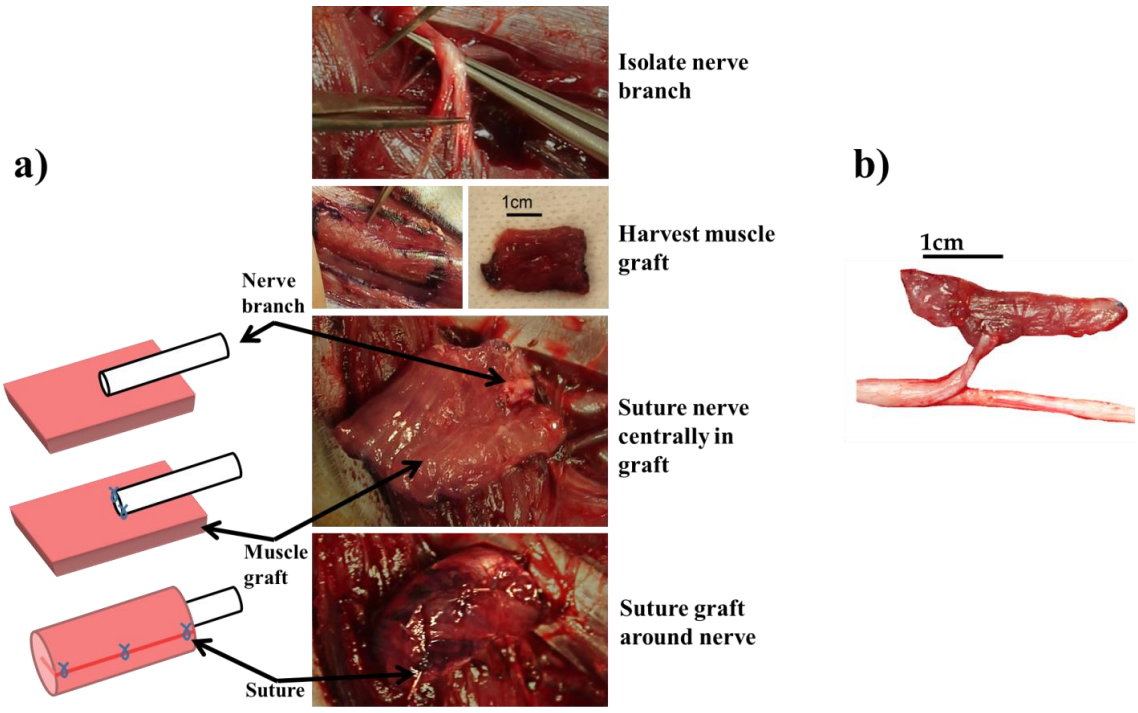

Figure 2.1. (a) RPNI implantation procedure illustrated from top to bottom. (b) A newly implanted RPNI, with a branch of the median nerve sutured into the muscle belly.

Implantation of multiple RPNIs is achieved by making small access incisions over the nerves of interest and the muscle for harvesting grafts. The above procedure is then simply repeated as necessary to create the desired number of RPNIs.

Following these procedures, we implanted a total of nine RPNIs on separate branches of the median and radial nerves in the forearms of two rhesus macaques, referred to hereafter as L and R. These branches terminated on the extrinsic finger flexors and extensors, providing a basis for prosthetic hand control. To preserve motor function, we transected only minor, redundant terminal motor nerve branches (see table 2.1 in the Results for details of each RPNI), leaving intact several branches to the same muscles.

2.3.2. Electrophysiology

During the first RPNI implantation surgery, we implanted several bipolar epimysial EMG electrodes (Plastics One, Roanoke, VA). The electrodes consisted of insulated stainless steel leads attached to a silicone backing. The electrodes were placed on the surface of the RPNI muscle grafts and secured in place by wrapping small intestinal submucosa (SIS) around the muscle-electrode construct and suturing it together. The leads were then tunneled subcutaneously

along the arm and back to a connector on the animal's headcap. Leads were looped at the RPNIs and at each joint for strain relief.

Shortly after surgery, the animal was able to break the leads at the margin of the headcap, leaving no intact electrodes for recording. In a revision surgery, it was noted that the stiffness of the silicone patch had caused significant scar formation and presumably impeded RPNI regeneration, so the epimysial electrodes were extracted and not used further on either animal.

Prior to chronic electrode implantation in both animals (during epimysial electrode extraction in the first animal and during the initial implantation surgery in the second animal), RPNIs were placed superficially in the subcutaneous plane in order to facilitate acute, percutaneous recording. During task behavior, we recorded EMG from the superficial RPNIs via fine-wire electrodes (Natus Medical, Pleasanton, CA). The RPNIs were located using surface landmarks and surgical photos. The wires were inserted into the RPNI muscle via hypodermic needle. As the RPNIs were located directly subcutaneously, the needle was inserted at a shallow angle and advanced just far enough to bury both contacts under the skin in order to avoid contact with the muscle within the deep compartments. Recording locations were verified in further revision surgeries. Percutaneous recordings of healthy, intact muscles were also obtained for comparison.

To subsequently facilitate chronic recording of RPNI activity, we implanted bipolar intramuscular electrodes (IM-MES; Ardiem Medical, Indiana, PA). The IM-MES electrodes consist of two insulated stainless steel leads coiled in a double helix formation and potted in silicone tubing (Memberg et al., 2014). Contacts are formed by exposing the leads and wrapping them around the tubing, and a polypropylene anchor at the distal end secures the electrode in the muscle. In the first animal, the two contacts on the electrode were 4 mm long with a diameter of 1.27 mm (the diameter of the silicone tubing), and were separated by 6 mm. After noting that, in some cases, this was too large to fit both contacts within the muscle belly of an RPNI, a reduced contact size of 1.5 mm and inter-contact spacing of 2.5 mm were used for the second animal. A single IM-MES electrode was placed in the muscle belly of each RPNI, as well as in a healthy control muscle, by making a small incision and manually feeding the electrode anchor-first into the muscle. Leads were tunneled subcutaneously to a transcutaneous port on the animal's back and attached to a connector protected by a primate jacket.

During task performance, EMG signals from the RPNIs were input into either a DAM50 differential EMG amplifier (WPI, Sarasota, FL), which filtered the signal between 10-1000 Hz with a gain of 1000x, or directly into a Cerebus neural signal processor (Blackrock Microsystems, Salt Lake City, UT), which filtered the signal between .3-7000 Hz (unity gain). For real-time signal analysis, the Cerebus was used to record from multiple electrodes simultaneously. The DAM50 was used for lower-noise recordings of a single electrode. In both cases, the processed signal was digitized and saved to disk by the Cerebus at 30ksps. The signal was further sent from the Cerebus to the behavioral rig via ethernet, where it could be processed in real-time.

During several revision surgeries after RPNI maturation in both animals, we tested the mature RPNIs for reinnervation and tissue health by evoking compound muscle action potentials (CMAPs) via stimulation of the implanted nerve. Using a Teca Synergy evoked potential system (Viasys Healthcare, Conshohocken, PA), we either stimulated the nerve just proximal to the point of entry to the RPNI or stimulated the muscle of the RPNI itself while simultaneously recording from bipolar electrodes in the belly of the RPNI muscle. Stimulation parameters varied between surgeries, consisting primarily of a pulse width of 200 μs and current amplitude between 1-20 mA when stimulating the nerve directly and a pulse width of 20 μs or 200 μs and current amplitude between 30-60 mA when stimulating the nerve through the RPNI muscle.

2.3.3 Behavioral task

We trained both monkeys to perform a finger movement task, illustrated in figure 2.2. A flex sensor (Spectra Symbol, West Valley City, UT) was attached to the monkey's index finger, which fed finger position data to a real-time computer running xPC Target (Mathworks, Natick, MA). A virtual model of a monkey hand was displayed in front of the monkey on a monitor, and mirrored the finger movements measured by the flex sensor. The monkeys both performed movements with all four fingers simultaneously, with the position of all four indicated by the index flex sensor. At the start of a trial, the xPC cued a spherical target to appear in the path of the virtual finger. The monkey was then required to move his fingers in order to hit the target on the screen. After holding the virtual finger in the target for a required hold time (usually set to 500-700 ms), the monkey was given a juice reward. The virtual hand could also be controlled by decoding the RPNI signals in real-time into predicted movement. The monkey would receive a

reward only if the predicted movement was correct, and could act to correct the decode within the trial time limit in a closed-loop manner.

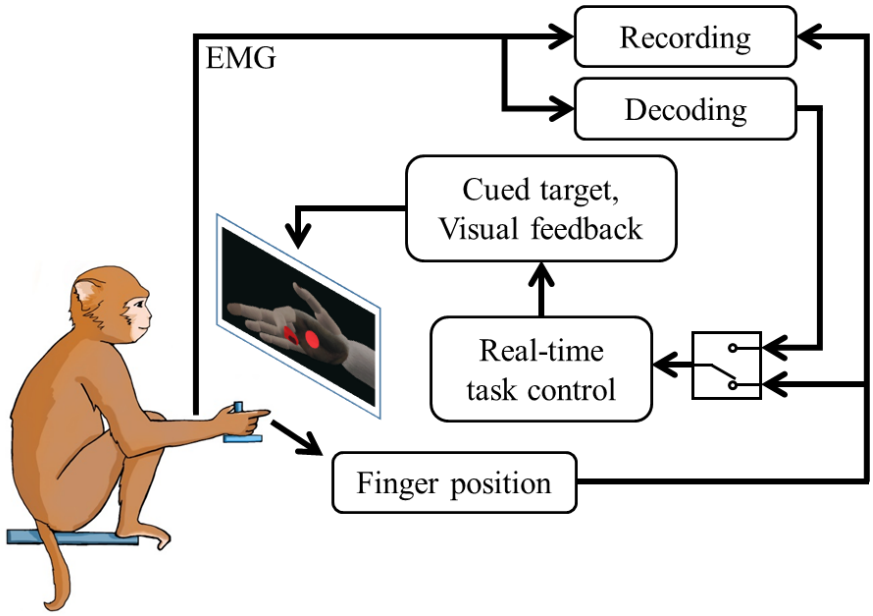

Figure 2.2. Monkey behavioral task. The monkey was required to hit virtual targets by moving his four fingers simultaneously. The virtual hand could be controlled either by the monkey's movements directly (as measured by flex sensors) or by EMG signals decoded into movement predictions in real-time, allowing either open-loop or closed-loop task performance.

2.3.4 Signal Analysis and Decoding

To isolate the EMG signal from motion and electrical artifacts, we filtered the data between 100-500 Hz using a second-order Butterworth filter. In offline analysis, the data were filtered forwards and backwards in order to eliminate phase shift.

For each recorded RPNI and intact muscle, we calculated both the maximum voluntary contraction (MVC) and the signal to noise ratio (SNR). MVC was calculated by isolating periods of maximum agonist behavior, corresponding to either full finger flexion or full finger extension movements, depending on the function of the RPNI nerve. Movement periods were isolated and labeled by thresholding the finger position and velocity to ensure both maximum EMG activation and consistent behavior. The mean of the peak-to-peak amplitude during all such movements was taken as the MVC. SNR was calculated by simply dividing the MVC by the noise floor for that channel, which was extracted by manually selecting quiescent periods in the signal and calculating the mean peak-to-peak amplitude.

In order to directly assess the functional efficacy of the RPNI signals, we classified current finger movement state using a Naïve Bayes classifier. Linear discriminant analysis was also performed, but classification accuracy was similar to that of the Naïve Bayes. As the decoding features, we extracted four temporal characteristics of the EMG waveform (Hudgins et al., 1993; Zhou et al., 2007) in successive 50 ms time bins: (1) mean absolute value, (2) number of zero crossings, (3) number of slope changes, and (4) waveform line length. This was performed both offline and online in closed-loop. During closed-loop decoding, three targets were presented to the monkey, requiring flexion, extension, and no movement (i.e. maintaining a neutral, relaxed hand position), respectively. After training the classifier on the first ~200 trials of normal task performance, the virtual hand was switched to mirror the classifier output instead of the monkey's actual finger position. To smooth the prediction, the final classifier output was updated only after four consecutive identical predictions. The virtual finger was automatically positioned in the target space associated with the current prediction, and the monkey was required to make the classifier output the correct state for the entire hold time (at least 10 consecutive time bins) in order to complete the task.

2.4 Results

A total of nine RPNIs were implanted on separate branches of the median and radial nerves in the forearms of two rhesus macaques, L and R. Pictures of several of the implanted RPNIs for each monkey are shown in figure 2.3, and the anatomical details of each RPNI are shown in table 2.1. RPNI names are based on the muscle originally innervated by the transected nerve branch, with a letter differentiating RPNIs with the same function.

Table 2.1. Details of implanted RPNIs.

Monkey	RPNI name	Nerve	Nerve branch function	Donor muscle
L	FDSa	Median	Flexion of digits 2-5 (PIP, MCP joints)	FCR
	FDSb	Median	Flexion of digits 2-5 (PIP, MCP joints)	FDS
	FDPa	Median	Flexion of digits 1-3* (DIP, PIP, MCP joints)	FCR
	FDPb	Median	Flexion of digits 1-3* (DIP, PIP, MCP joints)	FCR
	EDCa	Radial	Extension of digits 2-5 (DIP, PIP, MCP joints)	EDC
R	FDSc	Median	Flexion of digits 2-5 (PIP, MCP joints)	FCR
	FDPc	Median	Flexion of digits 1-3* (DIP, PIP, MCP joints)	FCR
	FDPd	Median	Flexion of digits 1-3* (DIP, PIP, MCP joints)	FCR
	EDCb	Radial	Extension of digits 2-5 (DIP, PIP, MCP joints)	EDC

* In the macaque, flexor pollicis longus does not exist and FDP has a tendon to thumb (Serlin and Schieber, 1993).
FDS – flexor digitorum superficialis, **FDP** – flexor digitorum profundus, **EDC** – extensor digitorum communis, **FCR** – flexor carpi radialis, **DIP** – distal interphalangeal joint, **PIP** – proximal interphalangeal joint, **MCP** – metacarpophalangeal joint.

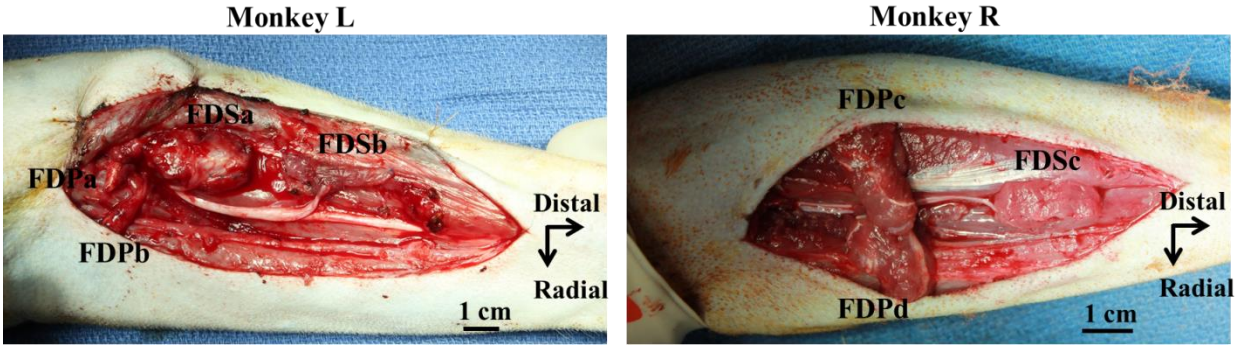

Figure 2.3. RPNIs implanted in the forearm of two monkeys (top – Monkey L, bottom – Monkey R), labeled as listed in table 2.1. All RPNIs in Monkey R and the FDSb RPNI in Monkey L are newly implanted, while the other RPNIs in Monkey L are mature and reinnervated.

A timeline of surgical procedures and electrophysiology recordings is shown in figure 2.4. In particular, note in Monkey L that EMG was recorded from the RPNIs up to 20 months post-implantation, and RPNIs were subsequently deemed healthy at the time of removal. Recordings were taken from Monkey R up to 14 months post-implantation, until experiments were completed. Monkey R's RPNIs and IM-MES electrodes have not been removed in order to facilitate long-term investigation of electrode implantation effects

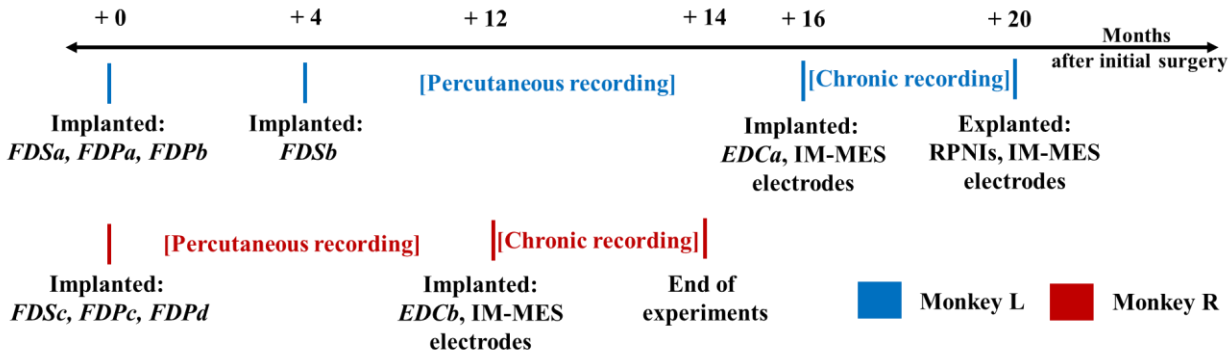

Figure 2.4. Timeline of RPNI surgeries, including both RPNI creation and chronic electrode implantation, and electrophysiology experiments. EMG was recorded from RPNIs in Monkey L up to 20 months post-implantation and from RPNIs in Monkey R up to 14 months post-implantation.

2.4.1 RPNIs caused no health issues

No major health concerns were noted by laboratory or veterinary staff during a 10-day post-op monitoring period or afterwards. In order to minimally disrupt normal function of the limb, we transected only small terminal nerve branches (leaving intact several other branches of the median and radial nerves innervating the FDS, FDP, and EDC muscles in the arm), and harvested only small (approximately 1x3 cm) grafts from large native FCR, FDS, and EDC muscles for each RPNI. Generally, muscle grafts can be harvested from any location, but here were taken from the implanted arm to limit the number of surgical sites. Following veterinary recommendation, buprenorphine was administered during the first 24 hours following each surgery, and carprofen and cefazolin administered for the first week to control possible pain and prevent wound infection. Both monkeys had minor swelling of the limb and hand immediately after one surgery (the second of three surgeries in Monkey L and the first of two in Monkey R), but this was attributed to the compression bandage applied at the end of surgery and not to the RPNI procedure itself. Both monkeys regained full use of the hand and limb within three days after each surgery, except in the case of Monkey R's swelling in which the animal recovered full use after one week, following fluid drainage by veterinary staff.

2.4.2 RPNIs successfully reinnervated and regenerated

All RPNIs appeared to regenerate and reinnervate successfully, producing healthy muscle tissue and an active neural connection. Visual inspection of RPNIs during revision surgeries indicated vascularized muscle grafts and integrated nerves. Because the EDCa RPNI in Monkey L was co-implanted with a chronic electrode upon initial implantation, it provided a clear

illustration of the regeneration process. The EDCa RPNI is shown in figure 2.5 (a), at the time of implantation and at the time of graft explantation four months later. As is typical, the mature muscle graft is somewhat smaller than the original graft, but is well vascularized and appears healthy. Histological staining (hematoxylin and eosin) of this RPNI, shown in figure 2.5 (b) indicates that the muscle fibers are somewhat smaller than in intact tissue, but the increased proportion of centrally-located nuclei and the more rounded shape of the RPNI fibers may also indicate that regeneration was still ongoing (Cedars et al., 1983). During the explantation surgery (at 4 months post-implantation, prior to tissue extraction), stimulation of the EDCa nerve produced compound muscle action potentials in the RPNI, indicating a healthy neuromuscular interface, as shown in figure 2.5 (d). Additionally, as a chronic intramuscular electrode was placed in the EDCa RPNI at implantation, we were able to track the degree of innervation over time, measured by the amplitude of the recorded signal during task performance. This is shown in figure 2.5 (c) as the signal amplitude during maximum voluntary contractions, compared to the equivalent signals recorded from an intact wrist muscle and a previously-matured RPNI. Note that only the EDCa RPNI shows an increasing trend in the signal amplitude, indicating reinnervation over a period of ~3 months, while the previously matured and reinnervated FDPb RPNI and the intact ECR (extensor carpi radialis) remain stable

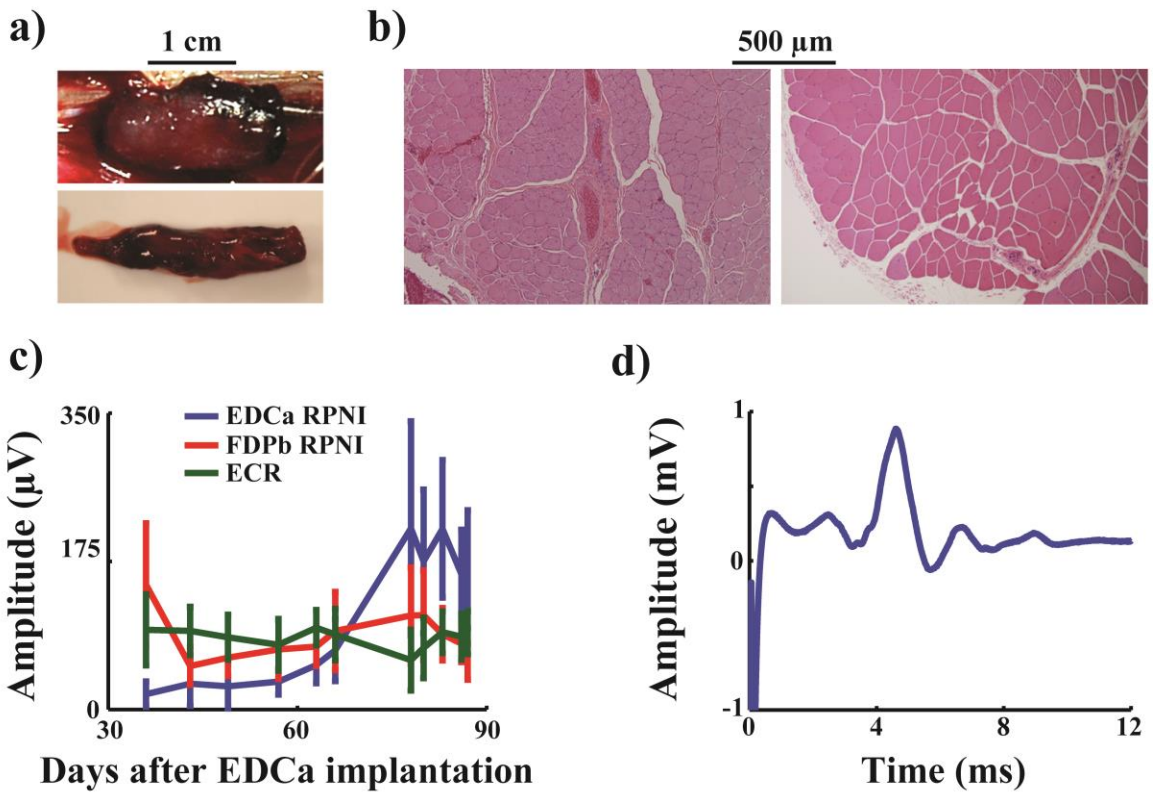

Figure 2.5. (a) EDCa RPNI at implantation (top) and after 3 months of maturation (bottom). (b) EDCa RPNI histology (H&E staining) after maturation (left) and comparison to intact FDS muscle (right). (c) Signal amplitude over time for the recently-implanted EDCa RPNI (blue), the matured FDPb RPNI (red), and the intact ECR muscle (green). (d) Mean CMAP produced by the EDCa RPNI in response to intra-operative stimulation.

No RPNIs failed to reinnervate, however it appeared that some RPNIs, particularly in Monkey R, reintegrated somewhat with the surrounding tissue. This made it more difficult to isolate the RPNI to place electrodes, and likely increased the amount of cross-talk picked up from nearby musculature. This may have been due to the non-use of SIS for these RPNIs, a smaller nerve transplant, or the swelling after Monkey R's initial implantation surgery. Even in these cases, however, the nerve was still intact and RPNI remained innervated as verified by intra-operative stimulation and visualization of healthy tissue.

2.4.3 RPNIs produce normal, volitional EMG

Signals recorded from RPNIs via both acute and chronically-implanted electrodes appeared similar to intact control muscles. EMG was correlated with the expected physical behavior of each nerve branch (either flexion or extension of the fingers), and single motor units could be discriminated from all RPNIs. Example IM-MES recordings are shown for several

RPNIs and intact muscles in figure 2.6, along with single unit action potentials extracted from each. In the bottom right trace of figure 2.6, the intact EDC signal was recorded from the IM-MES electrode originally placed in the EDCb RPNI. However, as the signal amplitude was very high immediately after implantation (which could not be produced by a denervated muscle), the electrode was assumed to have slipped out of the RPNI and was recording from the surrounding EDC muscle. It is included here as a healthy control muscle for comparison.

Though RPNI signal amplitudes varied, and were generally smaller in Monkey R, signal-to-noise ratios were high. This indicates that even with smaller amplitude signals, selective information can still be easily extracted from the RPNIs.

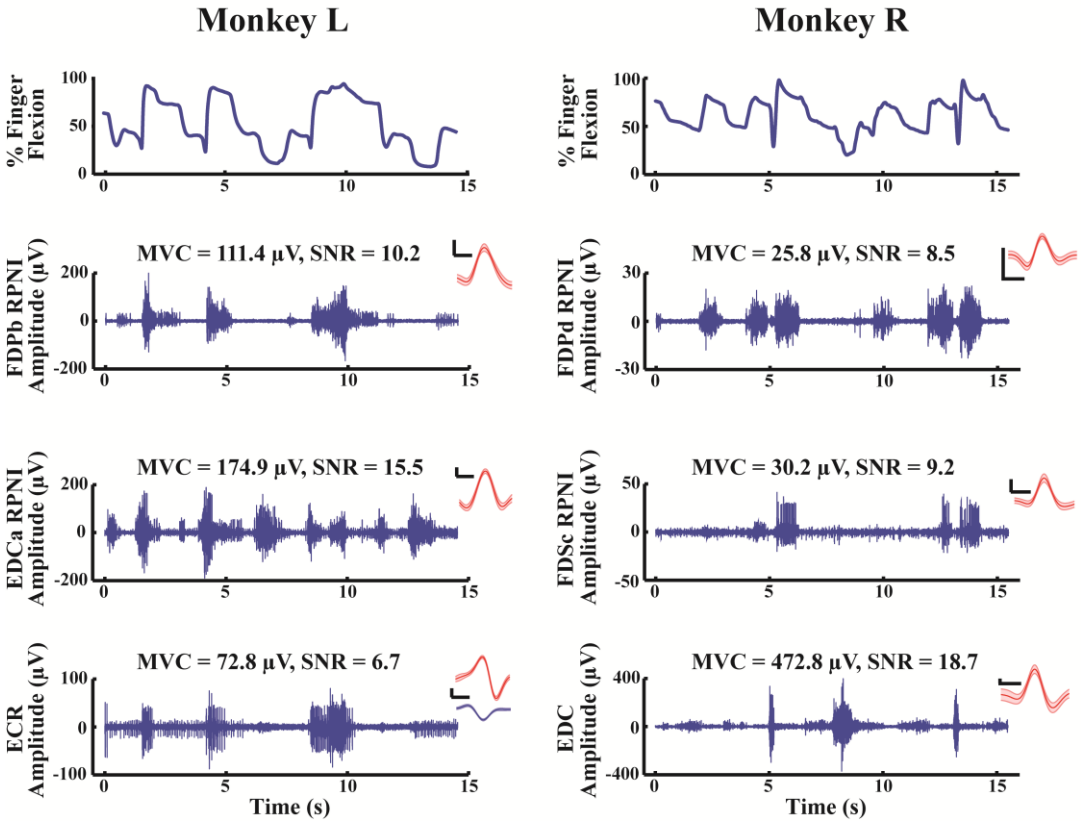

Figure 2.6. Example EMG recorded from chronic IM-MES electrodes in both monkeys (the bottom trace in each column is an intact muscle), with isolated single motor unit action potentials (to the right of each column - scale bars indicate 20 μV and 2 ms, respectively).

Cross-talk injected from nearby intact muscles was seen on several RPNIs, most likely due to incomplete implantation of the electrode in the RPNI (in several RPNIs, the proximal contact on the lead was located at least partially outside the muscle graft). In the left column of

figure 2.6, the EDCa RPNI signal is correlated with finger extension (as expected) and at least somewhat with finger flexion, probably corrupted by the nearby wrist extensor ECR (also shown in figure 2.6). However, the majority of the initial EDCa bursts during flexion are actually caused by the short extension movement immediately preceding flexion onset, rather than by the ECR cross-talk.

This cross-talk was not seen in percutaneous fine-wire recordings, indicating that, as expected, a smaller electrode would reveal more local activity. Accordingly, the amplitude of the signals obtained from acute, percutaneous electrodes varied widely across sessions. Two example recordings are shown in figure 2.7. This variability could potentially be exploited in the future to obtain more information from each RPNI. It also indicates that higher amplitude signals could potentially be recorded by optimally placing smaller electrodes in the RPNI muscle belly, as the fine-wire recording of the FDPd RPNI in Monkey R in figure 2.7 displayed a higher amplitude than the IM-MES recording of the same RPNI shown in figure 2.6. Importantly, it was possible to miss the RPNIs when inserting the fine-wires, which resulted in no discernable EMG and confirms that the recorded signals, when successfully attained, were in fact coming from local sources within the RPNI and not volume conduction from distant muscles.

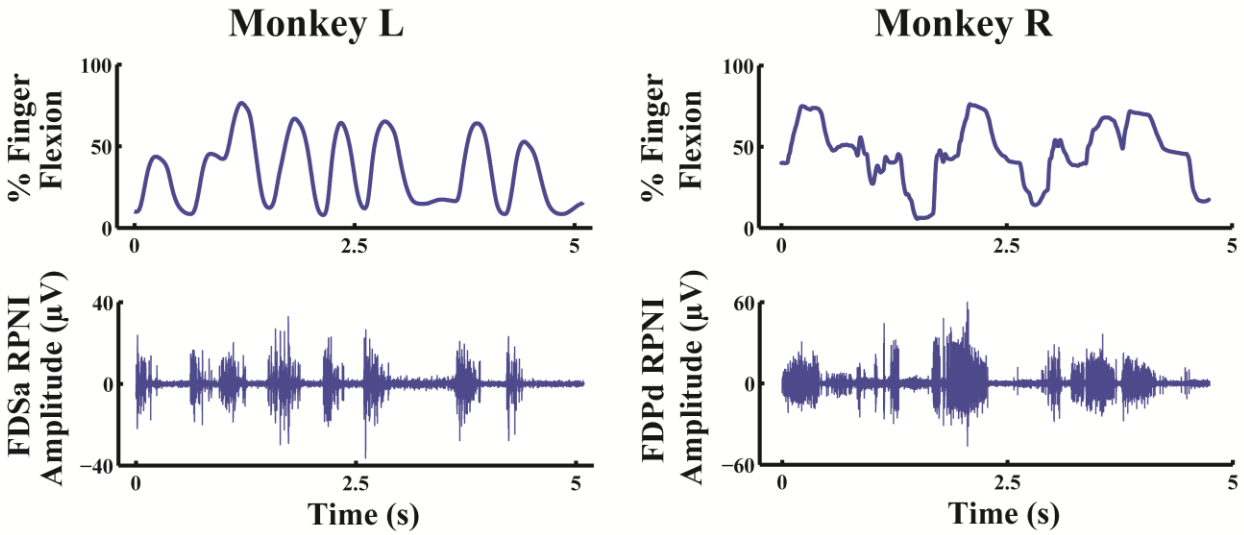

Figure 2.7. Example EMG recorded from acute fine-wire electrodes in both monkeys, showing signals which are qualitatively similar to those of the IM-MES recordings (although the fine-wire electrodes recorded higher amplitudes from the FDPd RPNI in Monkey R).

2.4.4 RPNIs can provide functional prosthesis control signals

Using a simple Naïve Bayes classifier, we were able to decode RPNI signals both offline and in real-time to allow the monkeys to control a virtual hand. In offline decodes of 280 and 447 successful finger movement trials for Monkey L and Monkey R, shown in figure 2.8 (c), we classified hand posture as either extension, flexion, or rest with an accuracy of 97.9% correct and 96.9% correct, respectively. We used leave-one-out cross-validation to minimize overfitting, and computed signal features using the whole trial (~1.5 s of activity, depending on the directness of the monkey's movement to the target) to ensure the inclusion of the maximum amplitude EMG bursts during movement. Because we used the whole trial for classification, true posture labels were based on the target position for that trial, whether or not the monkey moved monotonically towards the target.

Online classification was performed with both monkeys using 50 ms bins. To remove jitter on the output, we required four identical, consecutive decodes before changing the final classification. An example online decode is shown in figure 2.8 (a) for Monkey L. The classifier accurately transitions between movement states, depending on the monkey's current hand posture. Notably, the decode is relatively robust to noisy behavior, correctly classifying rest posture even when the monkey over- or under-shoots the neutral target (i.e. 50% flexion). This indicates that a deliberate attempt at movement was required for correct classification, minimizing the amount of false-positive detections, which may be a desirable trait in a final myoelectric controller.

To quantify the ability of this classification to provide useful prosthetic control, we allowed the monkey to perform the behavioral task in both physical control (in which the virtual hand is controlled by the monkey's actual movements) and closed-loop RPNI control (in which the virtual hand is controlled by the online classifier output). Monkey L's success rate and trial completion time (averaged over a 50-trial window) are shown in figure 2.8 (b), during physical and RPNI control. The required hold time for a successful target acquisition was 700 ms (equivalently, at least 14 consecutive correct classifications). Because the trial timeout (after which the trial was declared unsuccessful) was a relatively long 10 sec, the monkey's success rate was generally near 100%. However, the average trial completion time during physical control was 1.5 sec and was 1.4 sec during RPNI control, indicating that the monkey was able to perform the task equally well with either controller. Note also that there is no obvious adjustment

period when first switching to RPNI control, demonstrating the natural, physiologic control provided by the RPNIs. Finally, the sharp decrease in performance at the end of the experiment is a result of the monkey losing motivation, and not due to the controller.

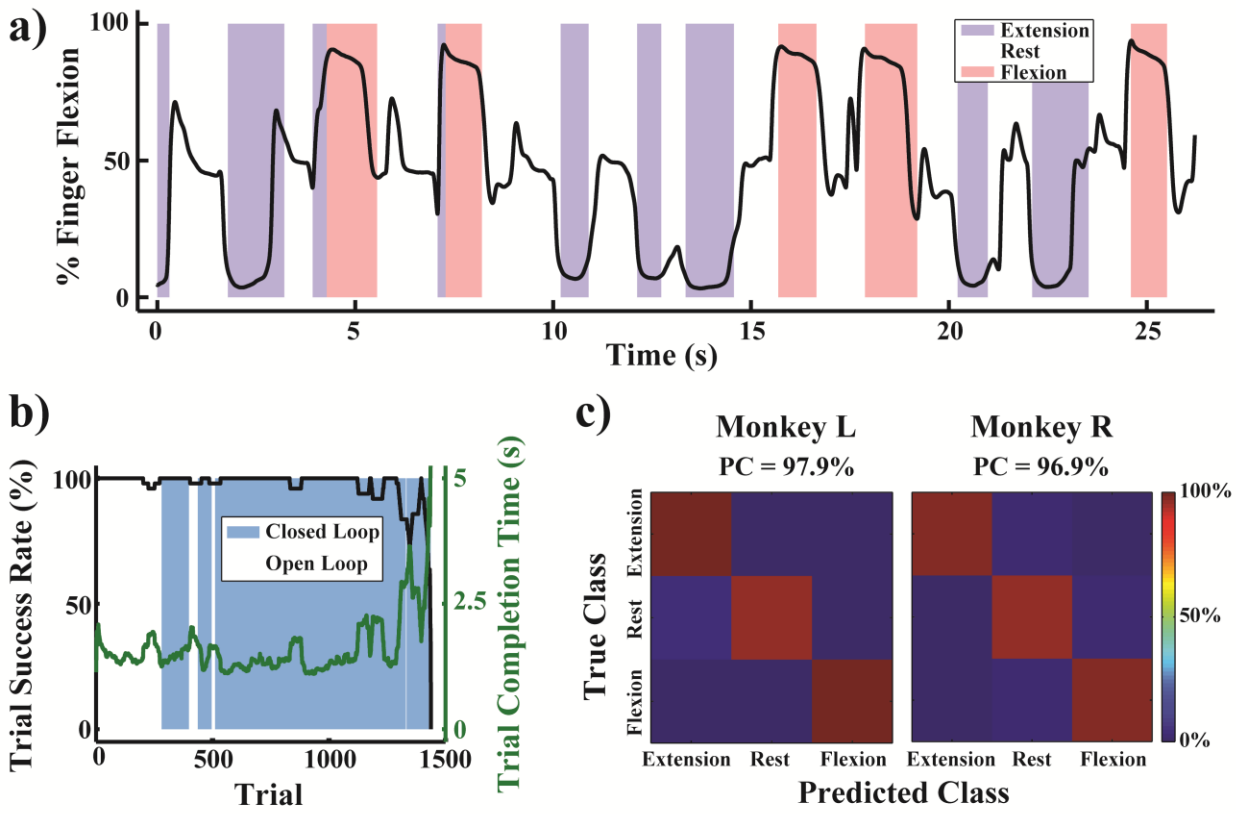

Figure 2.8. Classification of finger movement state using IM-MES electrodes: (a) Online, open-loop during Monkey L task behavior – predicted movement state is overlaid as background on a trace of the monkey's actual finger movements. (b) Monkey L's task performance during physical control (white background) and closed-loop RPNI control (blue background). (c) For both monkeys, offline classification accuracy on the same day as the online experiment, using whole-trial data.

2.5 Discussion

We have provided compelling initial safety data for the RPNI technique in two non-human primates, demonstrating that the implantation of nine RPNIs caused no health concerns and did not noticeably affect the normal function of un-modified anatomy. Further, we have shown that this approach produces healthy tissue which generates normal electromyographic signals with a high signal-to-noise ratio. These signals could be easily recorded using acute or chronically-implanted electrodes and decoded into functional prosthesis commands, showing promise as a capable, intuitive control source. The behavioral task and decodes presented here

are a single degree of freedom, making it substantially equivalent to commercial products which provide “open” and “close” signals.

Though promising, further investigation is required to answer some remaining questions. Primarily, the number of independent signals produced by the RPNIs could not be verified due to the requirements of monkey behavioral training. Thus it remains to be seen whether fully independent signals can be obtained from each RPNI, and whether this would enable the simultaneous control of multiple degrees-of-freedom. Further, the RPNIs were implanted in able-bodied monkeys and great care was taken to minimize any resulting motor deficits, limiting the placement of RPNIs onto small terminal nerve branches which were surrounded by intact muscles performing similar physiological functions. This made it difficult to quantify any potential cross-talk from neighboring muscles. We expect that this effect was minimal, due to the inherent selectivity of intramuscular electrodes, the verification of healthy regenerated RPNI tissue, and previous work in rats (Kung et al., 2014). However, this must be confirmed in future human studies by recording activity that could not be generated by residual anatomy. Finally, in these experiments, we could identify the function of each nerve branch prior to transection. In an actual amputation, nerve functions would be indistinguishable which may cause difficulties in both creation of independent RPNIs and the implementation of decoding algorithms. However, even if full functional separation is not possible, dissecting the nerve as much as possible should enable machine learning algorithms, such as the Naïve Bayes classifier used here, to extract movement intention from the combined activity.

Despite these limitations, this is the first demonstration of prosthesis control via an interface capable of providing stable, long-term physiological control at any level of amputation. Decoding of finger movements and subsequent closed-loop control of prosthetic devices (or the virtual equivalent) has been previously demonstrated using both surface (Tenore et al., 2009) and intramuscular (Birdwell et al., 2015; Cipriani et al., 2014; Smith et al., 2014) electromyography. Though these interfaces have resulted in impressively high-performance control, the inherent instability of both surface and percutaneous fine-wire electrodes represents a significant challenge to their clinical implementation. Perhaps more importantly, however, providing intuitive prosthesis control via residual muscle electromyography is not possible for amputees with more proximal injuries.

Direct nerve interfaces, which could be used for any level of injury, have also been used to provide prosthesis control but face their own set of challenges. The two electrode types which have been the most studied in terms of direct nerve recording and subsequent prosthesis control are the longitudinal intra-fascicular electrode (LIFE; [Lawrence et al., 2004]) and the Utah electrode array (Branner and Normann, 2000). Both have been implanted in multiple amputees and used to provide control functionality similar to this study (Gasson et al., 2005; Rossini et al., 2010). However, recorded signal amplitudes were generally small and corrupted by nearby EMG (Clark et al., 2014; Dhillon et al., 2004). Though these issues could be somewhat mitigated by further signal processing (Clark et al., 2014; Micera et al., 2011) or physical shielding of the array (Clark et al., 2011), successful recording and control have not been demonstrated for longer than one month, with questions remaining as to nerve health under longer-term implantation of these electrodes.

Given these issues, the signal strength, stability, and longevity of the RPNI technique demonstrates promise as a clinically-viable technology. In the future, by combining intramuscular electromyography for any residual muscles (in order to utilize all possible signal sources), RPNI implantation for amputated nerves, and a wireless implantable recording device, we can potentially restore full, effective control of a lost limb for the lifetime of the patient.

CHAPTER III

Cortical Decoding and Control of Precise Fingertip Position in a Rhesus Macaque

A version of this work is currently in preparation to submit for review and publication.

3.1 Abstract

Intracortical brain-machine interfaces (BMIs) are a promising source of prosthesis control signals for individuals with severe motor disabilities. Previous BMI studies have primarily focused on predicting and controlling whole-arm movements; restoration of hand movement, however, has been mostly limited to coarse binary control of simple grasps. In order to investigate the continuous decoding of isolated, precise finger movements, we have developed a novel behavioral task paradigm which requires the subject to acquire virtual fingertip position targets. During task performance, we recorded neural spikes from Utah electrode arrays in primary motor cortex. Using a standard Kalman filter, we could reconstruct continuous finger movement offline with an average correlation of $\rho = 0.79$ between actual and predicted position across three rhesus macaques. For one of the monkeys, this decode was performed in real-time to enable closed-loop neural control of the virtual hand. Compared to physical control, neural control performance was slightly degraded; however, the monkey was still able to successfully perform the task with a target acquisition rate of 79.3% across two sessions. BMI-enabled information throughput during closed-loop performance was 0.83 bits/s, which is similar to previous studies of whole-arm decoding using a standard Kalman filter. This is, to our knowledge, the first demonstration of closed-loop neural control of finger-level fine motor skills. We believe that these results represent an important step towards full and dexterous control of neural prosthetic devices.

3.2 Introduction

Intracortical brain-machine interfaces (BMIs) are a promising source of prosthesis control signals for individuals with severe motor disabilities. By decoding neural activity into intended upper-limb movement, BMIs have enabled both able-bodied monkeys and humans with

tetraplegia to control computer cursors (Gilja et al., 2012; Jarosiewicz et al., 2015; Kim et al., 2008) and high degree-of-freedom robotic arms (Hochberg et al., 2012; Velliste et al., 2008). However, these studies have primarily focused on predicting and controlling whole-arm movements; restoration of hand movement has been mostly limited to coarse binary control of one (Collinger et al., 2013; Velliste et al., 2008) or several (Wodlinger et al., 2015) grasp types. Though this type of binary grasp control is useful in the short term, providing the ability to interact with simple objects in the environment, true restoration of natural movement requires continuous, volitional control of hand and finger kinematics. One participant in an ongoing clinical trial has been able to use imagined and physical index and thumb movements to control a computer cursor (Gilja et al., 2015), but this was not performed in the context of prosthesis control and there was no discussion of the fidelity of finger movement reconstruction.

Several groups have investigated offline decoding of continuous finger-level movements from primary motor cortex in monkeys. By recording neural activity during reach-to-grasp behavioral tasks, in which the monkey reaches for different objects using unique grasps, later reconstruction has been demonstrated of 18 (Aggarwal et al., 2013), 25 (Vargas-Irwin et al., 2010), and 27 (Menz et al., 2015) joint angles of the arm and hand simultaneously. The ability to decode many degrees of freedom with relatively high accuracy is encouraging for future dexterous BMIs, but the inherently variable and imprecise movements generated by the reach-to-grasp task make analysis of the potential controllability of the decode difficult. Further, movements of the hand and fingers during this task are not isolated, but rather are coincident with more proximal movements of the elbow and shoulder (Schaffelhofer et al., 2015). This simultaneous movement may be a confounding factor for decoding, making it unclear whether accuracy would be maintained in other behavioral contexts.

To study isolated finger movements in the early 1990s, Schieber introduced a manipulandum allowing the measurement of individual finger flexion and extension over a range of a few millimeters by actuating force sensors and micro-switches (Schieber, 1991). This paradigm has been used successfully by several groups to classify multiple hand and wrist movements (Egan et al., 2012; Hamed et al., 2007), and continuously decode the instantaneous position of all five digits simultaneously offline (Aggarwal et al., 2009). However, as the range of movement measured by the manipulandum is severely limited, generalization to natural movement is not possible.

These studies have demonstrated the potential for extracting finger-level information from neural activity, but the extracted information has not been used to provide functional control to a subject. This requires a transition to closed-loop task performance, in which the task is completed using the decoded rather than physical movements and the subject can act to change and correct the decode in real time. However, it is not possible for the BMI decode to affect a task which depends solely on interactions with physical objects, whether grasping objects or closing switches. In order to address this issue, virtual reality simulators have been developed in which behavioral tasks can be performed through an avatar (Aggarwal et al., 2011; Putrino et al., 2015). In these systems, avatars could be actuated via either physical movements or decoded movements, enabling both open-loop and closed-loop assessment of BMI performance. Though promising, these systems have not yet been used for this purpose.

We have used this virtual reality paradigm to develop a novel finger-level behavioral task in which a monkey acquires fingertip position targets. Here, we used this task to investigate the continuous decoding of precise finger movements from primary motor cortex, isolated from confounding movements of the upper arm. We analyzed the resulting data in order to study the inherent kinematic tuning of motor cortex neurons during finger movements and identify the optimal parameters for decoding those movements. We used these results to present the first demonstration of closed-loop neural control of fingertip position.

3.3 Methods

All procedures were approved by the University of Michigan Institutional Animal Care and Use Committee.

3.3.1 Behavioral task

We trained three rhesus macaques, Monkeys S, P, and L, to perform simultaneous movements of all four fingers to hit fingertip position targets in a virtual environment, as illustrated in figure 3.1. The monkey sat in a shielded chamber with its right arm at its side, forearm flexed 90 degrees and resting on a table. The monkey's palm was lightly restrained facing to the left, with the fingers free to move unimpeded. A flex sensor (Spectra Symbol, West Valley City, UT) was attached to the index finger, covering all three joints, in order to measure the finger position. Position data were read by a real-time computer running xPC Target (Mathworks, Natick, MA). A computer monitor directly in front of the monkey displayed a

virtual model of a monkey hand (MusculoSkeletal Modeling Software; MDDF, Los Angeles, CA), which was actuated by the xPC in order to mirror the monkey's movements.

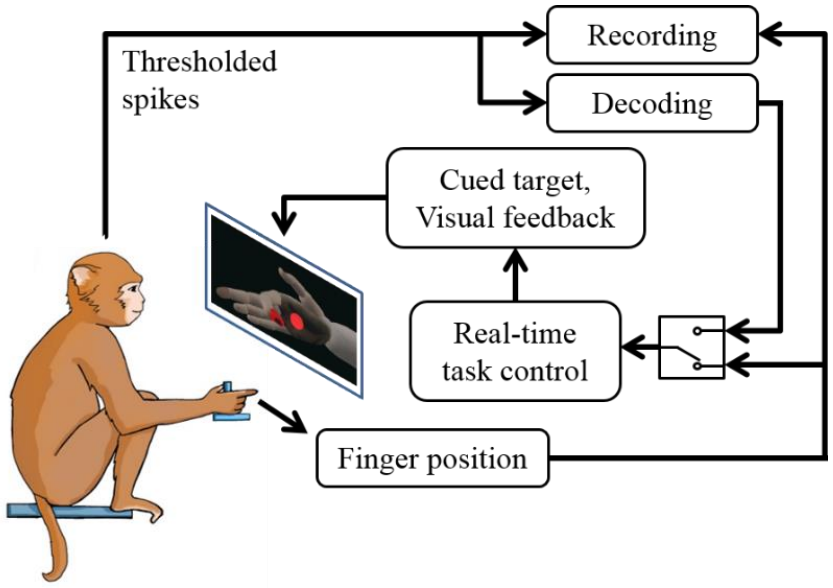

Figure 3.1. Behavioral task illustration. The monkey performed simultaneous flexion and extension movements of the four fingers in order to hit virtual targets on a computer screen. The virtual hand could be controlled either through physical movements, measured via flex sensor, or through decoded movements based on the thresholded neural spikes.

At the start of each trial, the xPC cued a spherical target to appear in the path of the virtual finger, and the monkey was required to move its fingers in order to hit the target and hold for a set period (100-500 ms, depending on the stage of training). Only the index finger was instrumented with a flex sensor, but the monkeys made movements with all four fingers simultaneously. Targets could be generated in one of two patterns, flex-extend or center-out. In the flex-extend pattern, which was the first task learned by each monkey, targets were presented in positions requiring either full flexion or full extension in alternating trials. In the center-out pattern, a target was initially presented in the neutral or rest position, half-way between flexed and extended. Once the monkey successfully acquired this target, a second target was pseudorandomly presented in one of six positions requiring differing degrees of flexion or extension. After this target was successfully acquired or the trial timed out, the neutral target was again presented until successful acquisition.

3.3.2 Electrophysiology

We implanted each monkey with intracortical electrode arrays in the hand area of primary motor cortex, as identified by surface landmarks. The genu of the arcuate sulcus was identified in the craniotomy, and a line was traced posteriorly to central sulcus. Arrays were placed on this line just anterior to central sulcus, as allowed by vasculature. Diagrams of each implantation are shown in figure 3.2. Implantations (array types and locations) were determined by experimental need, resulting in variation between animals. Monkey S received two 96-channel Utah arrays in motor cortex. Monkey P received one 96-channel Utah array and one 16-channel FMA (MicroProbes) in motor cortex, and two 16-channel FMAs in sensory cortex. Monkey L received two 96-channel Utah arrays, one in primary motor and one in primary sensory cortex.

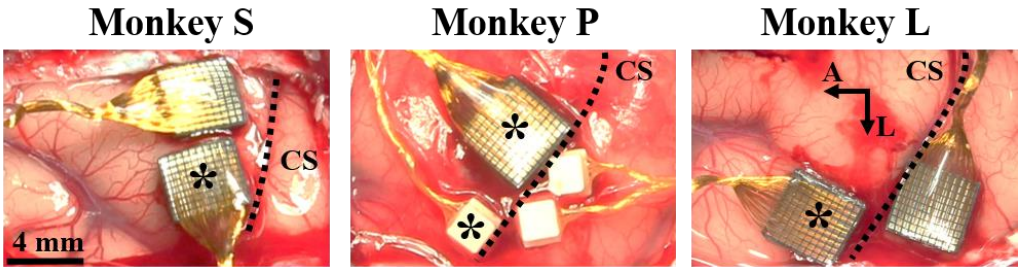

Figure 3.2. Surgical photos of each monkey's electrode array placement. Asterisks indicate arrays used for analysis. CS – central sulcus, A – anterior, L – lateral.

During experimental sessions, we recorded broadband data at 30 kS/s using a Cerebus neural signal processor (Blackrock Microsystems). Neural spikes were detected by thresholding at -4 times the RMS voltage on each channel, after high-pass filtering the broadband data at 250 Hz. Thresholded spikes were simultaneously recorded for offline analysis and streamed to the xPC for online decoding

3.3.3 Decoding

Offline, we used a linear Kalman filter (Wu et al., 2006) to decode continuous finger position from the thresholded neural spikes. Mean hand kinematics and neural firing rates were computed in consecutive, non-overlapping time bins. Hand kinematics at time bin t are collectively described by the hand state vector, $\boldsymbol{X}_t = [\, p, v, 1 \,]^T$, where p is the finger position as directly measured by the flex sensor and v is the finger velocity as calculated by the first

difference of position. Firing rates for each channel at time t are collected in the neural population activity $\boldsymbol{Y}_t = [\, y_1, \ldots, y_n \,]^T$, where y_k is the firing rate of the k^{th} channel. In the Kalman framework, hand state is modeled as a linear dynamical system with neural activity modeled as a noisy transformation of the current hand state, as described by,

$$\boldsymbol{X}_t = \boldsymbol{A}*\boldsymbol{X}_{t-1} + \boldsymbol{w}_t \qquad (1)$$

$$\boldsymbol{Y}_t = \boldsymbol{C}*\boldsymbol{X}_t + \boldsymbol{q}_t \qquad (2)$$

where $\boldsymbol{A}$ is the state transition matrix, $\boldsymbol{w}_t$ is the process noise, $\boldsymbol{C}$ is the observation transformation matrix, and $\boldsymbol{q}_t$ is the observation noise. Noise terms $\boldsymbol{w}_t$ and $\boldsymbol{q}_t$ are assumed to be drawn from individual Gaussian distributions with zero mean and covariance $\boldsymbol{W}$ and $\boldsymbol{Q}$, respectively.

In all cases, we used 10-fold cross-validation to avoid overfitting, training and testing the Kalman filter on separate sets of contiguous trials from the same day. For each monkey, one experimental day was set aside for optimizing decoding parameters. Optimal settings learned on this day were then applied to each testing day. The optimized parameters were the bin size, the time lag (the physiological delay between neural firing rate and kinematic measurements), and the kinematic tuning (whether modeling firing rates as being tuned to position only, velocity only, or both simultaneous resulted in a better decode).

3.3.4 Closed-loop neural control

To determine the functional utility of the offline finger decodes, we enabled one monkey to perform the behavioral task in closed-loop neural control, using a real-time decode of finger position. For each experimental session, Monkey L performed the center-out task using physical movements for ~200 trials. The algorithm was trained on this set of data, and was run in real-time for the rest of the experiment. During closed-loop trial blocks, the virtual hand was controlled using the decoded finger position instead of the monkey's actual finger movements. The task remained the same, with slightly larger targets to make the task slightly easier and provide motivation for the monkey to continue.

For computational efficiency, we used the steady-state Kalman filter (Dethier et al., 2013; Malik et al., 2011) for online decoding. The only difference between the steady-state filter and the standard filter used offline is that the steady-state Kalman gain is pre-computed during training. In practice, the Kalman gain, though updated every timestep in the standard filter,

depends only on the constant matrices ***A***, ***C***, ***W***, and ***Q***, and quickly converges to its steady-state value. When compared to the standard filter both offline and online in closed-loop, both the gain matrices and the kinematic predictions generally converged within 5 s (Malik et al., 2011). Thus, to compute the gain matrix during training, the gain update step of the Kalman algorithm was iterated for the equivalent of 5 s, and the final matrix saved for online use.

To evaluate the performance of the closed-loop decode, we computed several metrics including trial success rate, time to successful target acquisition, and bit rate via Fitts's law (Thompson et al., 2014), and compared them to those computed during physical task control.

3.4 Results

3.4.1 Kinematic data and neural tuning

Examples of kinematic and neural data recorded during task behavior are shown in figure 3.3, for both the flex-extend and center-out tasks. Neural modulation can be seen in both tasks. The flex-extend task paradigm was used as an intermediate step in training, and thus the behavior is both simpler and generally performed faster than the center-out task.

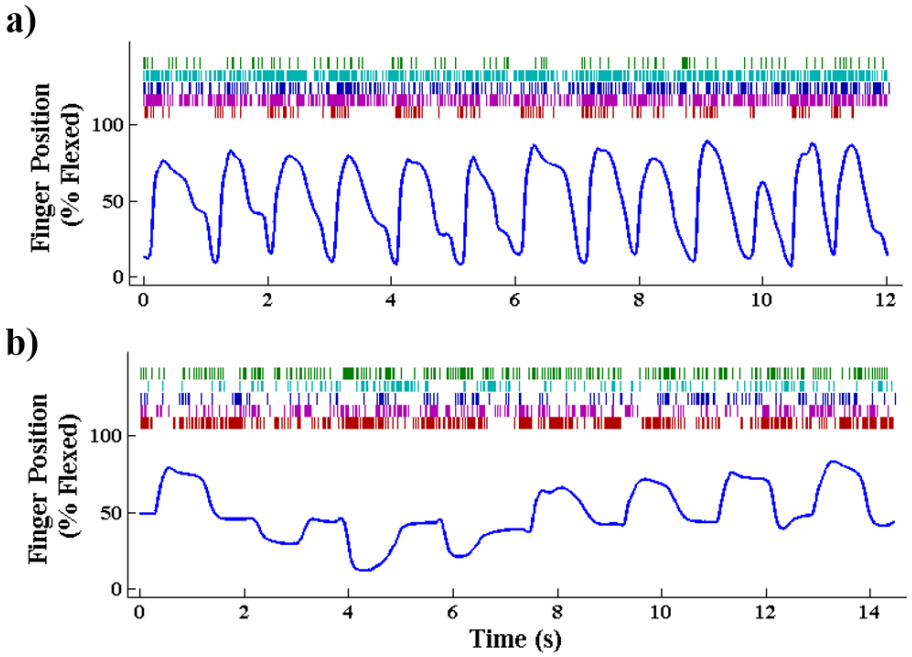

Figure 3.3. Task behavior and associated neural spikes from (a) Monkey P performing the flex-extend task and (b) Monkey L performing the center-out task. Each spike raster displays five separate channels, chosen to be exemplary of modulated activity in each monkey.

To examine the kinematic tuning of each channel, we computed the correlation coefficient (Pearson's r) between the kinematic data (position, velocity, and speed) and each single neural channel binned at 100 ms. To account for the preferred time lag of each channel, we repeated the calculation with multiple lags, from 0 ms to 200 ms, for each kinematic variable and recorded the maximum correlation. Figure 3.4 shows the distribution of correlation values with each kinematic variable.

Kinematic correlations with single channel firing rates were generally low, as expected due to the stochastic nature of the neural data. Though tuning was widely variable between monkeys, movement speed, rather than velocity, was the best represented parameter in each case. The relative tuning strengths of position and velocity were different in all three monkeys, with Monkey P's neurons tuned more to position, Monkey S's neurons tuned more to velocity, and Monkey L's neurons having little tuning to either parameter individually. It is unknown if this represents true neural variability in primary motor cortex, or if it is mainly a result of variable array placements. Interestingly, the tuning distribution in Monkey L appeared to change between behavioral tasks (the data for Monkey L shown in figure 3.4 are taken from the same day), with more channels becoming tuned to speed rather than position or velocity in the center-out task.

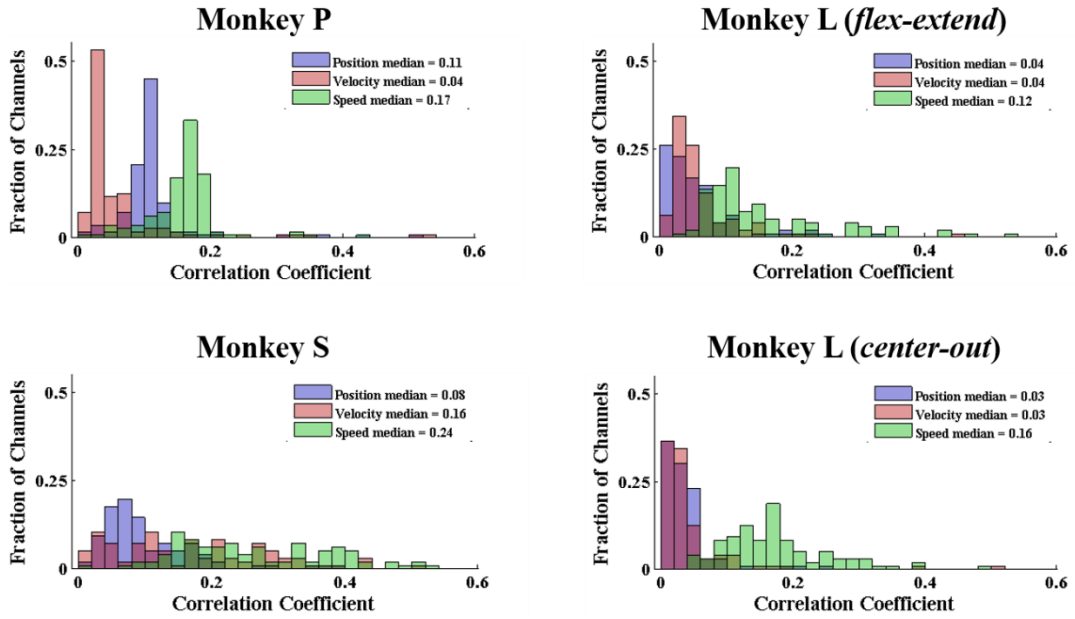

Figure 3.4. Distribution of kinematic tuning for each monkey, as a histogram of correlation values for all single neural channels. Monkeys P and L both performed the flex-extend task, while Monkey L performed both tasks.

3.4.2 Parameter optimization

In order to optimize decoding parameters for each monkey, a grid search of bin size and time lag (from 10-200 ms for each parameter) was performed on an experimental day reserved for this purpose. Using each set of parameters, the Kalman filter was trained and tested with 10-fold cross-validation. In general, performance tended to increase with larger bin size in all three monkeys. Time lags close to zero also tended to be better, but there was more variability between monkeys than for bin size. In each monkey, there was a wide range of "optimal" parameter settings in which the performance level was similar. One of these settings which was close to optimal for all monkeys was a bin size of 100 ms and zero time lag. These parameters are similar to those used previously for decoding of both arm (Cunningham et al., 2011; Kim et al., 2008) and hand (Aggarwal et al., 2013; Menz et al., 2015) movements, and were used for all further offline decoding. As optimal decoding parameters are typically different between offline and closed-loop decoding (Cunningham et al., 2011), closed-loop decoding parameters were optimized separately on each experimental day.

We also investigated the impact of including each kinematic parameter in the Kalman filter model. That is, assuming neural firing rates are related to position only, velocity only, or both simultaneously. The velocity-only filter consistently outperformed the position-only filter; however we found that including both parameters significantly increased decode performance over either single-parameter model. Further, the addition of movement speed did not increase performance over the position-velocity filter, and therefore was not used for decoding.

3.4.3 Offline decoding

Using a standard Kalman filter with these optimal parameters, we decoded several days of experiments for each monkey with an average correlation coefficient of 0.803, 0.858, and 0.709 (for Monkey S, P, and L, respectively) between true and predicted finger position. This performance level is very similar to that reported by previous studies during both reach-to-grasp tasks and limited isolated finger movement tasks (Aggarwal et al., 2009; Menz et al., 2015; Vargas-Irwin et al., 2010). Decode performance for each session is shown in table 3.1, and example traces are shown in figure 3.5 (a-c) for each monkey. For these experimental sessions, Monkeys S and P performed the flex-extend task, while Monkey L performed the center-out task.

Table 3.1. Offline decoding performance.

	S	P	L (center-out)	L (flex-extend)
Session	**ρ (RMSE)**	**ρ (RMSE)**	**ρ (RMSE)**	**ρ (RMSE)**
1	0.827 (0.176)	0.868 (0.121)	0.659 (0.143)	0.795 (0.220)
2	0.772 (0.209)	0.894 (0.119)	0.705 (0.135)	-
3	0.810 (0.182)	0.812 (0.161)	0.763 (0.123)	-
Mean	0.803 (0.189)	0.858 (0.134)	0.709 (0.134)	-

Performance was noticeably lower for Monkey L, which was likely due to the more complex behavioral task. To compare decoding performance between task types, we also decoded one session in which Monkey L performed the flex-extend task. Decode correlation increased relative to the center-out task performed on the same day (0.795 vs. 0.659 correlation), though RMSE also increased (0.220 vs. 0.143) due to the decode "overshooting" near the minimum and maximum finger positions. This change in performance was also seen in the held-out parameter optimization session, though the differences were less dramatic (0.759 vs. 0.733 correlation and 0.189 vs. 0.123 RMSE for the flex-extend vs. center-out tasks). A sample decode from the flex-extend task is shown in figure 3.5 (d). These differences indicate that care must be taken in the design of behavioral task so that the accuracy of movement prediction is not overstated.

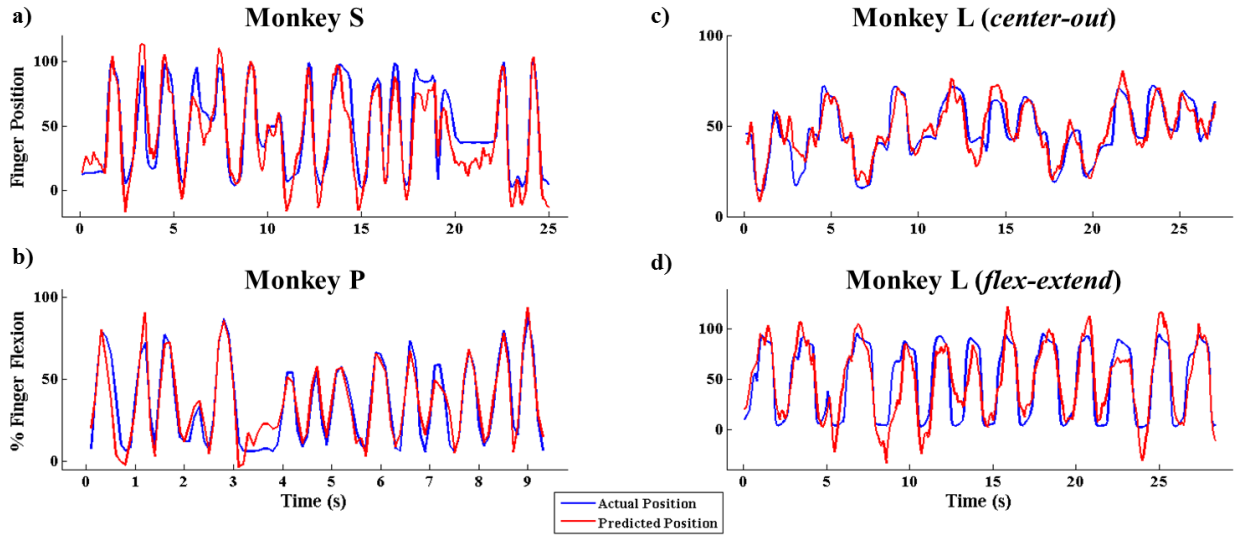

Figure 3.5. (a-c) Sample decodes for each monkey, with the blue trace indicating the true finger position and the red trace indicating the predicted position. (d) Sample decode of the flex-extend task for Monkey L for comparison.

3.4.4 Closed-loop decoding

Following offline testing in Monkey L, we used a steady-state position/velocity Kalman filter to decode movements in real-time during task performance. The filter was optimized and trained on the first ~300 trials of behavior: a number of parameters were tested both offline and in closed-loop. In two days of experiments, 50 and 100 ms bins were used, with 50 and 0 ms of lag. In subsequent blocks of trials, the monkey used either physical movements or the predicted movements in order to perform the task. The required hold time for each target was 500 ms, with a trial timeout of 5 s. A sample of closed-loop task performance is shown in figure 3.6, with both the monkey's actual movements and the predicted movements. The closed-loop decode appeared to be heavily influenced by the monkey's finger velocity, often predicting a return to the rest position when the finger was actually held at a constant flexed or extended position. Despite the often large errors in decoded position, the monkey was able to successfully complete more than 75% of trials, learning to compensate for the erroneous virtual finger motion.

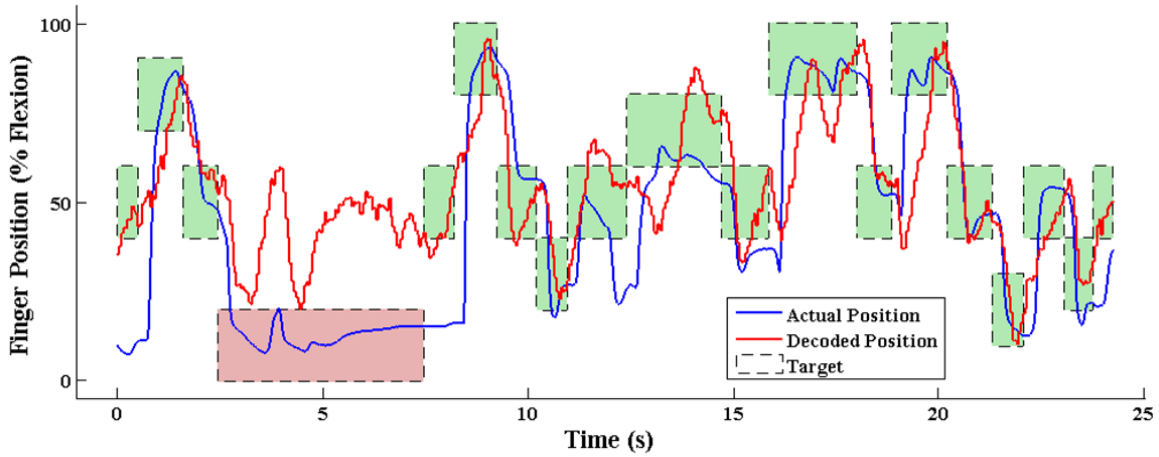

Figure 3.6. Closed-loop control of the behavioral task. The monkey was required to keep the decoded finger position (red trace) within the target zone (dashed boxes) for 500 ms, regardless of the true finger position (blue trace). Target background color indicates the trial success (green) or failure (red).

Several performance metrics for both the open-loop and the closed-loop task are shown in table 3.2. As expected, performance was clearly lower during closed-loop behavior than open-loop with physical control; however, the animal was still able to successfully complete the task, as the target success rate remained >76 % on both days. The average time to complete a trial was longer during closed-loop trials by <0.5 s, which was still well below the trial timeout of 5 s.

Table 3.2. Task performance metrics.

	Success rate (%)		Mean acquisition time (s)		Bit rate (bits/s)	
Session	**Open loop**	**Closed loop**	**Open loop**	**Closed loop**	**Open loop**	**Closed loop**
1	99.2	82.2	1.07	1.52	1.12	0.85
2	98.0	76.4	1.12	1.60	1.09	0.81
Mean	98.6	79.3	1.10	1.56	1.11	0.83

An informative metric when performing continuous selection tasks is the Fitts's law bit rate, which takes into account both the difficulty of the task (how hard the target is to acquire in space) and how quickly the target can be acquired. This metric is fairly robust to variations in tasks (Thompson et al., 2014), and therefore can be compared across algorithms and lab procedures. With a simple Kalman filter, we achieved an average bit rate of 0.83 bits/s, compared to 1.11 bits/s when using the physical hand. This compares well with bit rates reported in the literature for whole-arm BMI performance using the same simple algorithm (see [Gilja et al., 2012] Supplemental Materials for a comparison of estimated bit rates).

3.5 Discussion

Here, we have presented a novel behavioral task paradigm which is designed to enable the detailed investigation of isolated movements of the hand. We used this task to perform the first successful demonstration of continuous decoding of isolated finger movements over the full range of motion. Previous continuous decoding studies have either involved confounding simultaneous movement of the upper-arm or have shown only decoding of very limited movement of the fingers in isolation. Our offline decode performance was similar to these previous reports despite the lack of upper arm movement, confirming that robust information specifically concerning finger-level movements can be extracted from motor cortex. In addition, we have also demonstrated the first closed-loop neural control of finger-level fine motor skills, allowing a monkey to perform a demanding behavioral task using only data recorded from primary motor cortex.

Though these results represent important steps towards restoration of normal upper-limb function, there are still many remaining challenges which can be addressed using our task paradigm. Most critically, the offline decoding accuracy and online task performance must be improved in order to better approximate the abilities of the normal hand. For online decoding, it is probable that using a state-of-the-art algorithm such as the ReFIT Kalman filter (Gilja et al.,

2012) or the neural dynamical filter (Kao et al., 2015) would improve BMI performance. Additionally, even using simpler algorithms as reported here, it is likely the monkey could learn to improve his use of the BMI given sufficient practice (Carmena et al., 2003; Ganguly and Carmena, 2009).

In both cases, however, it is currently unknown if such techniques will translate to finger-level BMIs, and it is likely that some improvement in the underlying decode accuracy will be necessary. The offline reconstruction of finger position presented here appears to accurately capture periods of movement, but tends to overshoot the actual position at the extents of the movement. Further, during periods where the fingers are held in a flexed or extended position, the reconstruction tends to develop a constant offset. Along with our finding of variable kinematic tuning between and within monkeys, these relatively consistent errors may indicate that the assumption of a linear relationship between neural activity and kinematics is not realistic. Indeed, non-linear decoding algorithms relating neural activity to kinematics have generally performed better than equivalent linear models (Aggarwal et al., 2009; Li et al., 2009; Sussillo et al., 2012), and separate studies have indicated that motor cortex activity may fundamentally encode low-level muscle activity rather than extrinsic kinematics (Morrow et al., 2007).

Finally, the movements demonstrated here are simultaneous flexion and extension of all four fingers. This is equivalent to continuous control of a power grasp and is by itself a useful functionality, but it is unclear how this control would change when applied to different grasps or individuated finger movements. It is likely, due to the complex biomechanical constraints of the hand (Lang and Schieber, 2004), that difficulties will arise when directly translating simple linear algorithms to these movements. Modeling these constraints (Kim et al., 2007; Schaffelhofer et al., 2015) and incorporating them into the decoding process may be necessary.

We believe that the results presented here represent an important early step towards full and dexterous control of neural prosthetic devices.

CHAPTER IV

Enabling Low-power, Multi-modal Neural Interfaces through a Common, Low-bandwidth Feature Space

A version of this work has been accepted to IEEE Transactions on Neural Systems and Rehabilitation Engineering, and is currently published online (Irwin et al., 2015).

4.1. Abstract

Brain-Machine Interfaces (BMIs) have shown great potential for generating prosthetic control signals. Translating BMIs into the clinic requires fully implantable, wireless systems; however, current solutions have high power requirements which limit their usability. Lowering this power consumption typically limits the system to a single neural modality, or signal type, and thus to a relatively small clinical market. Here, we address both of these issues by investigating the use of signal power in a single narrow frequency band as a decoding feature for extracting information from ECoG, EMG, and intracortical neural data. We have designed and tested the Multi-modal Implantable Neural Interface (MINI), a wireless recording system which extracts and transmits signal power in a single, configurable frequency band. In pre-recorded datasets, we used the MINI to explore low frequency signal features and any resulting tradeoff between power savings and decoding performance losses. When processing intracortical data, the MINI achieved a power consumption 89.7% less than a more typical system designed to extract action potential waveforms. When processing ECoG and EMG data, the MINI achieved similar power reductions of 62.7% and 78.8%. At the same time, using the single signal feature extracted by the MINI, we were able to decode all three modalities with less than a 9% drop in accuracy relative to using high-bandwidth, modality-specific signal features. We believe this system architecture can be used to produce a viable, cost-effective, clinical BMI.

4.2 Introduction

Brain-machine Interfaces (BMIs) have shown great promise for generating prosthetic control signals in both monkeys (Ethier et al., 2012; Gilja et al., 2012; Velliste et al., 2008) and

humans (Collinger et al., 2013; Hochberg et al., 2012). By decoding neural activity into intended movement, they offer potentially more accurate and natural control than conventional body-powered or surface-myoelectric prostheses. BMIs also have the potential to restore function in cervical-level spinal cord injury, where conventional prostheses are not applicable. However, current BMIs require a percutaneous connection from indwelling electrodes to recording devices outside the body. This introduces several major problems, including potential infection risk and limited user mobility.

To address these problems and move closer to a viable clinical BMI, many groups have designed and built wireless and implantable neural recording systems (Patterson et al., 2004; Rizk et al., 2009; Szuts et al., 2011; Yin et al., 2013). However, none of these systems have thus far been tested in humans or approved by the FDA for clinical use. One major challenge to translating research BMIs into the clinic is the high-bandwidth nature of typical systems, which grant access to the individual neural waveforms. The need to acquire, process, and wirelessly transmit data at rates up to and well beyond 24 Mbps (Borton et al., 2013; Chae et al., 2009) both increases the power requirements of the device and restricts the use of wireless bands like the medical-reserved MedRadio service (which currently limits bandwidth to 6 MHz [CFR Title 47, Part 95.663(d)]).

The high power consumption of current systems results in unacceptably low battery life, unlike other implanted technologies, such as pacemakers, which can operate for years on a single battery (Mallela et al., 2004). Borton et al., for example, developed a fully implantable 100-channel system which transmits broadband data at 24 Mbps and requires 90.6 mW. This device must be recharged every 7 h when using a medical-grade 200 mAh battery (Borton et al., 2013). Miranda et al. similarly built a system which consists primarily of off-the-shelf components and is capable of transmitting 32 channels of broadband data at 24 Mbps for 143 mW (Miranda et al., 2010). Their system lasts for 33 h (Miranda et al., 2010), but requires two 1200 mAh batteries which may be impractical for an implanted device.

One common method of saving power is to reduce the system bandwidth by focusing on only the BMI-relevant features of the input signal, which is typically specific to a particular neural signal type, or modality. For example, electrocorticography-based (ECoG) BMIs commonly use average signal power in particular frequency bands in order to classify intended movement (Chestek et al., 2013; Pistohl et al., 2012). Zhang et al. designed a neural processing

IC which uses this ECoG-specific feature space by extracting and transmitting only the signal power in four separate low-frequency bands, instead of the full broadband signal (Zhang et al., 2011). This type of data compression, along with lowering the front-end bandwidth, resulted in a power consumption of only 6.4 μW for a single-channel system (Zhang et al., 2011).

Commercial electromyography-based (EMG) BMIs use a similar signal feature by thresholding average waveform amplitude for on/off binary decodes (Farina et al., 2014). Hart et al. reported a system containing on-board circuitry to integrate the rectified EMG, allowing for a lower sampling rate and thus reducing the data rate for processing and transmission (Hart et al., 2011). In research-oriented EMG BMIs, pattern recognition algorithms examine waveform temporal features, requiring high sampling rates (Farina et al., 2014; Zhou et al., 2007). However, even these types of BMIs can save power by limiting the analog pass-band to below 1 kHz (Farnsworth et al., 2009; Weir et al., 2009).

Intracortical BMIs typically analyze action potential ("spike") timing. Spikes are detected in the broadband signal, and are binned at regular intervals to produce spike counts. These spike counts can then be used by various decoding algorithms to predict continuous movement (Hochberg et al., 2006; Serruya et al., 2002) or classify intended movement targets (Santhanam et al., 2006). This presents an opportunity for massive data compression, as a system need only transmit spike times instead of the full ~30 ksps waveform, reducing the required data rate by >90 % (Gosselin et al., 2009; Olsson and Wise, 2005; Sodagar et al., 2009). (Chestek et al., 2009) built and tested in vivo a system based on the 100-channel Integrated Neural Interface chip, designed by (Harrison et al., 2009), which contains integrated comparators for on-board spike detection and consumes a total of 8 mW (Harrison et al., 2009). Cheney et al. further limited the outgoing data rate by transmitting spike counts, instead of single detections, at 100 ms intervals (Cheney et al., 2007).

Each of these systems is designed around a modality-specific signal feature, limiting the clinical use of the system to a fairly small market. A cost-effective solution might require a single, multi-modal system which could be applicable to all clinical areas. This paper describes a path to clinical viability by exploring a low-bandwidth feature space common to ECoG, EMG, and intracortical BMIs, which would allow for both low-power and multi-modal implantable systems. ECoG and EMG BMIs are both capable of using band power as the primary decoding feature, but few groups have investigated band power as an alternative to intracortical spikes.

Stark and Abeles found that most, if not all, of the decoding power of spikes could also be extracted from the signal power in a band from .3-6 kHz (Stark and Abeles, 2007). This implies that all three neural modalities can be decoded using individual, low-bandwidth frequency bands. However, there was no discussion in that study of whether the same intracortical information could be found in a narrower band. Also, assessment of the actual power savings of such an approach, and any potential tradeoff in BMI performance, requires a physical device. Dorman et al. designed an intracortical recording device around this feature, using a 1 kHz low-pass filter to pass spike timing information (Dorman et al., 1985), though to our knowledge the device output was never used for decoding.

We have designed and built a low-power, multi-modal neural recording system which extracts the signal power in a single, configurable frequency band and wirelessly transmits that power at regular, BMI-relevant time intervals. We validated the system using novel datasets consisting of EMG and intracortical spikes from rhesus macaques, and ECoG recordings from human subjects. We explored the ability of this low-bandwidth feature space to accurately decode all three modalities, and compared the power requirements of the system to that of more typical high-bandwidth systems.

4.3 Methods

In order to fully explore this feature space, we designed and built the Multi-modal Implantable Neural Interface (MINI), shown in figure 4.1 along with a block diagram of the system. The MINI is designed to extract and transmit the average signal power on each channel at regular time intervals, and can be easily re-configured for a wide range of analog pass-bands, sampling rates, and wireless data rates, summarized in table 4.1.

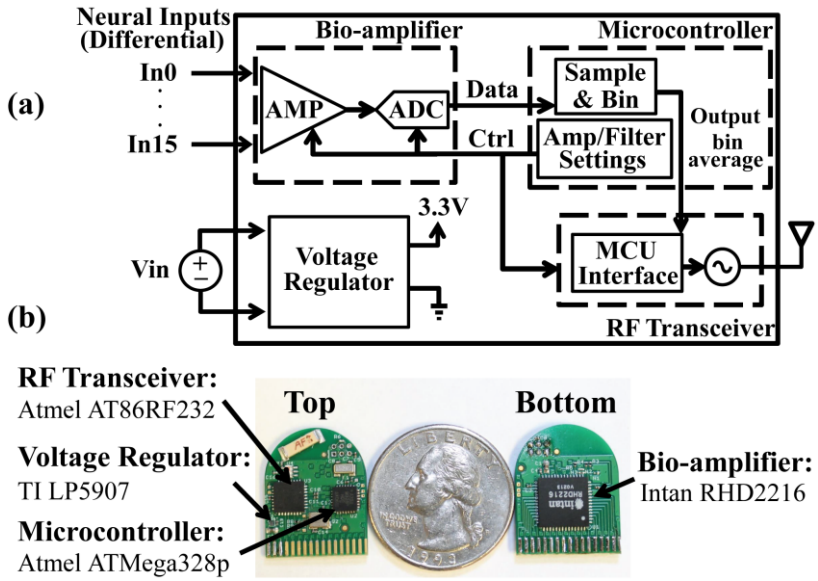

Figure 4.1. (a) Block diagram of the MINI. The average signal power on each channel is computed and wirelessly transmitted at regular intervals. (b) The assembled device with labeled components.

Table 4.1. MINI system specifications.

Parameter	Value
# channels	16 *
ADC resolution	16 bits
Amplifier input-referred noise	2.4 μV_{RMS}
MCU clock	8 MHz
Low-pass filter	0.1 – 20 kHz *
High-pass filter	0.1 – 500 Hz *
Sampling rate	< 5 ksps (16 channels), < 40 ksps (1 channel)*
Wireless data rate	< 250 kbps *
Wireless packet rate	< 500 packets/s (16 channels), < 7500 packets/s (1 channel)
Supply voltage	3.3 V
Typical power consumption	7.5 mW **

* Configurable in software

** Parameter settings: low pass filter – 100 Hz, high pass filter – 500 Hz, sampling rate – 2 ksps, wireless data rate – 4 kbps

4.3.1. System Design

The MINI consists entirely of commercial, off-the-shelf components. The front-end is an Intan RHD2216, a 16-channel bio-amplifier and 16-bit ADC. The amplifier settings and number of active channels can be easily configured by the central microcontroller (MCU) via a standard SPI bus to match the desired signal modality. The lower cutoff frequency of the amplifier bank is selectable from 0.1–500 Hz, while the upper cutoff range is 0.1–20 kHz. The ADC sampling rate

is determined by the MCU, up to a maximum of 5 ksps when using all 16 channels, or 40 ksps for a single channel. The power consumption of the Intan chip scales linearly with the configured filter upper cutoff frequency and the total sampling rate, permitting an analysis of the tradeoff between signal fidelity and MINI power.

The Intan chip also internally computes the absolute value of each channel, which can be used as a simple measure of signal power. During initial decode tests in MATLAB, signal absolute value performed at least as well as more computationally complex algorithms such as mean squared value and root mean squared value for all modalities. The Intan absolute value function was thus used to save costly MCU computational time.

The wireless transceiver is an Atmel AT86RF232, which is compliant with the IEEE 802.15.4 wireless standard and has a maximum data rate of 250 kbps at 2.4 GHz. With 16 channels and 16-bit ADC resolution, signal power can be binned and transmitted off-device roughly every 2 ms, though in typical use the transmission rate is set to ~50 ms. Data and configuration settings are exchanged with the MCU through a second SPI bus.

An 8-bit Atmel ATMega328p MCU serves as the central controller and data processor, configuring the front-end and wireless, as well as controlling the dataflow from sampling to transmission. The MCU is clocked via an internal RC oscillator at 8 MHz, with a 32.768 kHz external crystal oscillator operating asynchronously from the main clock for sampling timing. The MCU itself is programmed from an external computer via a 6-pin in-system interface, and system configuration settings can be easily modified in the application code. Prior to clinical translation, this physical interface could be modified to accept programming via the wireless link.

In typical use, the system is first configured for the desired modality by setting a few simple C macros in the MCU application code: changing the analog pass-band, ADC sampling rate, number of recorded channels, and wireless transmission rate. During operation, the MCU samples and buffers the absolute value of each channel. At the end of each bin period, it computes the average for each channel and passes the data to the wireless transceiver for transmission off-device. Outside the system, a remote recording system receives the data sent at each bin period, which can be stored or input into a decoding algorithm for prosthetic control.

4.3.2 Study Design and Device Validation

We used the MINI to explore the relationship between power consumption and decoding performance, analyzing four datasets containing neural and hand kinematic data recorded during similar finger movement tasks. ECoG data were obtained from two human subjects undergoing invasive seizure-focus mapping, and EMG and intracortical data were obtained from two rhesus macaques performing a separate task. All neural data were recorded using a Cerebus/Neuroport amplifier (Blackrock Microsystems, Salt Lake City, UT) with a similar noise floor to the MINI. Human and monkey protocols were approved by the University of Michigan Institutional Review Board and the University Committee on Use and Care of Animals.

For each modality, we first performed a high-bandwidth decode in MATLAB (Mathworks, Natick, MA) using a typical feature set specific to that modality, and estimated the power required to transmit and extract that feature set. We then, also in MATLAB and using different days' datasets, searched the low-bandwidth feature space to determine the optimal frequency band and sampling rate for decoding each modality. Using that optimal configuration, we replayed the first set of neural data through the MINI, measured the power consumption, and performed a low-bandwidth decode using the output. Finally, we compared both the decode performance and the power difference between high-bandwidth and low-bandwidth approaches within each modality.

4.3.3 Behavioral Tasks

A human subject (P1) undergoing invasive ECoG seizure-focus mapping performed an isometric hand movement task as described in (Chestek et al., 2013). Briefly, in several consecutive trials, the subject was asked to perform and hold a fist grasp, pinch grasp, or flexion of an individual finger for four seconds, before returning to a neutral hand position for an additional four seconds. Hand kinematics were recorded via a DataGlove 5 Ultra (5DT, Irvine, CA) containing flex sensors on each of the fingers. A real-time computer running xPC Target (Mathworks, Natick, MA) coordinated the trial flow and synchronized the behavioral and neural data for offline analysis. A second human subject (P2) performed a passive sensory task, in which one fingertip per trial (thumb, index, or little) was brushed (in one experiment) or pressed (in a second experiment) by the experimenter for four seconds per trial.

Two monkeys performed a continuous finger movement task, illustrated in figure 4.2. Each monkey's index finger was instrumented with a flex sensor (Spectra Symbol, West Valley

City, UT), which fed finger position data to a real-time computer also running xPC Target. A virtual model of a monkey hand was displayed on a monitor in front of the monkey and mirrored the movements measured by the flex sensor. At the start of a trial, the xPC cued a spherical target to appear in the path of the virtual finger, and the monkey was required to flex or extend his finger to hit the target on the screen. After holding the target for ~100 ms, the monkey was given a juice reward. Two targets, respectively requiring full flexion and full extension, were presented to the monkey in alternating trials.

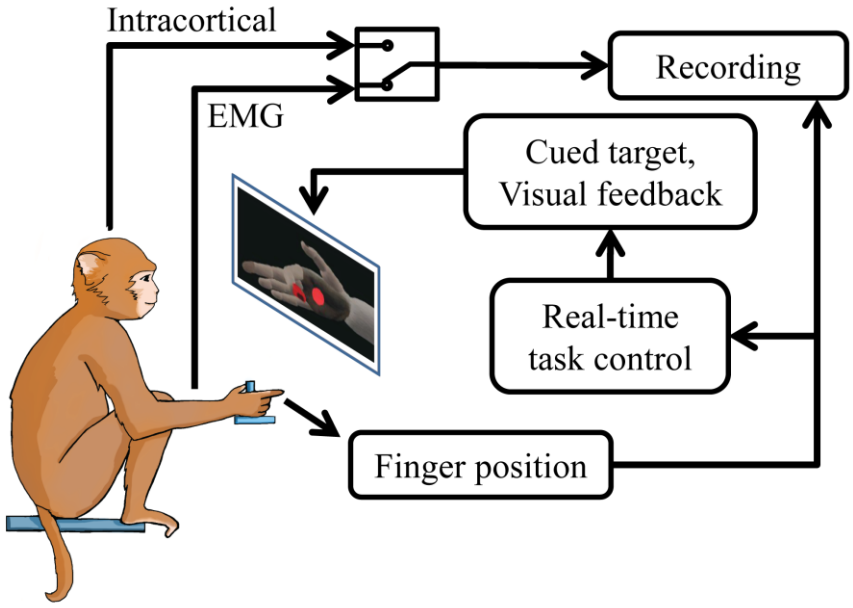

Figure 4.2. Monkey finger movement task. The monkey was required to hit virtual targets by flexing or extending his fingers. Hand movements were measured via flex sensors, and recorded along with either intracortical or EMG data.

4.3.4 Electrophysiology

The two human subjects were implanted with clinical subdural ECoG macroelectrode grids (Ad-Tech Medical, Racine, WI) for seizure-focus mapping. Broadband neural data were recorded during task performance at 30 ksps using a Neuroport signal processor (Blackrock Microsystems, Salt Lake City, UT). Prior to analysis, the neural data were decimated to 10 ksps, and each channel was re-referenced to the common average of its corresponding 32-channel cable into the amplifier (Ludwig et al., 2009). Re-referencing was necessary to remove the noise introduced on the ~3 ft recording cables by the hospital room environment.

Finger flexion-related EMG was recorded from one monkey during task performance via a pair of percutaneous fine-wire electrodes. The differential signal from these electrodes was filtered by a DAM50 amplifier (WPI, Sarasota, FL) between 10–1000 Hz before it was digitized at 30 ksps by a Cerebus neural signal processor (NSP; Blackrock Microsystems, Salt Lake City, UT).

A second monkey was implanted with two 96-channel intracortical Utah arrays in primary motor cortex, shown in figure 4.3, by two neurosurgeons experienced in this procedure. To locate the hand area of motor cortex, we first identified the genu of the arcuate sulcus within the craniotomy and projected a line posteriorly to central sulcus. The first array was placed on this line, just anterior to central sulcus, and the second was placed directly medial to the first. Broadband data were recorded at 30 ksps from the lateral array during task performance using the NSP. Neural spikes were detected by high-pass filtering the raw data at 250 Hz and thresholding the resulting signal at -4.5 times the RMS voltage on each channel.

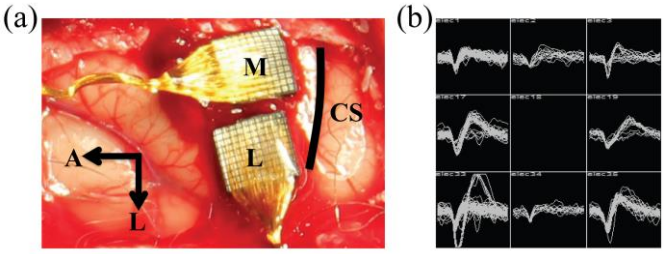

Figure 4.3. (a) Surgical photo of two Utah arrays implanted in motor cortex of a rhesus macaque, medial ('M') and lateral ('L') arrays, (b) representative spike panel from the lateral array, showing well isolated single units.

4.3.5 High-bandwidth Decoding

We analyzed datasets from two separate days for each modality. One was used as a feature selection set, to find the optimal decoding features for each modality, and the other was used as the testing set for both the high-bandwidth and low-bandwidth decodes. No feature selection was performed on the testing set, and each decode was trained and tested on the testing set using cross-validation.

For the ECoG datasets, we classified either which grasp was performed (P1, fist vs. pinch vs. rest), or which finger was stimulated (P2, thumb vs. index vs. little) on each trial. Movement/stimulation onset for each trial was marked by visual inspection of the kinematic data. We used linear discriminant analysis (LDA) to perform the classification, and verified

performance with leave-one-out cross-validation. Our performance metric was percent correct, and we used an equal number of trials for each movement during decoding.

Using the P1 ECoG feature selection dataset, we found grasp-relevant channels by comparing mean gamma (66-114 Hz) power on each channel during separate thumb and little finger flexion movements. We used the five channels with a significant difference between trial types that also corresponded to motor cortex as mapped by clinical microstimulation. To determine the best high-bandwidth feature for decoding, we performed LDA on the same dataset to classify fist vs. pinch grasps, using mean gamma power and beta power (10-30 Hz). We found, similar to several other studies (Chestek et al., 2013; Pistohl et al., 2012), that including beta band activity did not significantly increase classification performance. Similarly, with the P2 ECoG feature selection set, we found the two stimulation-relevant channels that also corresponded to sensory cortex, and confirmed that beta did not increase performance. Thus, our high-bandwidth decoding feature was simply mean gamma power from 0.5 s before to 1 s after movement/stimulation onset.

All subsequent testing was performed on the testing day's datasets. The P1 testing dataset contained 51 total trials. The P2 testing set contained 20 trials. The signal-to-noise ratio (SNR) of these datasets was taken as the ratio of mean gamma activity amplitude surrounding movement onset to that during rest periods. For P1 and P2, the mean SNR of all channels was 1.2 and 1.1, respectively.

For the EMG datasets, we predicted finger flexion onset and offset during a contiguous set of movement trials. The testing dataset contained 95 trials (756 time bins). The SNR was taken as the ratio of mean EMG amplitude during finger flexion to that during extension and rest, resulting in an SNR of 5.8 for the testing set. True movement onset and offset times were marked via visual inspection of the kinematic data prior to decoding. Each trial was split into consecutive 64 ms time bins, and we used LDA (with 10-fold cross-validation) to predict whether the monkey was flexing or not during each bin. The performance metric was again percent correct, where decode points were marked as correct if onset or offset was correctly detected within 150 ms and the decode remained constant until the next onset or offset. For the high-bandwidth decode, we first filtered the broadband EMG between 100-500 Hz. We then extracted four temporal features of the EMG waveform (Hudgins et al., 1993; Zhou et al., 2007) at each time

bin: (1) Average absolute signal amplitude, (2) number of zero crossings, (3) number of slope changes, and (4) waveform line length.

For the intracortical datasets, we used a linear Wiener filter (Chestek et al., 2011) to predict the monkey's continuous finger position. The testing dataset contained 152 trials (1535 time bins). The intracortical SNR was taken as the peak-to-peak amplitude of the largest single unit on each channel to twice the standard deviation of the broadband signal on that channel with isolated spikes removed. The mean SNR of all included channels in the testing set was 6.5. We first binned the neural and kinematic data at 64 ms intervals, and took ten lagged bins of neural data history for each channel. We then performed least squares linear regression to calculate the filter coefficients (Chestek et al., 2011). We performed 10-fold cross-validation for testing, and used the correlation coefficient and root-mean-square error as the performance metrics. Using the feature selection day's dataset, we first determined the optimal set of 16 channels (currently, the maximum capability of the MINI) for decoding by performing backward elimination from the full set of 96 channels (Cecotti et al., 2011). This type of neuron selection has been shown previously to improve decoding performance (Wahnoun et al., 2006). For the high-bandwidth decode, we used binned spike counts on each of the 16 channels. The high-bandwidth feature for each modality is listed in table 4.2.

Table 4.2. Decoding features.

Modality	High Bandwidth Feature	System Configuration	Data Rate	Low Bandwidth Feature	System Configuration	Data Rate
ECoG	Gamma power	< 1 kHz, 2 ksps	512 kbps	Optimal band power	75-150 Hz, 500 sps	4 kbps*
EMG	Temporal features	100-500 Hz, 5 ksps	1.28 Mbps	Optimal band power	200-500 Hz, 2 ksps	4 kbps*
Intracortical	Spike counts	< 7.5 kHz, 20 ksps	3.84 Mbps**	Optimal band power	300-1000 Hz, 2ksps	4 kbps*

* Transmitting a single 16-bit average per channel every 64 ms
** 12 bit ADC resolution

4.3.6 Low-bandwidth Decoding

In MATLAB, using the feature selection datasets, we first found the best individual frequency band for decoding each modality by performing a grid search on the possible upper and lower cutoff frequencies. Using each pair of filter cutoffs, we filtered the broadband data and used the mean signal power on each channel as the decoding feature (using the same methods as

the high-bandwidth decode). After finding the optimal bands, we performed the same decodes again with a range of sampling rates to determine the effect, if any, of sampling over or under the Nyquist rate for each band.

Using each modality's testing dataset, we configured the MINI to use the optimal frequency band and sampling rate for that modality, and replayed the broadband neural data through the MINI using a National Instruments DAC. The DAC output was adjusted via a voltage divider to achieve the original signal amplitude. The MINI output was recorded by a remote wireless receiver and re-synchronized with the kinematics from the same dataset. Finally, the low-bandwidth decode was performed on this new dataset, using the same algorithm and cross-validation process as the high-bandwidth decode for each modality.

4.3.7 Power Comparison

In order to compare the power requirements of implantable systems designed for low-bandwidth vs. high-bandwidth features, we estimated the power consumption of a system with a similar architecture to the MINI, but designed to transmit full broadband data for each modality. As the MINI was designed for low data rates, we estimated the full broadband power assuming an RF transceiver from the same family, the Atmel AT86RF233, with a maximum throughput of 2 Mbps. We kept the assumed system specifications as close as possible to the MINI. Power was calculated based on numbers and equations drawn from each component's datasheet, and depended primarily on the assumed analog filter cutoff, sampling rate, and wireless data rate. Details of the calculation are given in Appendix A.

4.4 Results

4.4.1 System Validation

To validate the real-time performance of the MINI, we recorded in vivo EMG during task performance, while simultaneously recording the full broadband signal with the NSP. The MINI was powered by a single 3.7 V battery, and was configured to filter between 100-500 Hz, sample at 1 ksps, and transmit every 64 ms (250 bps for a single channel). The output of the MINI was wirelessly transmitted to a receiver located ~1 m away, which then sent the received data to the xPC for storage and task synchronization. The MINI output and associated broadband signal are shown in figure 4.4.

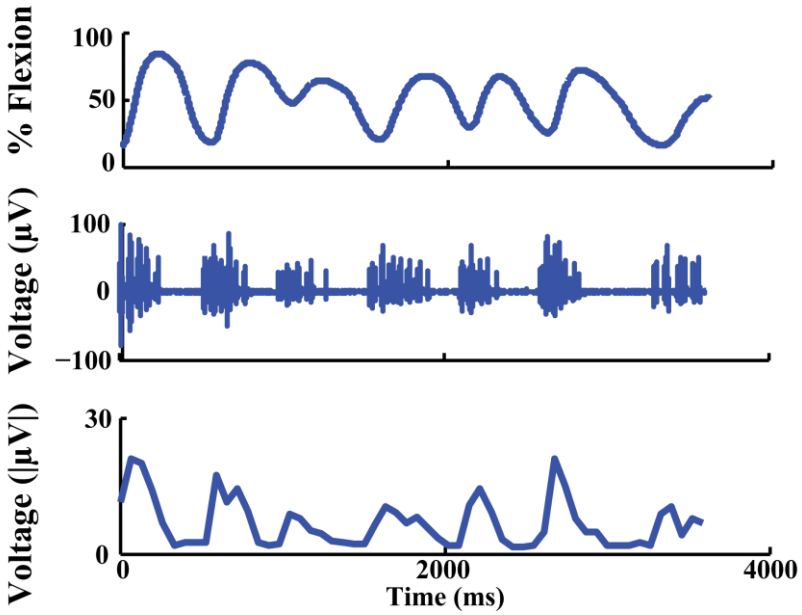

Figure 4.4. Real-time MINI recording of in vivo EMG during task performance. Top trace: monkey finger position (100 = fully flexed, 0 = fully extended). Middle trace: Broadband EMG recorded simultaneously. Bottom trace: MINI output received every 64 ms, representing mean signal power in 100-500 Hz.

We also explored the contribution of each configurable parameter to system power consumption by performing a sweep of the parameter space (amplifier upper cutoff frequency, per-channel sampling rate, and total wireless data rate). During each single parameter sweep, the remaining parameters were held constant at a cutoff of 500 Hz, a sampling rate of 1 ksps, and a wireless bit rate of 4 kbps (transmitting 16 channels of 16-bit data every 64 ms). The individual sweeps are shown in figure 4.5. A linear fit to each curve yields a slope of 0.43 mW/kHz, 2.31 mW/ksps, and 0.29 mW/kbps, respectively.

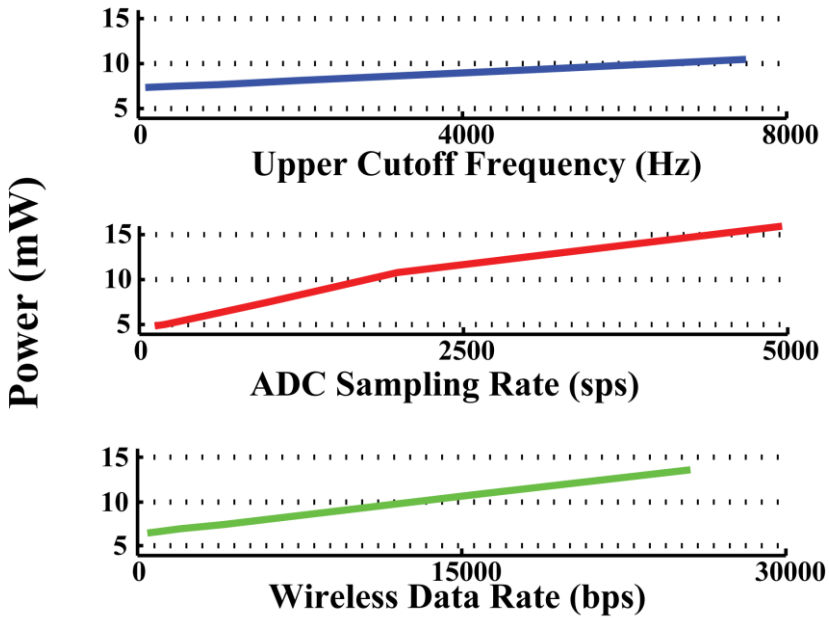

Figure 4.5. MINI parameter sweeps showing the individual contribution of each configuration setting to the overall power consumption. The slope of a linear fit to each parameter is 0.43 mW/kHz, 2.31 mW/ksps, and 0.29 mW/kbps, respectively, from top to bottom.

As each slope is positive, the optimal setting for each parameter is the minimum value which does not significantly decrease decoding ability. In particular, sampling rate appears to be the main driver of power consumption in this system. However, it is primarily limited by the analog upper cutoff frequency, such that we can potentially reduce power consumption by minimizing the cutoff frequency and sampling at the Nyquist rate. Further, the wireless data rate is required to be fast enough that a clinical BMI could respond to neural commands with no noticeable lag, limiting the power optimization of this setting. Thus, the primary target of MINI optimization discussed here is upper cutoff frequency.

4.4.2 Modality I - ECoG

We used ECoG data to classify either which grasp (fist, pinch, or rest) a human subject (P1) performed on a given trial, or which finger (thumb, index, or little) of a second subject (P2) was stimulated. In order to find the optimal MINI filter cutoffs for decoding ECoG data, we performed these classifications in MATLAB using various pass-bands. Decode performance for each subject as a function of the lower and upper cutoff frequency is shown as a heatmap in figure 4.6 (a, d). Only performance values above the diagonal are shown, as by definition the upper cutoff is larger than the lower cutoff. As the sampling rate was shown in figure 4.5 to be

the main driver of power consumption, the optimal MINI configuration should minimize the upper cutoff frequency, allowing the required Nyquist sampling rate to decrease. Thus, the optimal setting can be found from the heatmaps in figure 4.6 as the cluster of high performance values nearest the lower left corner, ~60-120 Hz (black circles in figure 4.6 (a, d)). This identified optimal band did not change considerably when Gaussian white noise was added to the signal prior to decoding in MATLAB.

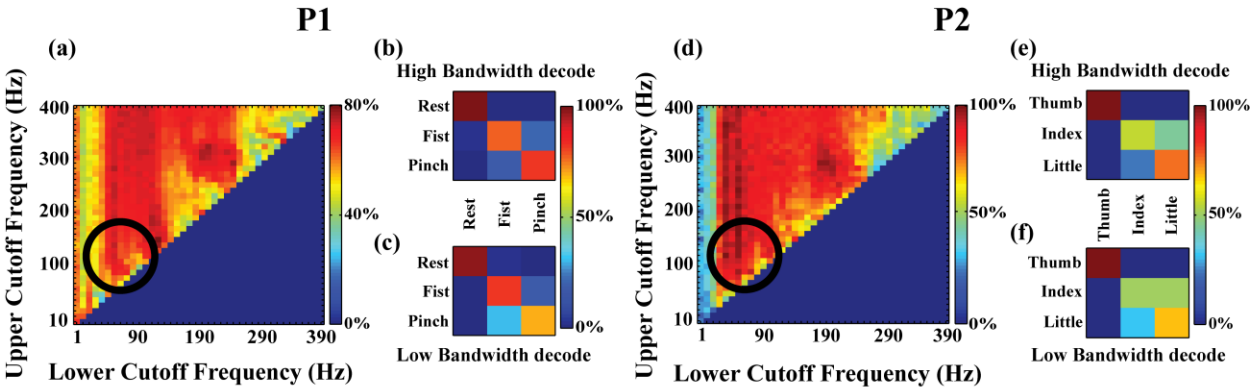

Figure 4.6. (a, d) ECoG decoding performance for P1 and P2, respectively, as a function of the front-end pass-band (black circles mark the optimal pass-band), (b, e) High-bandwidth decode performance as a confusion matrix for P1 and P2 using gamma power (<1 kHz, 2 ksps) – percent correct (PC) = 86.4% for P1, PC = 77.3% for P2, (c, f) Low-bandwidth decode performance for P1 and P2 using the MINI (75-150 Hz, 0.5 ksps) – PC = 83.3% for P1, PC = 72.7% for P2.

Using this pass-band, we repeated the classification for P1 using a range of sampling rates, and found considerable performance decreases when sampling below 500 sps. To provide a decodable output at BMI-relevant timescales, we set the bin period to 64 ms. At 16 channels and 16-bit resolution, this results in a wireless data rate of 4 kbps. These settings are summarized in table 4.2, along with those for the EMG and intracortical modalities.

Using these optimal parameters, we ran the neural data from the testing datasets through the MINI and recorded the output. In this configuration, the MINI consumed 5.9 mW of power. To estimate the power consumption of a system similar to the MINI, but designed to extract the high-bandwidth ECoG feature (gamma power extracted from the broadband data), we assumed an upper cutoff frequency of 1 kHz and a 2 ksps sampling rate. This configuration, listed in table 4.2, would allow for the extraction of all commonly-used ECoG frequency bands (Pistohl et al., 2012). At 16-bit resolution, transmitting 16 channels of broadband would result in a wireless data rate of 512 kbps. The estimated power for this system, using the datasheet from a high-

bandwidth Atmel wireless transceiver from the same family as the MINI transceiver, was 15.8 mW. In this case, the MINI reduced the necessary power by 62.7% of the high-bandwidth consumption.

We decoded the MINI output, as shown in figure 4.6 (c, f), yielding a percent correct (PC) of 83.3% for P1 and 72.7% for P2. We decoded these same datasets in MATLAB using the high-bandwidth ECoG feature, yielding PC = 86.4% for P1 and PC = 77.3% for P2, as shown in figure 4.6 (b, e). Thus for a power reduction of 62.7%, the low-bandwidth MINI decodes represent losses of only 3.6% and 6.0% of the high-bandwidth performance for P1 and P2, respectively. These results are summarized in table 4.3 for each modality.

Table 4.3. Summary of decoding performance and power consumption.

Modality	**Full decoding performance [95% CI]**	**MINI decoding performance [95% CI]**	**Percent change from full decode**	**Full power consumption**	**MINI power consumption**	**Percent change from full power**
ECoG (P1)	PC = 86.4% [70.8, 95.5]	PC = 83.3% [67.2, 93.6]	-3.6%	15.8 mW	5.9 mW	-62.7%
ECoG (P2)	PC = 77.3% [49.0, 94.4]	PC = 72.7% [44.2, 91.8]	-6.0%	15.8 mW	5.9 mW	-62.7%
EMG	PC = 95.3% [93.6, 96.8]	PC = 92.6% [90.2, 94.1]	-2.8%	35.3 mW	7.5 mW	-78.8%
Intra-cortical	$\rho = 0.82$ [0.81, 0.84], RMSE = 0.172	$\rho = 0.78$ [0.77, 0.80], RMSE = 0.186	-4.9%, +8.1%	105.9 mW	10.9 mW	-89.7%

4.4.3 Modality II - EMG

We used EMG data to predict whether or not a monkey was flexing his fingers at a given time point. To find the optimal MINI filter cutoffs for decoding EMG, we performed this decode in MATLAB using various pass-bands. Decode performance is shown in figure 4.7 (a) as a function of the cutoff frequencies. The optimal pass-band was found to be ~200–400 Hz, and was robust to simulated signal white noise. Due to a limited number of filter configuration values on the Intan amplifier, we used a pass-band of 200-500 Hz to best represent this optimal band. Using this band with a range of sampling rates, the optimal setting was the Nyquist rate of 1

ksps. We also used the same wireless data rate as ECoG, transmitting 16 channels every 64 ms (4 kbps).

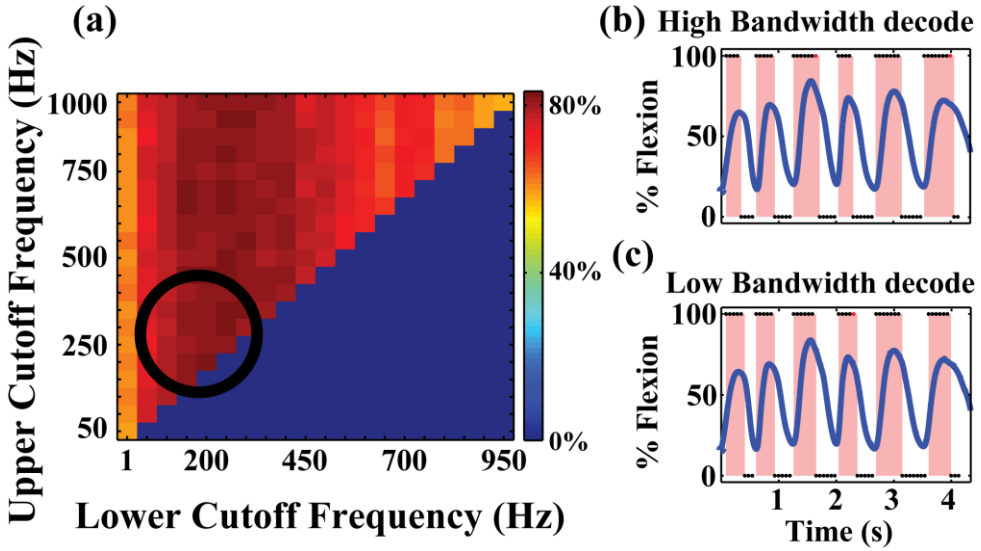

Figure 4.7. (a) EMG decoding performance as a function of the front-end pass-band (black circle marks the optimal pass-band), (b) High-bandwidth decode using temporal waveform features, pink indicates predicted flexion (200-500 Hz, 5 ksps) – percent correct = 95.3%, (c) Low-bandwidth decoding performance using the MINI (200-500 Hz, 1 ksps) – percent correct = 92.6%.

In this configuration, when processing a separate testing dataset, the MINI consumed 7.5 mW of power. To estimate the high-bandwidth system power, we assumed a pass-band of 100-500 Hz and sampling rate of 5 ksps to enable extraction of temporal waveform features. Transmitting 16 channels at 16-bit resolution requires a wireless data rate of 1.28 Mbps. The estimated power for this system was 35.3 mW, indicating that the MINI reduced the necessary power by 78.8%.

Decoding the MINI output resulted in a PC = 92.6%, shown in figure 4.7 (c). Decoding the same dataset in MATLAB using the high-bandwidth EMG feature set yielded PC = 95.3%, as shown in figure 4.7 (b). Thus for a power reduction of 78.8%, the low-bandwidth MINI decode loses only 2.8% of the high-bandwidth performance.

4.4.4 Modality III - Intracortical

Finally, we used intracortical data to predict a monkey's continuous finger position via a linear Wiener filter (Chestek et al., 2011). To find the optimal MINI filter settings for decoding intracortical data, we repeated this decode in MATLAB using various pass-bands. Decode

performance (correlation coefficient) is shown in figure 4.8 (a) as a function of the cutoff frequencies. The optimal pass-band was found to be ~300–1000 Hz, and the optimal sampling rate to be the Nyquist rate of 2 ksps. This is consistent with a view that most of the information in intracortical data can be found in spikes with a ~1 ms sinusoidal waveform. This pass-band sacrifices some potential performance in order to reduce the required sampling rate, and therefore save power. It did not change considerably with simulated white noise conditions. We used the same wireless data rate as previously, 4 kbps when transmitting every 64 ms.

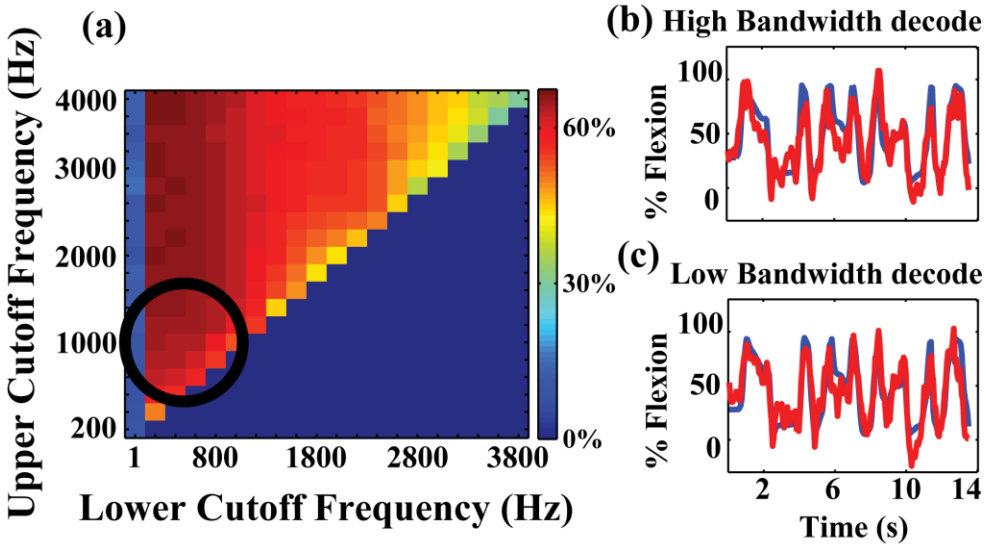

Figure 4.8. (a) Intracortical decoding performance as a function of the front-end pass-band (black circle marks the optimal pass-band), (b) High-bandwidth decode using spike counts, blue trace is the actual finger position, red is the predicted position (<7.5 kHz, 20 ksps) – correlation (ρ) = 0.82 and root-mean-square error (RMSE) = 0.172, (c) Low-bandwidth decoding performance using the MINI (0.3-1 kHz, 2 ksps) – ρ = 0.78 and RMSE = 0.186.

In this configuration, when processing the testing dataset, the MINI consumed 10.9 mW of power. To estimate the power consumed by a high-bandwidth system designed to extract neural spikes, we assumed a pass-band of .1–7500 Hz and a sampling rate of 20 ksps, similar to existing systems (Borton et al., 2013). The resulting data rate for this configuration was 3.84 Mbps when using 12-bit resolution. As this data rate was beyond the 2 Mbps maximum of the assumed transceiver, we further assumed the system to have two identical transceivers, each transmitting the data from eight channels (a per-chip data rate of 1.92 Mbps). The estimated power for this system was 105.9 mW, indicating that the MINI reduced the necessary power by 89.7%.

Decoding the low-bandwidth MINI output resulted in a correlation coefficient (ρ) of 0.78 between actual and predicted finger position, and root mean squared error (RMSE) of 0.186, as shown in 4.8 (c). Using the high-bandwidth feature, spike counts detected in the broadband by thresholding, we decoded the same dataset with $\rho = 0.82$ and RMSE = 0.172, as shown in 4.8 (b). Thus for a power reduction of 89.7%, the low-bandwidth MINI decode loses only 4.9% of the high-bandwidth correlation coefficient and increases the high-bandwidth RMSE by only 8.1%.

4.5 Discussion

We have demonstrated that signal power within a narrow frequency band, sampled below 2 ksps, can be used to accurately decode information from multiple, disparate neural sources. We designed and built a miniature neural recording system to extract this feature, and verified that decoding performance was similar to using high-bandwidth, modality-specific features. Performance decreased by less than 9% when decoding continuous finger movement from intracortical data or when classifying the target of sensory stimulation from ECoG data, and less than 5% when classifying grasp type from ECoG data or when predicting finger flexion from EMG recordings. Further, the decode performances and identified optimal frequency bands were robust to added signal noise. Decoding performance was similar to that reported by other groups using modality-specific features (Aggarwal et al., 2013; Chestek et al., 2013).

In contrast, the power consumption saved when extracting our low-bandwidth feature on-chip relative to a system designed to transmit the full broadband signal varied from 62.8% for ECoG to 89.7% for intracortical. This dramatic decrease in power enables not only longer-lasting devices, but also higher channel counts. Our system was designed to transmit 16 channels of neural data. Assuming linear scaling of power consumption, our system would require only 68.1 mW to transmit 100 channels of intracortical data, ten times less than the 661.9 mW for a broadband design. It remains to be seen whether the information extracted via band power is sufficient for the ultimate restoration of natural movement, or whether neural or muscle action potentials themselves contain critical information, but it is likely that this potential 10-fold increase in channel count would more than offset the performance decrease while maintaining similar power requirements.

It could be argued that low-power ASIC-based systems are capable of enabling viable broadband designs without our approach. Chae et al., for example, designed a 128 channel intracortical system which draws only 6 mW to transmit broadband data below 20 kHz (sampled at 40 ksps) (Chae et al., 2009). Wattanapanitch and Sarpeshkar similarly designed a neural recording IC which digitized 32 channels of intracortical broadband for only 325 μW (a per-channel cost of only 10.2 μW) (Wattanapanitch and Sarpeshkar, 2011). A comparison of these and several other ASIC-based systems to the MINI is presented in table 4.4, clearly showing that an ASIC can achieve much lower power than an off-the-shelf solution such as the MINI.

Table 4.4. Comparison of MINI to intracortical ASIC-based systems.

Reference	No. channels	Upper cutoff frequency (kHz)	Sampling rate per channel (kSps)	Total data rate (Mbps)	Amplifier input-referred noise (μVrms)	Total power (mW)	Power per channel (μW)
(Chae et al., 2009)	128	10	40	90	4.9	6	46.8
(Gosselin et al., 2009)	16	9.2	30	<1	5.4	2.21	138
(Wattanapanitch and Sarpeshkar, 2011)	32	12	31.3	8	5.4	0.325	10.2
(Borton et al., 2013)	100	7.8	20	24	8.6	90.6	906
(Yin et al., 2013)	100	7.8	20	24	2.83	51	510
This work	16	1	2	0.004	2.4	10.9	681

However, these approaches are not mutually exclusive. If power reductions similar to those shown here for the MINI could be applied to the already low-power designs of (Chae et al., 2009) and (Wattanapanitch and Sarpeshkar, 2011), for example, this would result in a total cost of only 618 μW and 33.5 μW, respectively. This puts such systems much closer to being able to operate for long periods on a battery, without inductive charging or with only rare recharges necessary, which would ease the transition into the clinical setting. If higher power consumption is still acceptable, the power savings can be used to increase channel counts and gather information from many more neural sources.

Additionally, producing high-bandwidth data requires excessive hardware on the receiving end, in order to extract the necessary decoding features (a low-bandwidth signal in any case). Systems designed to record and decode neural data entirely inside the body (e.g. functional

electrical stimulation (Hobby et al., 2001)) would be required to either also implant fast, power-hungry processors in order to deal with the added data load, further reducing battery life, or require the patient to use an unnecessary external processor.

Our system demonstrates that accurate, clinically-useful information can be extracted from a feature space shared by the three most commonly used neural modalities, which also allows for a substantial reduction in power consumption. We believe that this represents a viable commercial device architecture by enabling long-lasting and high channel-count implantable systems for use in multiple clinical markets.

CHAPTER V

Discussion

5.1 Conclusion

By tapping into the body's communication pathway in order to generate intuitive control signals, neural interfaces can offer the unique potential of restoring normal hand function to people with severe motor disabilities. However, there are still many challenges left to solve before this technology is a robust and accepted treatment for restoring truly dexterous movement. This thesis attempts to address several of these challenges, in order to bring neural interfaces one step closer to clinical reality.

First, Chapter 2 investigated the ability of a novel peripheral nerve interface, the regenerative peripheral nerve interface (RPNI), to enable the long-term extraction of control signals for hand-level movement. Stable EMG with high signal-to-noise ratio could be recorded from the RPNIs up to 20 months after initial implantation, with no sign of degradation. These signals could accurately detect the intended hand motion, which subsequently enabled the functional control of a virtual hand prosthesis with performance equal to that of the physical hand. The level of control provided by the RPNIs in this initial study is equivalent to current myoelectric prostheses, and demonstrates the potential of the interface as well as providing initial safety data for future human implementation.

In order to provide similar control for paralyzed subjects, in whom the peripheral nervous system no longer contains functional motor signals, Chapter 3 evaluated the fine motor information contained in intracortical signals. Using neural data recorded from primary motor cortex during a novel behavioral task, continuous fingertip position could be accurately reconstructed offline. To our knowledge, this is the first demonstration of continuous neural decoding of isolated hand movement over the full range of motion. Further, this decode could be performed in real-time, and allow the monkey to control a virtual hand in closed-loop in order to move the fingers to arbitrary positions. Again, to our knowledge, this is the first demonstration of volitional control of fine motor skills enabled through a cortical neural interface.

The results presented in these two chapters are encouraging for the success of neural interfaces, but a large hurdle for translating this technology into clinical practice is the development of fully-implantable, wireless devices which can record and transmit neural signals through the skin. This would enable the long-term use of neural interfaces in everyday life, a critical milestone. To this end, Chapter 4 presented the design and testing of the Multi-modal Implantable Neural Interface, a wireless system which extracts and transmits the signal power in a single, configurable frequency band to enable low-power recording of cortical, peripheral, and myoelectric signals. Compared to more typical systems designed to extract and transmit high-bandwidth broadband data, the MINI significantly reduced power consumption while maintaining decode performance for each signal modality. These results indicate that the MINI represents a viable device architecture which could enable clinical neural interfaces for a broad prosthetics market.

5.2 Future Directions

Building on the results presented in this and other works, there are still many questions to be answered and improvements to be made before these technologies are ready for clinical use. Answering these questions will require both human and animal studies. Here, I will attempt to lay out a potential path to clinical reality for peripheral and cortical interfaces, addressing some of the most critical challenges to be solved along the way.

Peripheral nerve interfaces have shown great promise in recent pilot human trials (Clark et al., 2014), but there remain serious concerns about the longevity of current approaches. The RPNI technique as demonstrated in Chapter 2 appears to solve this issue. We have successfully recorded and decoded signals from RPNIs in monkeys up to 20 months after implantation, with no signs of signal degradation. RPNIs have also been implanted in humans for the purpose of neuroma control for more than 2.5 years, and we have recorded and decoded signals from two RPNIs in an amputee up to seven months after implantation.

The primary challenge to be addressed in future human studies is determining the number of independent control signals which can be extracted using RPNIs. In order to maximally separate control signals, the RPNI implantation procedure must include intraoperatively dissecting residual nerves into individual fascicles and isolating them into separate muscle grafts. It remains to be seen whether this can be done to the extent of isolating a single function to each

RPNI, but seems likely at least for more distal amputations, in which the nerve fascicles are relatively segregated and somatotopic (Stewart, 2003). For more proximal amputations, where fascicle grouping is less clear, implanting multiple electrode contacts into each RPNI may be necessary for extracting intermingled functions.

Secondly, in order to restore truly natural movement, it is necessary to provide simultaneous, continuous control of each degree of freedom of the prosthesis. Able-bodied subjects will be required in order to develop and evaluate the decoding algorithms to achieve this. This could be studied in monkeys with RPNI implants, but training limitations would restrict decoding to relatively simple movements. As the RPNIs produce normal EMG signals, however, decode studies on able-bodied human subjects with standard EMG techniques may be directly applicable to RPNI control. Initial work in this area has been done by several groups investigating regression algorithms for simultaneous control of 2D wrist movements in able-bodied humans, with promising results (Hahne et al., 2014; Smith et al., 2015). Our initial efforts applying a linear Kalman filter to RPNI signals in monkeys have been similarly promising for finger control, albeit with relatively simple movements.

If these challenges can be solved, providing simultaneous and continuous control of many degrees of freedom, then RPNIs may represent one integral part of the optimal solution for amputation at any level. With a large number of implanted RPNIs, and possibly multiple electrodes in each, an implanted recording system will likely require some form of data compression such as that proposed by the MINI architecture in Chapter 4. The system would then extract only relevant signal features from each channel and wirelessly transmit the data to decoding hardware located in the prosthesis socket. This would minimize power requirements, either extending implanted battery life or minimizing the necessary inductive power transfer, depending on implementation.

Intracortical neural interfaces face a fundamentally different challenge than peripheral interfaces. Interface longevity seems to be less of an issue, with at least some Utah arrays recording useful signals over five years post-implantation (Hochberg et al., 2012; Jarosiewicz et al., 2015); however, the fundamental physiological mechanism by which neural activity produces movement is still unclear. In order to answer this question, it is necessary to record both neural activity and the resulting movement simultaneously, requiring further study using able-bodied monkeys. This is not to say that human studies should not continue or even expand further, as

important achievements are being made, for example, in cursor control for assistive technology (Gilja et al., 2015). Neural plasticity may also obviate the need for biomimetic prosthesis control (Ganguly and Carmena, 2009), in which case current human research in prosthesis control using standard linear algorithms may achieve sufficient performance simply by adding more controllable dimensions (Wodlinger et al., 2015). However, even with the relatively simple movements investigated in Chapter 3, it is unlikely that the reported decode accuracy represents the best performance possible. Rather, it may simply be approaching the limit of linear models to approximate the true relationship between neural firing rates and finger kinematics. Thus, there still may be a need for further research into physiological mechanisms in order to achieve adequate performance.

There is currently no consensus about which aspect of movement is fundamentally encoded by primary motor cortex, with possibilities ranging from movement direction (Georgopoulos et al., 1982; Schwartz et al., 1988) to muscle activation level (Morrow and Miller, 2003; Scott and Kalaska, 1995). However, multiple studies have shown that decode performance better generalizes to new task contexts (e.g. reaching with a different arm posture or within a force field) when neural activity is modelled as relating to low-level parameters such as intended joint torque or muscle activity (Cherian et al., 2013; Oby et al., 2013). This indicates that certain non-linearities are present in the path from neural firing to ultimate kinematic output, whether caused by an inherent non-linear encoding in the neural activity itself (Pohlmeyer et al., 2007) or caused by the musculoskeletal mechanics underlying physical movement (Park and Durand, 2008). It seems likely that including musculoskeletal dynamics in the decode path may be necessary for increasing accuracy in unrestricted environments (Kim et al., 2007).

One final challenge for intracortical interfaces, which must also be addressed initially in animal models, is the fact that current electrode arrays sample activity from a tiny, sparse fraction of the neurons in motor cortex. In order to elucidate the true relationship between neural activity and movement, and more faithfully extract movement intention, it may be necessary to develop arrays with higher, denser channel counts. One promising method of increasing channel counts is to use single carbon fibers, which have a small enough diameter to avoid most of the glial scarring common to traditional silicon electrodes (Patel et al., 2015). Using both traditional electrode arrays and future ultra-high density carbon fiber arrays, the novel experimental

paradigm presented in Chapter 3 could enable some resolution of the neural representation debate, and thus allow truly accurate movement decoding.

If high channel counts are indeed necessary for accurate intracortical interfaces, then an implantable system similar to the MINI architecture would be required to allow clinical translation. This system could be used for wireless data compression in order to transmit data outside the body to a prosthesis, or it could lower front-end processing power to enable fully-implanted functional electrical stimulation. This would accommodate either patient preference, limb replacement or restoration.

Both peripheral and intracortical neural interfaces still face a long path to widespread clinical reality, but significant progress has been made in the past decade and, combining this progress with the results of the future work described here, it may soon be possible to restore normal arm and hand function in cases of debilitating injury.

APPENDIX A

Broadband System Power Calculation

Broadband system power was estimated based on a system similar to the MINI, using an Intan RHD2216 amplifier, Atmel ATMega328p MCU, and an Atmel AT86RF233 wireless transceiver. In a simplified model of the system, the amplifier draws a constant current after being configured, the MCU draws a large current when actively retrieving data from the amplifier and is in low-power mode for the rest of the sampling period, and the transceiver draws a large current when actively transmitting and is in low-power mode otherwise.

The amplifier current draw depends only on the configured filter upper cutoff frequency, f_c, and the per-channel sampling rate, f_s. With all 16 channels active, the current is

$$I_{amp} = 710\ \mu A + 121.6\frac{\mu A}{kHz} * f_c + 34.24\frac{\mu A}{ksps} * f_s\ . \qquad (1)$$

The MCU current draw depends both on the MCU clock rate, f_{mcu}, and on f_s to determine the active duty cycle. For the ECoG and EMG modalities, we assumed a clock of 8 MHz in order to achieve the same SPI clock rate (half the MCU clock) as the MINI. For this clock rate, the large active current, I_a, is 3 mA and the low-power mode current, I_s, is 1 µA. The higher sampling rate of intracortical data required the assumption of a higher MCU clock of 12 MHz, increasing I_a to 4 mA. For 16 channels of 16-bit data, MCU current is:

$$I_{mcu} = I_a * \frac{512 * f_s}{f_{mcu}} + I_s * \left(1 - \frac{512 * f_s}{f_{mcu}}\right). \qquad (2)$$

Wireless current assumed it was transmitting at maximum power at 2 Mbps. When actively transmitting, it draws 13.8 mA and draws 0.4 µA for the rest of the sampling period. The time spent in each mode depends on the total amount of data transmitted, N_{bits}. For ECoG and EMG, N_{bits} was 256 bits at 16-bit resolution. For intracortical, the high sampling rate required a further assumption that the system have two identical RF transceivers, each transmitting the data from eight channels at 12-bit resolution. Thus, N_{bits} for intracortical was 96 bits, and the total wireless current draw was doubled.

$$I_{rf} = 13.8mA * \frac{N_{bits} * f_s}{2\ Mbps} + 0.4\mu A * (1 - \frac{N_{bits} * f_s}{2\ Mbps}) \qquad (3)$$

The total broadband system power was then the sum of all component currents multiplied by the supply voltage:

$$P = \left(I_{amp} + I_{mcu} + I_{rf}\right) * 3.3\ V. \quad (4)$$

BIBLIOGRAPHY

Aggarwal, V., Kerr, M., Davidson, A.G., Davoodi, R., Loeb, G.E., Schieber, M.H., Thakor, N.V., 2011. Cortical control of reach and grasp kinematics in a virtual environment using musculoskeletal modeling software, in: 2011 5th International IEEE/EMBS Conference on Neural Engineering (NER). Presented at the 2011 5th International IEEE/EMBS Conference on Neural Engineering (NER), pp. 388–391. doi:10.1109/NER.2011.5910568

Aggarwal, V., Mollazadeh, M., Davidson, A.G., Schieber, M.H., Thakor, N.V., 2013. State-based decoding of hand and finger kinematics using neuronal ensemble and LFP activity during dexterous reach-to-grasp movements. J. Neurophysiol. 109, 3067–3081. doi:10.1152/jn.01038.2011

Aggarwal, V., Tenore, F., Acharya, S., Schieber, M.H., Thakor, N.V., 2009. Cortical decoding of individual finger and wrist kinematics for an upper-limb neuroprosthesis, in: Annual International Conference of the IEEE Engineering in Medicine and Biology Society, 2009. EMBC 2009. Presented at the Annual International Conference of the IEEE Engineering in Medicine and Biology Society, 2009. EMBC 2009, pp. 4535–4538. doi:10.1109/IEMBS.2009.5334129

Anderson, K.D., Fridén, J., Lieber, R.L., 2008. Acceptable benefits and risks associated with surgically improving arm function in individuals living with cervical spinal cord injury. Spinal Cord 47, 334–338. doi:10.1038/sc.2008.148

Biddiss, E.A., Chau, T.T., 2007. Upper limb prosthesis use and abandonment: A survey of the last 25 years. Prosthet. Orthot. Int. 31, 236–257. doi:10.1080/03093640600994581

Biddiss, E., Chau, T., 2007. Upper-Limb Prosthetics: Critical Factors in Device Abandonment. Am. J. Phys. Med. Rehabil. 86, 977–987. doi:10.1097/PHM.0b013e3181587f6c

Birdwell, J.A., Hargrove, L.J., Weir, R.F.F., Kuiken, T.A., 2015. Extrinsic Finger and Thumb Muscles Command a Virtual Hand to Allow Individual Finger and Grasp Control. IEEE Trans. Biomed. Eng. 62, 218–226. doi:10.1109/TBME.2014.2344854

Blabe, C.H., Gilja, V., Chestek, C.A., Shenoy, K.V., Anderson, K.D., Henderson, J.M., 2015. Assessment of brain–machine interfaces from the perspective of people with paralysis. J. Neural Eng. 12, 043002. doi:10.1088/1741-2560/12/4/043002

Borton, D.A., Yin, M., Aceros, J., Nurmikko, A., 2013. An implantable wireless neural interface for recording cortical circuit dynamics in moving primates. J. Neural Eng. 10, 026010. doi:10.1088/1741-2560/10/2/026010

Branner, A., Normann, R.A., 2000. A multielectrode array for intrafascicular recording and stimulation in sciatic nerve of cats. Brain Res. Bull. 51, 293–306. doi:10.1016/S0361-9230(99)00231-2

Branner, A., Stein, R.B., Normann, R.A., 2001. Selective Stimulation of Cat Sciatic Nerve Using an Array of Varying-Length Microelectrodes. J. Neurophysiol. 85, 1585–1594.

Carlson, B.M. and, Faulkner, J.A., 1983. The regeneration of skeletal muscle fibers following injury: a review. [Review]. Med. Sci. Sports Exerc. 1983 15, 187–198.

Carmena, J.M., Lebedev, M.A., Crist, R.E., O'Doherty, J.E., Santucci, D.M., Dimitrov, D.F., Patil, P.G., Henriquez, C.S., Nicolelis, M.A.L., 2003. Learning to Control a Brain–Machine Interface for Reaching and Grasping by Primates. PLoS Biol 1, e42. doi:10.1371/journal.pbio.0000042

Carmena, J.M., Lebedev, M.A., Henriquez, C.S., Nicolelis, M.A.L., 2005. Stable Ensemble Performance with Single-Neuron Variability during Reaching Movements in Primates. J. Neurosci. 25, 10712–10716. doi:10.1523/JNEUROSCI.2772-05.2005

Cecotti, H., Rivet, B., Congedo, M., Jutten, C., Bertrand, O., Maby, E., Mattout, J., 2011. A robust sensor-selection method for P300 brain–computer interfaces. J. Neural Eng. 8, 016001. doi:10.1088/1741-2560/8/1/016001

Cedars, M.G.M.D., Das, S.K.M.D., Roth, J.C.B.S., Miller, T.A.M.D., 1983. The Microscopic Morphology of Orthotopic Free Muscle Grafts in Rabbits. Plast. Reconstr. Surg. 72, 179–187.

Cedars, M.G.M.D., Miller, T.A.M.D., 1984. A Review of Free Muscle Grafting. Plast. Reconstr. Surg. 74, 712–720.

Chae, M.-S., Yang, Z., Yuce, M.R., Hoang, L., Liu, W., 2009. A 128-Channel 6 mW Wireless Neural Recording IC With Spike Feature Extraction and UWB Transmitter. IEEE Trans. Neural Syst. Rehabil. Eng. 17, 312–321. doi:10.1109/TNSRE.2009.2021607

Cheney, D., Goh, A., Xu, J., Gugel, K., Harris, J.G., Sanchez, J.C., Principe, J.C., 2007. Wireless, In Vivo Neural Recording using a Custom Integrated Bioamplifier and the Pico System, in: 3rd International IEEE/EMBS Conference on Neural Engineering, 2007. CNE '07. Presented at the 3rd International IEEE/EMBS Conference on Neural Engineering, 2007. CNE '07, pp. 19–22. doi:10.1109/CNE.2007.369601

Cherian, A., Fernandes, H.L., Miller, L.E., 2013. Primary motor cortical discharge during force field adaptation reflects muscle-like dynamics. J. Neurophysiol. 110, 768–783. doi:10.1152/jn.00109.2012

Chestek, C.A., Gilja, V., Blabe, C.H., Foster, B.L., Shenoy, K.V., Parvizi, J., Henderson, J.M., 2013. Hand posture classification using electrocorticography signals in the gamma band over human sensorimotor brain areas. J. Neural Eng. 10, 026002. doi:10.1088/1741-2560/10/2/026002

Chestek, C.A., Gilja, V., Nuyujukian, P., Foster, J.D., Fan, J.M., Kaufman, M.T., Churchland, M.M., Rivera-Alvidrez, Z., Cunningham, J.P., Ryu, S.I., Shenoy, K.V., 2011. Long-term stability of neural prosthetic control signals from silicon cortical arrays in rhesus macaque motor cortex. J. Neural Eng. 8, 045005. doi:10.1088/1741-2560/8/4/045005

Chestek, C.A., Gilja, V., Nuyujukian, P., Kier, R.J., Solzbacher, F., Ryu, S.I., Harrison, R.R., Shenoy, K.V., 2009. HermesC: Low-Power Wireless Neural Recording System for Freely Moving Primates. IEEE Trans. Neural Syst. Rehabil. Eng. 17, 330–338. doi:10.1109/TNSRE.2009.2023293

Christensen, M.B., Pearce, S.M., Ledbetter, N.M., Warren, D.J., Clark, G.A., Tresco, P.A., 2014. The foreign body response to the Utah Slant Electrode Array in the cat sciatic nerve. Acta Biomater. 10, 4650–4660. doi:10.1016/j.actbio.2014.07.010

Cipriani, C., Segil, J.L., Birdwell, J.A., Weir, R.F., 2014. Dexterous Control of a Prosthetic Hand Using Fine-Wire Intramuscular Electrodes in Targeted Extrinsic Muscles. IEEE Trans. Neural Syst. Rehabil. Eng. 22, 828–836. doi:10.1109/TNSRE.2014.2301234

Clark, G.A., Ledbetter, N.M., Warren, D.J., Harrison, R.R., 2011. Recording sensory and motor information from peripheral nerves with Utah Slanted Electrode Arrays, in: 2011 Annual International Conference of the IEEE Engineering in Medicine and Biology Society, EMBC. Presented at the 2011 Annual International Conference of the IEEE Engineering in Medicine and Biology Society, EMBC, pp. 4641–4644. doi:10.1109/IEMBS.2011.6091149

Clark, G.A., Wendelken, S., Page, D.M., Davis, T., Wark, H.A.C., Normann, R.A., Warren, D.J., Hutchinson, D.T., 2014. Using multiple high-count electrode arrays in human median and ulnar nerves to restore sensorimotor function after previous transradial amputation of the hand, in: 2014 36th Annual International Conference of the IEEE Engineering in Medicine and Biology Society (EMBC). Presented at the 2014 36th Annual International Conference of the IEEE Engineering in Medicine and Biology Society (EMBC), pp. 1977–1980. doi:10.1109/EMBC.2014.6944001

Code of Federal Regulations (CFR), n.d. Title 47, Telecommunication, Part 95.663(d) Emission Bandwidth.

Collinger, J.L., Wodlinger, B., Downey, J.E., Wang, W., Tyler-Kabara, E.C., Weber, D.J., McMorland, A.J.C., Velliste, M., Boninger, M.L., Schwartz, A.B., 2013. High-performance neuroprosthetic control by an individual with tetraplegia. Lancet 381, 557–564. doi:10.1016/S0140-6736(12)61816-9

Cunningham, J.P., Nuyujukian, P., Gilja, V., Chestek, C.A., Ryu, S.I., Shenoy, K.V., 2011. A closed-loop human simulator for investigating the role of feedback control in brain-machine interfaces. J. Neurophysiol. 105, 1932–1949. doi:10.1152/jn.00503.2010

Dethier, J., Nuyujukian, P., Ryu, S.I., Shenoy, K.V., Boahen, K., 2013. Design and validation of a real-time spiking-neural-network decoder for brain–machine interfaces. J. Neural Eng. 10, 036008. doi:10.1088/1741-2560/10/3/036008

Dhillon, G.S., Horch, K.W., 2005. Direct neural sensory feedback and control of a prosthetic arm. IEEE Trans. Neural Syst. Rehabil. Eng. 13, 468–472. doi:10.1109/TNSRE.2005.856072

Dhillon, G.S., Lawrence, S.M., Hutchinson, D.T., Horch, K.W., 2004. Residual function in peripheral nerve stumps of amputees: implications for neural control of artificial limbs1. J. Hand Surg. 29, 605–615. doi:10.1016/j.jhsa.2004.02.006

Dorman, M.G., Prisbe, M.., Meindl, J.D., 1985. A monolithic signal processor for a neurophysiological telemetry system. IEEE J. Solid-State Circuits 20, 1185–1193. doi:10.1109/JSSC.1985.1052457

Dumanian, G.A., Ko, J.H., O'Shaughnessy, K.D., Kim, P.S., Wilson, C.J., Kuiken, T.A., 2009. Targeted Reinnervation for Transhumeral Amputees: Current Surgical Technique and Update on Results: Plast. Reconstr. Surg. 124, 863–869. doi:10.1097/PRS.0b013e3181b038c9

Egan, J., Baker, J., House, P.A., Greger, B., 2012. Decoding Dexterous Finger Movements in a Neural Prosthesis Model Approaching Real-World Conditions. IEEE Trans. Neural Syst. Rehabil. Eng. 20, 836–844. doi:10.1109/TNSRE.2012.2210910

Engdahl, S.M., Christie, B.P., Kelly, B., Davis, A., Chestek, C.A., Gates, D.H., 2015. Surveying the interest of individuals with upper limb loss in novel prosthetic control techniques. J. NeuroEngineering Rehabil. 12, 53. doi:10.1186/s12984-015-0044-2

Ethier, C., Oby, E.R., Bauman, M.J., Miller, L.E., 2012. Restoration of grasp following paralysis through brain-controlled stimulation of muscles. Nature 485, 368–371. doi:10.1038/nature10987

Evarts, E.V., 1968. Relation of pyramidal tract activity to force exerted during voluntary movement. J Neurophysiol 31, 14–27.

Fan, J.M., Nuyujukian, P., Kao, J.C., Chestek, C.A., Ryu, S.I., Shenoy, K.V., 2014. Intention estimation in brain–machine interfaces. J. Neural Eng. 11, 016004. doi:10.1088/1741-2560/11/1/016004

Farina, D., Jiang, N., Rehbaum, H., Holobar, A., Graimann, B., Dietl, H., Aszmann, O.C., 2014. The Extraction of Neural Information from the Surface EMG for the Control of Upper-Limb Prostheses: Emerging Avenues and Challenges. IEEE Trans. Neural Syst. Rehabil. Eng. 22, 797–809. doi:10.1109/TNSRE.2014.2305111

Farina, D., Merletti, R., Enoka, R.M., 2004. The extraction of neural strategies from the surface EMG. J. Appl. Physiol. 96, 1486–1495. doi:10.1152/japplphysiol.01070.2003

Farnsworth, B.D., Talyor, D.M., Triolo, R.J., Young, D.J., 2009. Wireless in vivo EMG sensor for intelligent prosthetic control, in: Solid-State Sensors, Actuators and Microsystems Conference,

2009. TRANSDUCERS 2009. International. Presented at the Solid-State Sensors, Actuators and Microsystems Conference, 2009. TRANSDUCERS 2009. International, pp. 358–361. doi:10.1109/SENSOR.2009.5285488

Faulkner, J.A., Maxwell, L.C., Mufti, S.A., Carlson, B.M., 1976. Skeletal muscle fiber regeneration following heterotopic autotransplantation in cats. Life Sci. 19, 289–296. doi:10.1016/0024-3205(76)90402-1

Fougner, A., Stavdahl, Ø., Kyberd, P.J., Losier, Y.G., Parker, P.A., 2012. Control of Upper Limb Prostheses: Terminology and Proportional Myoelectric Control - A Review. IEEE Trans. Neural Syst. Rehabil. Eng. 20, 663–677. doi:10.1109/TNSRE.2012.2196711

Ganguly, K., Carmena, J.M., 2009. Emergence of a Stable Cortical Map for Neuroprosthetic Control. PLoS Biol 7, e1000153. doi:10.1371/journal.pbio.1000153

Gao, H., Walker, R.M., Nuyujukian, P., Makinwa, K.A.A., Shenoy, K.V., Murmann, B., Meng, T.H., 2012. HermesE: A 96-Channel Full Data Rate Direct Neural Interface in 0.13 m CMOS. IEEE J. Solid-State Circuits 47, 1043–1055. doi:10.1109/JSSC.2012.2185338

Gasson, M., Hutt, B., Goodhew, I., Kyberd, P., Warwick, K., 2005. Invasive neural prosthesis for neural signal detection and nerve stimulation. Int. J. Adapt. Control Signal Process. 19, 365–375. doi:10.1002/acs.854

Georgopoulos, A.P., Kalaska, J.F., Caminiti, R., Massey, J.T., 1982. On the relations between the direction of two-dimensional arm movements and cell discharge in primate motor cortex. J. Neurosci. 2, 1527–1537.

Georgopoulos, A.P., Schwartz, A.B., Kettner, R.E., 1986. Neuronal Population Coding of Movement Direction. Science 233, 1416–1419. doi:10.2307/1697462

Gilja, V., Nuyujukian, P., Chestek, C.A., Cunningham, J.P., Yu, B.M., Fan, J.M., Churchland, M.M., Kaufman, M.T., Kao, J.C., Ryu, S.I., Shenoy, K.V., 2012. A high-performance neural prosthesis enabled by control algorithm design. Nat. Neurosci. 15, 1752–1757. doi:10.1038/nn.3265

Gilja, V., Pandarinath, C., Blabe, C.H., Nuyujukian, P., Simeral, J.D., Sarma, A.A., Sorice, B.L., Perge, J.A., Jarosiewicz, B., Hochberg, L.R., Shenoy, K.V., Henderson, J.M., 2015. Clinical translation of a high-performance neural prosthesis. Nat. Med. 21, 1142–1145. doi:10.1038/nm.3953

Gosselin, B., Ayoub, A., Roy, J.-F., Sawan, M., Lepore, F., Chaudhuri, A., Guitton, D., 2009. A Mixed-Signal Multichip Neural Recording Interface With Bandwidth Reduction. IEEE Trans. Biomed. Circuits Syst. 3, 129–141. doi:10.1109/TBCAS.2009.2013718

Hahne, J.M., Biebmann, F., Jiang, N., Rehbaum, H., Farina, D., Meinecke, F.C., Muller, K.R., Parra, L.C., 2014. Linear and Nonlinear Regression Techniques for Simultaneous and Proportional

Myoelectric Control. IEEE Trans. Neural Syst. Rehabil. Eng. 22, 269–279. doi:10.1109/TNSRE.2014.2305520

Hamed, S.B., Schieber, M.H., Pouget, A., 2007. Decoding M1 Neurons During Multiple Finger Movements. J. Neurophysiol. 98, 327–333. doi:10.1152/jn.00760.2006

Harrison, R.R., Kier, R.J., Chestek, C.A., Gilja, V., Nuyujukian, P., Ryu, S., Greger, B., Solzbacher, F., Shenoy, K.V., 2009. Wireless neural recording with single low-power integrated circuit. IEEE Trans. Neural Syst. Rehabil. Eng. Publ. IEEE Eng. Med. Biol. Soc. 17, 322–329. doi:10.1109/TNSRE.2009.2023298

Hart, R.L., Bhadra, N., Montague, F.W., Kilgore, K.L., Peckham, P.H., 2011. Design and Testing of an Advanced Implantable Neuroprosthesis With Myoelectric Control. IEEE Trans. Neural Syst. Rehabil. Eng. 19, 45–53. doi:10.1109/TNSRE.2010.2079952

Hobby, J., Taylor, P.N., Esnouf, J., 2001. Restoration of Tetraplegic Hand Function by Use of the Neurocontrol Freehand System. J. Hand Surg. Br. Eur. Vol. 26, 459–464. doi:10.1054/jhsb.2001.0587

Hochberg, L.R., Bacher, D., Jarosiewicz, B., Masse, N.Y., Simeral, J.D., Vogel, J., Haddadin, S., Liu, J., Cash, S.S., van der Smagt, P., Donoghue, J.P., 2012. Reach and grasp by people with tetraplegia using a neurally controlled robotic arm. Nature 485, 372–375. doi:10.1038/nature11076

Hochberg, L.R., Serruya, M.D., Friehs, G.M., Mukand, J.A., Saleh, M., Caplan, A.H., Branner, A., Chen, D., Penn, R.D., Donoghue, J.P., 2006. Neuronal ensemble control of prosthetic devices by a human with tetraplegia. Nature 442, 164–171. doi:10.1038/nature04970

Horch, K., Meek, S., Taylor, T.G., Hutchinson, D.T., 2011. Object Discrimination With an Artificial Hand Using Electrical Stimulation of Peripheral Tactile and Proprioceptive Pathways With Intrafascicular Electrodes. IEEE Trans. Neural Syst. Rehabil. Eng. 19, 483–489. doi:10.1109/TNSRE.2011.2162635

Hotson, G., McMullen, D.P., Fifer, M.S., Johannes, M.S., Katyal, K.D., Para, M.P., Robert Armiger, Anderson, W.S., Thakor, N.V., Wester, B.A., Crone, N.E., 2016. Individual finger control of a modular prosthetic limb using high-density electrocorticography in a human subject. J. Neural Eng. 13, 026017. doi:10.1088/1741-2560/13/2/026017

Hudgins, B., Parker, P., Scott, R.N., 1993. A new strategy for multifunction myoelectric control. IEEE Trans. Biomed. Eng. 40, 82–94. doi:10.1109/10.204774

Irwin, Z., Thompson, D., Schroeder, K., Tat, D., Hassani, A., Bullard, A., Woo, S., Urbanchek, M., Sachs, A., Cederna, P., Stacey, W., Patil, P., Chestek, C., 2015. Enabling Low-power, Multi-modal Neural Interfaces through a Common, Low-bandwidth Feature Space. IEEE Trans. Neural Syst. Rehabil. Eng. PP, 1–1. doi:10.1109/TNSRE.2015.2501752

Jarosiewicz, B., Sarma, A.A., Bacher, D., Masse, N.Y., Simeral, J.D., Sorice, B., Oakley, E.M., Blabe, C., Pandarinath, C., Gilja, V., Cash, S.S., Eskandar, E.N., Friehs, G., Henderson, J.M., Shenoy, K.V., Donoghue, J.P., Hochberg, L.R., 2015. Virtual typing by people with tetraplegia using a self-calibrating intracortical brain-computer interface. Sci. Transl. Med. 7, 313ra179–313ra179. doi:10.1126/scitranslmed.aac7328

Jia, X., Koenig, M.A., Zhang, X., Zhang, J., Chen, T., Chen, Z., 2007. Residual Motor Signal in Long-Term Human Severed Peripheral Nerves and Feasibility of Neural Signal-Controlled Artificial Limb. J. Hand Surg. 32, 657–666. doi:10.1016/j.jhsa.2007.02.021

Kao, J.C., Nuyujukian, P., Ryu, S.I., Churchland, M.M., Cunningham, J.P., Shenoy, K.V., 2015. Single-trial dynamics of motor cortex and their applications to brain-machine interfaces. Nat. Commun. 6, 7759. doi:10.1038/ncomms8759

Kennedy, P.R., Bakay, R.A.E., Moore, M.M., Adams, K., Goldwaithe, J., 2000. Direct control of a computer from the human central nervous system. IEEE Trans. Rehabil. Eng. 8, 198–202. doi:10.1109/86.847815

Kilgore, K.L., Hoyen, H.A., Bryden, A.M., Hart, R.L., Keith, M.W., Peckham, P.H., 2008. An Implanted Upper-Extremity Neuroprosthesis Using Myoelectric Control. J. Hand Surg. 33, 539–550. doi:10.1016/j.jhsa.2008.01.007

Kim, H.K., Carmena, J.M., Biggs, S.J., Hanson, T.L., Nicolelis, M.A.L., Srinivasan, M.A., 2007. The Muscle Activation Method: An Approach to Impedance Control of Brain-Machine Interfaces Through a Musculoskeletal Model of the Arm. IEEE Trans. Biomed. Eng. 54, 1520–1529. doi:10.1109/TBME.2007.900818

Kim, S.-P., Simeral, J.D., Hochberg, L.R., Donoghue, J.P., Black, M.J., 2008. Neural control of computer cursor velocity by decoding motor cortical spiking activity in humans with tetraplegia. J. Neural Eng. 5, 455–476. doi:10.1088/1741-2560/5/4/010

Klaes, C., Kellis, S., Aflalo, T., Lee, B., Pejsa, K., Shanfield, K., Hayes-Jackson, S., Aisen, M., Heck, C., Liu, C., Andersen, R.A., 2015. Hand Shape Representations in the Human Posterior Parietal Cortex. J. Neurosci. 35, 15466–15476. doi:10.1523/JNEUROSCI.2747-15.2015

Krusienski, D.J., Sellers, E.W., Cabestaing, F., Bayoudh, S., McFarland, D.J., Vaughan, T.M., Wolpaw, J.R., 2006. A comparison of classification techniques for the P300 Speller. J. Neural Eng. 3, 299. doi:10.1088/1741-2560/3/4/007

Kuiken, T.A., Dumanian, G.A., Lipschutz, R.D., Miller, L.A., Stubblefield, K.A., 2004. The use of targeted muscle reinnervation for improved myoelectric prosthesis control in a bilateral shoulder disarticulation amputee. Prosthet. Orthot. Int. 28, 245–253. doi:10.3109/03093640409167756

Kuiken, T.A., Li, G., Lock, B.A., Lipschutz, R.D., Miller, L.A., Stubblefield, K.A., Englehart, K., 2009. Targeted Muscle Reinnervation for Real-Time Myoelectric Control of Multifunction Artificial Arms. JAMA J. Am. Med. Assoc. 301, 619–628. doi:10.1001/jama.2009.116

Kung, T.A., Langhals, N.B., Martin, D.C., Johnson, P.J., Cederna, P.S., Urbanchek, M.G., 2014. Regenerative Peripheral Nerve Interface Viability and Signal Transduction with an Implanted Electrode: Plast. Reconstr. Surg. 133, 1380–1394. doi:10.1097/PRS.0000000000000168

Lang, C.E., Schieber, M.H., 2004. Human Finger Independence: Limitations due to Passive Mechanical Coupling Versus Active Neuromuscular Control. J. Neurophysiol. 92, 2802–2810. doi:10.1152/jn.00480.2004

Lawrence, S.M., Dhillon, G.S., Jensen, W., Yoshida, K., Horch, K.W., 2004. Acute peripheral nerve recording Characteristics of polymer-based longitudinal intrafascicular electrodes. IEEE Trans. Neural Syst. Rehabil. Eng. 12, 345–348. doi:10.1109/TNSRE.2004.831491

Li, Z., O'Doherty, J.E., Hanson, T.L., Lebedev, M.A., Henriquez, C.S., Nicolelis, M.A.L., 2009. Unscented Kalman Filter for Brain-Machine Interfaces. PLOS ONE 4, e6243. doi:10.1371/journal.pone.0006243

Lovely, D.F., 2004. Signals and Signal Processing for Myoelectric Control, in: LM, A.M.M., BS, FRCPC, FACP, AFCASI, DAAPM (Ed.), Powered Upper Limb Prostheses. Springer Berlin Heidelberg, pp. 35–54.

Ludwig, K.A., Miriani, R.M., Langhals, N.B., Joseph, M.D., Anderson, D.J., Kipke, D.R., 2009. Using a Common Average Reference to Improve Cortical Neuron Recordings From Microelectrode Arrays. J. Neurophysiol. 101, 1679–1689. doi:10.1152/jn.90989.2008

Malik, W.Q., Truccolo, W., Brown, E.N., Hochberg, L.R., 2011. Efficient Decoding With Steady-State Kalman Filter in Neural Interface Systems. IEEE Trans. Neural Syst. Rehabil. Eng. 19, 25–34. doi:10.1109/TNSRE.2010.2092443

Mallela, V.S., Ilankumaran, V., Rao, N.S., 2004. Trends in Cardiac Pacemaker Batteries. Indian Pacing Electrophysiol. J. 4, 201–212.

McFarland, L.V., Winkler, S.L.H., Heinemann, A.W., Jones, M., Esquenazi, A., 2010. Unilateral upper-limb loss: Satisfaction and prosthetic-device use in veterans and servicemembers from Vietnam and OIF/OEF conflicts. J. Rehabil. Res. Dev. 47, 299. doi:10.1682/JRRD.2009.03.0027

Memberg, W.D., Stage, T.G., Kirsch, R.F., 2014. A Fully Implanted Intramuscular Bipolar Myoelectric Signal Recording Electrode. Neuromodulation Technol. Neural Interface 17, 794–799. doi:10.1111/ner.12165

Menz, V., Schaffelhofer, S., Scherberger, H., 2015. Representation of continuous hand and arm movements in macaque areas M1, F5, and AIP: a comparative decoding study. J. Neural Eng. 12. doi:10.1088/1741-2560/12/5/056016

Micera, S., Rossini, P.M., Rigosa, J., Citi, L., Carpaneto, J., Raspopovic, S., Tombini, M., Cipriani, C., Assenza, G., Carrozza, M.C., Hoffmann, K.-P., Yoshida, K., Navarro, X., Dario, P., 2011. Decoding of grasping information from neural signals recorded using peripheral intrafascicular interfaces. J. NeuroEngineering Rehabil. 8, 53. doi:10.1186/1743-0003-8-53

Miller, L.A., Stubblefield, K.A., Lipschutz, R.D., Lock, B.A., Kuiken, T.A., 2008. Improved Myoelectric Prosthesis Control Using Targeted Reinnervation Surgery: A Case Series. IEEE Trans. Neural Syst. Rehabil. Eng. 16, 46–50. doi:10.1109/TNSRE.2007.911817

Miller, L.A., Stubblefield, K.A., Lipschutz, R.D., Lock, B.A., Souza, J.M., Dumanian, G.A., Kuiken, T.A., 2013. Surgical and functional outcomes of targeted muscle reinnervation, in: Targeted Muscle Reinnervation: A Neural Interface for Artificial Limb. pp. 149–163.

Miranda, H., Gilja, V., Chestek, C.A., Shenoy, K.V., Meng, T.H., 2010. HermesD: A High-Rate Long-Range Wireless Transmission System for Simultaneous Multichannel Neural Recording Applications. IEEE Trans. Biomed. Circuits Syst. 4, 181–191. doi:10.1109/TBCAS.2010.2044573

Morel, P., Ferrea, E., Taghizadeh-Sarshouri, B., Audí, J.M.C., Roman Ruff, Hoffmann, K.-P., Lewis, S., Russold, M., Dietl, H., Abu-Saleh, L., Dietmar Schroeder, Krautschneider, W., Meiners, T., Gail, A., 2016. Long-term decoding of movement force and direction with a wireless myoelectric implant. J. Neural Eng. 13, 016002. doi:10.1088/1741-2560/13/1/016002

Moritz, C.T., Perlmutter, S.I., Fetz, E.E., 2008. Direct control of paralysed muscles by cortical neurons. Nature 456, 639–642. doi:10.1038/nature07418

Morrow, M.M., Jordan, L.R., Miller, L.E., 2007. Direct Comparison of the Task-Dependent Discharge of M1 in Hand Space and Muscle Space. J. Neurophysiol. 97, 1786–1798. doi:10.1152/jn.00150.2006

Morrow, M.M., Miller, L.E., 2003. Prediction of Muscle Activity by Populations of Sequentially Recorded Primary Motor Cortex Neurons. J. Neurophysiol. 89, 2279–2288. doi:10.1152/jn.00632.2002

Najafi, K., Wise, K.D., 1986. An implantable multielectrode array with on-chip signal processing. IEEE J. Solid-State Circuits 21, 1035–1044. doi:10.1109/JSSC.1986.1052646

Naples, G.G., Mortimer, J.T., Scheiner, A., Sweeney, J.D., 1988. A spiral nerve cuff electrode for peripheral nerve stimulation. IEEE Trans. Biomed. Eng. 35, 905–916. doi:10.1109/10.8670

National Spinal Cord Injury Statistical Center, 2012. Annual Statistical Report for the Spinal Cord Injury Model Systems - Complete Public Version. University of Alabama at Birmingham, Birmingham, AL.

Navarro, X., Krueger, T.B., Lago, N., Micera, S., Stieglitz, T., Dario, P., 2005. A critical review of interfaces with the peripheral nervous system for the control of neuroprostheses and hybrid bionic systems. J. Peripher. Nerv. Syst. 10, 229–258. doi:10.1111/j.1085-9489.2005.10303.x

Nordhausen, C.T., Rousche, P.J., Normann, R.A., 1994. Optimizing recording capabilities of the Utah Intracortical Electrode Array. Brain Res. 637, 27–36. doi:10.1016/0006-8993(94)91213-0

Oby, E.R., Ethier, C., Miller, L.E., 2013. Movement representation in the primary motor cortex and its contribution to generalizable EMG predictions. J. Neurophysiol. 109, 666–678. doi:10.1152/jn.00331.2012

Olsson, R.H., Wise, K.D., 2005. A three-dimensional neural recording microsystem with implantable data compression circuitry. IEEE J. Solid-State Circuits 40, 2796–2804. doi:10.1109/JSSC.2005.858479

O'Shaughnessy, K.D., Dumanian, G.A., Lipschutz, R.D., Miller, L.A., Stubblefield, K., Kuiken, T.A., 2008. Targeted Reinnervation to Improve Prosthesis Control in Transhumeral Amputees. J Bone Jt. Surg Am 90, 393–400. doi:10.2106/JBJS.G.00268

Park, H., Durand, D.M., 2008. Motion control of musculoskeletal systems with redundancy. Biol. Cybern. 99, 503–516. doi:10.1007/s00422-008-0258-5

Pasquina, P.F., Evangelista, M., Carvalho, A.J., Lockhart, J., Griffin, S., Nanos, G., McKay, P., Hansen, M., Ipsen, D., Vandersea, J., Butkus, J., Miller, M., Murphy, I., Hankin, D., 2015. First-in-man demonstration of a fully implanted myoelectric sensors system to control an advanced electromechanical prosthetic hand. J. Neurosci. Methods, Brain Computer Interfaces; Tribute to Greg A. Gerhardt 244, 85–93. doi:10.1016/j.jneumeth.2014.07.016

Patel, P.R., Na, K., Zhang, H., Kozai, T.D.Y., Kotov, N.A., Yoon, E., Chestek, C.A., 2015. Insertion of linear 8.4 μ m diameter 16 channel carbon fiber electrode arrays for single unit recordings. J. Neural Eng. 12, 046009. doi:10.1088/1741-2560/12/4/046009

Patterson, W.R., Song, Y.-K., Bull, C.W., Ozden, I., Deangellis, A.P., Lay, C., McKay, J.L., Nurmikko, A.V., Donoghue, J.D., Connors, B.W., 2004. A microelectrode/microelectronic hybrid device for brain implantable neuroprosthesis applications. IEEE Trans. Biomed. Eng. 51, 1845–1853. doi:10.1109/TBME.2004.831521

Peckham, P.H., Keith, M.W., Kilgore, K.L., Grill, J.H., Wuolle, K.S., Thrope, G.B., Gorman, P., Hobby, J., Mulcahey, M.J., Carroll, S., Hentz, V.R., Wiegner, A., 2001. Efficacy of an implanted neuroprosthesis for restoring hand grasp in tetraplegia: A multicenter study. Arch. Phys. Med. Rehabil. 82, 1380–1388. doi:10.1053/apmr.2001.25910

Peckham, P.H., Knutson, J.S., 2005. Functional Electrical Stimulation for Neuromuscular Applications. Annu. Rev. Biomed. Eng. 7, 327–360. doi:10.1146/annurev.bioeng.6.040803.140103

Pistohl, T., Schulze-Bonhage, A., Aertsen, A., Mehring, C., Ball, T., 2012. Decoding natural grasp types from human ECoG. NeuroImage 59, 248–260. doi:10.1016/j.neuroimage.2011.06.084

Pohlmeyer, E.A., Solla, S.A., Perreault, E.J., Miller, L.E., 2007. Prediction of upper limb muscle activity from motor cortical discharge during reaching. J. Neural Eng. 4, 369–379. doi:10.1088/1741-2560/4/4/003

Popovic, D.B., Stein, R.B., Jovanovic, K.L., Dai, R., Kostov, A., Armstrong, W.W., 1993. Sensory nerve recording for closed-loop control to restore motor functions. IEEE Trans. Biomed. Eng. 40, 1024–1031. doi:10.1109/10.247801

Putrino, D., Wong, Y.T., Weiss, A., Pesaran, B., 2015. A training platform for many-dimensional prosthetic devices using a virtual reality environment. J. Neurosci. Methods, Brain Computer Interfaces; Tribute to Greg A. Gerhardt 244, 68–77. doi:10.1016/j.jneumeth.2014.03.010

Raichle, K.A., Hanley, M.A., Molton, I., Kadel, N.J., Campbell, K., Phelps, E., Ehde, D., Smith, D.G., 2008. Prosthesis use in persons with lower- and upper-limb amputation. J. Rehabil. Res. Dev. 45, 961–972.

Rizk, M., Bossetti, C.A., Jochum, T.A., Callender, S.H., Nicolelis, M.A.L., Turner, D.A., Wolf, P.D., 2009. A fully implantable 96-channel neural data acquisition system. J. Neural Eng. 6, 026002. doi:10.1088/1741-2560/6/2/026002

Roche, A.D., Rehbaum, H., Farina, D., Aszmann, O.C., 2014. Prosthetic Myoelectric Control Strategies: A Clinical Perspective. Curr. Surg. Rep. 2, 1–11. doi:10.1007/s40137-013-0044-8

Rossini, P.M., Micera, S., Benvenuto, A., Carpaneto, J., Cavallo, G., Citi, L., Cipriani, C., Denaro, L., Denaro, V., Di Pino, G., Ferreri, F., Guglielmelli, E., Hoffmann, K.-P., Raspopovic, S., Rigosa, J., Rossini, L., Tombini, M., Dario, P., 2010. Double nerve intraneural interface implant on a human amputee for robotic hand control. Clin. Neurophysiol. 121, 777–783. doi:10.1016/j.clinph.2010.01.001

Sahin, M., Durand, D.M., 1998. Improved nerve cuff electrode recordings with subthreshold anodic currents. IEEE Trans. Biomed. Eng. 45, 1044–1050. doi:10.1109/10.704873

Sahin, M., Haxhiu, M.A., Durand, D.M., Dreshaj, I.A., 1997. Spiral nerve cuff electrode for recordings of respiratory output. J. Appl. Physiol. 83, 317–322.

Santhanam, G., Ryu, S.I., Yu, B.M., Afshar, A., Shenoy, K.V., 2006. A high-performance brain-computer interface. Nature 442, 195–198. doi:10.1038/nature04968

Schaffelhofer, S., Sartori, M., Scherberger, H., Farina, D., 2015. Musculoskeletal Representation of a Large Repertoire of Hand Grasping Actions in Primates. IEEE Trans. Neural Syst. Rehabil. Eng. 23, 210–220. doi:10.1109/TNSRE.2014.2364776

Schalk, G., Miller, K.J., Anderson, N.R., Wilson, J.A., Smyth, M.D., Ojemann, J.G., Moran, D.W., Wolpaw, J.R., Leuthardt, E.C., 2008. Two-dimensional movement control using electrocorticographic signals in humans. J. Neural Eng. 5, 75. doi:10.1088/1741-2560/5/1/008

Scheme, E., Lock, B., Hargrove, L., Hill, W., Kuruganti, U., Englehart, K., 2014. Motion Normalized Proportional Control for Improved Pattern Recognition-Based Myoelectric Control. IEEE Trans. Neural Syst. Rehabil. Eng. 22, 149–157. doi:10.1109/TNSRE.2013.2247421

Schieber, M.H., 1991. Individuated finger movements of rhesus monkeys: a means of quantifying the independence of the digits. J. Neurophysiol. 65, 1381–1391.

Schwartz, A.B., Kettner, R.E., Georgopoulos, A.P., 1988. Primate motor cortex and free arm movements to visual targets in three- dimensional space. I. Relations between single cell discharge and direction of movement. J. Neurosci. 8, 2913–2927.

Scott, S.H., Kalaska, J.F., 1995. Changes in motor cortex activity during reaching movements with similar hand paths but different arm postures. J. Neurophysiol. 73, 2563–2567.

Serlin, D.M., Schieber, M.H., 1993. Morphologic Regions of the Multitendoned Extrinsic Finger Muscles in the Monkey Forearm. Cells Tissues Organs 146, 255–266. doi:10.1159/000147465

Serruya, M.D., Hatsopoulos, N.G., Paninski, L., Fellows, M.R., Donoghue, J.P., 2002. Brain-machine interface: Instant neural control of a movement signal. Nature 416, 141–142. doi:10.1038/416141a

Simeral, J.D., Kim, S.-P., Black, M.J., Donoghue, J.P., Hochberg, L.R., 2011. Neural control of cursor trajectory and click by a human with tetraplegia 1000 days after implant of an intracortical microelectrode array. J. Neural Eng. 8, 025027. doi:10.1088/1741-2560/8/2/025027

Smith, L.H., Kuiken, T.A., Hargrove, L.J., 2015. Linear regression using intramuscular EMG for simultaneous myoelectric control of a wrist and hand system, in: 2015 7th International IEEE/EMBS Conference on Neural Engineering (NER). Presented at the 2015 7th International IEEE/EMBS Conference on Neural Engineering (NER), pp. 619–622. doi:10.1109/NER.2015.7146699

Smith, L.H., Kuiken, T.A., Hargrove, L.J., 2014. Real-time simultaneous and proportional myoelectric control using intramuscular EMG. J. Neural Eng. 11, 066013. doi:10.1088/1741-2560/11/6/066013

Snoek, G.J., IJzerman, M.J., Hermens, H.J., Maxwell, D., Biering-Sorensen, F., 2004. Survey of the needs of patients with spinal cord injury: impact and priority for improvement in hand function in tetraplegics. Spinal Cord 42, 526–532. doi:10.1038/sj.sc.3101638

Sodagar, A.M., Wise, K.D., Najafi, K., 2009. A Wireless Implantable Microsystem for Multichannel Neural Recording. IEEE Trans. Microw. Theory Tech. 57, 2565–2573. doi:10.1109/TMTT.2009.2029957

Sodagar, A., Perlin, G.E., Yao, Y., Najafi, K., Wise, K.D., 2009. An Implantable 64-Channel Wireless Microsystem for Single-Unit Neural Recording. IEEE J. Solid-State Circuits 44, 2591–2604. doi:10.1109/JSSC.2009.2023159

Stark, E., Abeles, M., 2007. Predicting Movement from Multiunit Activity. J. Neurosci. 27, 8387–8394. doi:10.1523/JNEUROSCI.1321-07.2007

Stewart, J.D., 2003. Peripheral nerve fascicles: Anatomy and clinical relevance. Muscle Nerve 28, 525–541. doi:10.1002/mus.10454

Stubblefield, K.A., Miller, L.A., Lipschutz, R.D., Kuiken, T.A., 2009. Occupational therapy protocol for amputees with targeted muscle reinnervation. J. Rehabil. Res. Dev. 46, 481–488.

Suminski, A.J., Tkach, D.C., Fagg, A.H., Hatsopoulos, N.G., 2010. Incorporating Feedback from Multiple Sensory Modalities Enhances Brain–Machine Interface Control. J. Neurosci. 30, 16777–16787. doi:10.1523/JNEUROSCI.3967-10.2010

Sussillo, D., Nuyujukian, P., Fan, J.M., Kao, J.C., Stavisky, S.D., Ryu, S., Shenoy, K., 2012. A recurrent neural network for closed-loop intracortical brain–machine interface decoders. J. Neural Eng. 9, 026027. doi:10.1088/1741-2560/9/2/026027

Szuts, T.A., Fadeyev, V., Kachiguine, S., Sher, A., Grivich, M.V., Agrochão, M., Hottowy, P., Dabrowski, W., Lubenov, E.V., Siapas, A.G., Uchida, N., Litke, A.M., Meister, M., 2011. A wireless multi-channel neural amplifier for freely moving animals. Nat. Neurosci. 14, 263–269. doi:10.1038/nn.2730

Taylor, D.M., Tillery, S.I.H., Schwartz, A.B., 2002. Direct Cortical Control of 3D Neuroprosthetic Devices. Science 296, 1829–1832. doi:10.1126/science.1070291

Tenore, F.V.G., Ramos, A., Fahmy, A., Acharya, S., Etienne-Cummings, R., Thakor, N.V., 2009. Decoding of Individuated Finger Movements Using Surface Electromyography. IEEE Trans. Biomed. Eng. 56, 1427–1434. doi:10.1109/TBME.2008.2005485

Thompson, D.E., Quitadamo, L.R., Mainardi, L., Laghari, K. ur R., Gao, S., Pieter-Jan Kindermans, Simeral, J.D., Fazel-Rezai, R., Matteucci, M., Falk, T.H., Bianchi, L., Chestek, C.A., Huggins, J.E., 2014. Performance measurement for brain–computer or brain–machine interfaces: a tutorial. J. Neural Eng. 11, 035001. doi:10.1088/1741-2560/11/3/035001

Ursu, D.C., Urbanchek, M.G., Nedic, A., Cederna, P.S., Gillespie, R.B., 2016. In vivo characterization of regenerative peripheral nerve interface function. J. Neural Eng. 13, 026012. doi:10.1088/1741-2560/13/2/026012

Vargas-Irwin, C.E., Shakhnarovich, G., Yadollahpour, P., Mislow, J.M.K., Black, M.J., Donoghue, J.P., 2010. Decoding Complete Reach and Grasp Actions from Local Primary Motor Cortex Populations. J. Neurosci. 30, 9659–9669. doi:10.1523/JNEUROSCI.5443-09.2010

Velliste, M., Perel, S., Spalding, M.C., Whitford, A.S., Schwartz, A.B., 2008. Cortical control of a prosthetic arm for self-feeding. Nature 453, 1098–1101. doi:10.1038/nature06996

Wahnoun, R., He, J., Tillery, S.I.H., 2006. Selection and parameterization of cortical neurons for neuroprosthetic control. J. Neural Eng. 3, 162. doi:10.1088/1741-2560/3/2/010

Warren, D.J., Kellis, S., Nieveen, J.G., Wendelken, S.M., Dantas, H., Davis, T.S., Hutchinson, D.T., Normann, R.A., Clark, G.A., Mathews, V.J., 2016. Recording and Decoding for Neural Prostheses. Proc. IEEE 104, 374–391. doi:10.1109/JPROC.2015.2507180

Warwick, K., Gasson, M., Hutt, B., 2003. THe application of implant technology for cybernetic systems. Arch. Neurol. 60, 1369–1373. doi:10.1001/archneur.60.10.1369

Wattanapanitch, W., Sarpeshkar, R., 2011. A Low-Power 32-Channel Digitally Programmable Neural Recording Integrated Circuit. IEEE Trans. Biomed. Circuits Syst. 5, 592–602. doi:10.1109/TBCAS.2011.2163404

Weir, R.F., Troyk, P.R., DeMichele, G.A., Kerns, D.A., Schorsch, J.F., Maas, H., 2009. Implantable Myoelectric Sensors (IMESs) for Intramuscular Electromyogram Recording. IEEE Trans. Biomed. Eng. 56, 159–171. doi:10.1109/TBME.2008.2005942

Wodlinger, B., Downey, J.E., Tyler-Kabara, E.C., Schwartz, A.B., Boninger, M.L., Collinger, J.L., 2015. Ten-dimensional anthropomorphic arm control in a human brain−machine interface: difficulties, solutions, and limitations. J. Neural Eng. 12, 016011. doi:10.1088/1741-2560/12/1/016011

Wright, T.W., Hagen, A.D., Wood, M.B., 1995. Prosthetic usage in major upper extremity amputations. J. Hand Surg. 20, 619–622. doi:10.1016/S0363-5023(05)80278-3

Wu, W., Gao, Y., Bienenstock, E., Donoghue, J.P., Black, M.J., 2006. Bayesian population decoding of motor cortical activity using a Kalman filter. Neural Comput. 18, 80–118.

Wu, W., Shaikhouni, A., Donoghue, J.R., Black, M.J., 2004. Closed-loop neural control of cursor motion using a Kalman filter, in: Engineering in Medicine and Biology Society, 2004. IEMBS'04. 26th Annual International Conference of the IEEE. pp. 4126–4129.

Yin, M., Li, H., Bull, C., Borton, D.A., Aceros, J., Larson, L., Nurmikko, A.V., 2013. An externally head-mounted wireless neural recording device for laboratory animal research and possible human clinical use, in: 2013 35th Annual International Conference of the IEEE Engineering in Medicine and Biology Society (EMBC). Presented at the 2013 35th Annual International Conference of the IEEE Engineering in Medicine and Biology Society (EMBC), pp. 3109–3114. doi:10.1109/EMBC.2013.6610199

Young, A.J., Smith, L.H., Rouse, E.J., Hargrove, L.J., 2013. Classification of Simultaneous Movements Using Surface EMG Pattern Recognition. IEEE Trans. Biomed. Eng. 60, 1250–1258. doi:10.1109/TBME.2012.2232293

Zhang, F., Mishra, A., Richardson, A., Otis, B., 2011. A Low-Power ECoG/EEG Processing IC With Integrated Multiband Energy Extractor. IEEE Trans. Circuits Syst. Regul. Pap. 58, 2069–2082. doi:10.1109/TCSI.2011.2163972

Zhou, P., Lowery, M.M., Englehart, K.B., Huang, H., Li, G., Hargrove, L., Dewald, J.P.A., Kuiken, T.A., 2007. Decoding a New Neural Machine Interface for Control of Artificial Limbs. J. Neurophysiol. 98, 2974–2982. doi:10.1152/jn.00178.2007

Ziegler-Graham, K., MacKenzie, E.J., Ephraim, P.L., Travison, T.G., Brookmeyer, R., 2008. Estimating the Prevalence of Limb Loss in the United States: 2005 to 2050. Arch. Phys. Med. Rehabil. 89, 422–429. doi:10.1016/j.apmr.2007.11.005

Zou, X., Liu, L., Cheong, J.H., Yao, L., Li, P., Cheng, M.-Y., Goh, W.L., Rajkumar, R., Dawe, G.S., Cheng, K.-W., Je, M., 2013. A 100-Channel 1-mW Implantable Neural Recording IC. IEEE Trans. Circuits Syst. Regul. Pap. 60, 2584–2596. doi:10.1109/TCSI.2013.2249175